Observation and Investigation of the New Proton-Unbound Nuclei ^{30}Ar and ^{29}Cl with In-Flight Decay Spectroscopy

Inaugural-Dissertation zur Erlangung des Doktorgrades der Naturwissenschaftlichen and dem Fachbereich 07 Mathematik und Informatik, Physik, Geographie an der Justus-Liebig-Universität Gießen

vorgelegt von

Xiaodong Xu
geboren in Shaanxi (China)

Gießen 2016

Selbstständigkeitserklärung

Ich erkläre: Ich habe die vorgelegte Dissertation selbständig und ohne unerlaubte fremde Hilfe und nur mit den Hilfen angefertigt, die ich in der Dissertation angegeben habe. Alle Textstellen, die wörtlich oder sinngemäß aus veröffentlichten Schriften entnommen sind, und alle Angaben, die auf mündlichen Auskünften beruhen, sind als solche kenntlich gemacht. Bei den von mir durchgeführten und in der Dissertation erwähnten Untersuchungen habe ich die Grundsätze guter wissenschaftlicher Praxis, wie sie in der „Satzung der Justus-Liebig-Universität Gießen zur Sicherung guter wissenschaftlicher Praxis“ niedergelegt sind, eingehalten.

Datum

Xiaodong Xu

Erstgutachter: Prof. Dr. Christoph Scheidenberger
Zweitgutachter: Prof. Dr. Dr. h.c. Hans Geissel

Tag der mündlichen Prüfung: 30.06.2016

Abstract

Two-proton ($2p$) radioactivity is an exotic nuclear decay mode resulting in the simultaneous emission of two protons. The ground-state $2p$ radioactivity was discovered in the decay of ^{45}Fe in 2002. Later, this novel decay mode was also found in the decays of ^{48}Ni, ^{54}Zn, and ^{19}Mg.

In order to study a promising $2p$ radioactivity candidate ^{30}Ar, an experiment was performed at the Fragment Separator of GSI in Darmstadt (Germany). The in-flight decay technique, which is based on the tracking of the in-flight decay products by using the silicon strip detectors, was employed. Several calibration and alignment procedures were performed to achieve the best-possible accuracy of position and angle measurements. In order to determine the angular and half-life resolutions as well as the detection efficiency, the decays of the previously-known $2p$ emitter ^{19}Mg were remeasured. The $2p$ radioactivity of ^{19}Mg ground state and sequential emission of protons from several known excited states in ^{19}Mg were confirmed. The deduced $2p$ decay energies are consistent with previous data. The evidence on a new excited state in ^{19}Mg at $8.9^{+0.8}_{-0.7}$ MeV above the $2p$ threshold was found. It was tentatively suggested that this new ^{19}Mg state decays by sequential emission of protons via two unknown ^{18}Na resonances at $2.5^{+0.7}_{-0.3}$ MeV and $4.0^{+1.5}_{-0.6}$ MeV above the $1p$ threshold, respectively.

Two previously-unknown proton-unbound nuclei ^{30}Ar and ^{29}Cl were identified by measuring the trajectories of their in-flight decay products $^{28}\mathrm{S}+p+p$ and $^{28}\mathrm{S}+p$, respectively. The analysis of ^{28}S-proton angular correlations provided information on the decay energies and structure of the observed states in ^{30}Ar and ^{29}Cl. The assigned ground state and first excited state of ^{29}Cl were found at $1.8^{+0.1}_{-0.1}$ MeV and $2.3^{+0.1}_{-0.1}$ MeV above the one-proton threshold, respectively. The ground state of ^{30}Ar was found to be $2.45^{+0.05}_{-0.10}$ MeV above the $2p$ emission threshold. Due to a strong Thomas-Ehrman shift, the lowest states in ^{30}Ar and ^{29}Cl point to a violation of isobaric mirror symmetry in the structure of these unbound nuclei. Detailed theoretical calculations of the correlations between $2p$ decay products followed by the Monte Carlo simulations of the detector response to the $2p$ decay were performed in order to investigate the decay mechanism of the ^{30}Ar ground state. Its decay is located in a transition region between simultaneous $2p$ decay and sequential emission of protons. Such an interplay between the true three-body and the sequential two-body decay mechanisms is the first-time observation in a nuclear ground state. The theoretical investigations of the transition dynamics demonstrated a surprisingly strong sensitivity of the decay correlation patterns to the $2p$ decay energy of the ^{30}Ar ground state and the one-proton decay energy as well as the one-proton de-

cay width of the ^{29}Cl ground state. The first hint on so-called fine structure in the decay of ^{30}Ar$^{*}(2^{+})$ was obtained by detecting two decay branches into both ground state and first excited state of ^{28}S. The comparison of the experimental ^{28}S-proton angular correlations with those resulting from the Monte Carlo simulations of the detector response illustrates that other observed ^{30}Ar excited states decay by sequential emission of protons via intermediate resonances in ^{29}Cl. The decay schemes of the observed states in ^{30}Ar and ^{29}Cl were constructed.

Zusammenfassung

Die Zwei-Protonen ($2p$) Radioaktivität ist ein ungewöhnlicher Zerfalls-Modus, bei dem aus einem Atomkern zwei Protonen gleichzeitig emittiert werden. Der $2p$-Zerfall von Atomkernen im Grundzustand wurde experimentell erstmals im Jahr 2002 an ^{45}Fe-Kernen beobachtet. Danach wurde diese neue Zerfallsart auch in anderen Nukliden ^{48}Ni, ^{54}Zn und ^{19}Mg entdeckt. Weltweit gibt es Interesse und theoretische wie experimentelle Untersuchungen dieser besonderen Form der Radioaktivität.

In der vorliegenden Arbeit wurde ein am Fragmentseparator der GSI durchgeführtes Experiment ausgewertet, bei dem ^{30}Ar, welches aufgrund theoretischer Vorhersagen ein weiterer Kandidat ist, der möglicherweise das Phänomen der $2p$-Radioaktivität aufweist, erzeugt und untersucht wurde. Dazu wurde die Methode des "Zerfalls im Flug" angewendet, bei der die Spuren der Zerfallsprodukte (Tochterkern und Protonen) verfolgt und mittels ortsempfindlicher Silizium-Detektoren rekonstruiert werden. Daraus lassen sich Zerfallseigenschaften wie Halbwertszeit und Energietönung sowie über Verzweigungsverhältnisse und angeregte Zustände in den Tochter-Nukliden ableiten. Dabei bewegen sich die Zerfallsprodukte mit nahezu Lichtgeschwindigkeit und um diese Informationen zu gewinnen, müssen die Spuren der Zerfallsprodukte mit geeigneter Präzision bestimmt werden. Dazu wurde ein Verfahren zur software-mäßigen Kalibrierung und Ausrichtung der Detektoren relativ zueinander entwickelt und angewandt um die bestmögliche Genauigkeit bei Positions- und Winkelmessungen zu erzielen; das Ergebnis wurde anhand einer Messung mit dem bereits bekannten $2p$-Emitter ^{19}Mg überprüft. Diese Messung diente gleichzeitig als Referenz zur Überprüfung des gesamten Aufbaus um sicherzustellen, dass aus der Literatur bekannte Ergebnisse zuverlässig reproduziert werden können. In der Tat konnten der $2p$-Zerfall des ^{19}Mg-Grundzustands sowie die sequentielle Emission von zwei Protonen aus mehreren angeregten Zuständen in Übereinstimmung mit den bereits bekannten Daten bestätigt werden. Ferner wurde ein weiterer, bisher nicht bekannter Anregungszustand des ^{19}Mg bei $8.9^{+0.8}_{-0.7}$ MeV oberhalb der $2p$-Schwelle entdeckt. Die vorliegenden Daten werden so interpretiert, dass dieser Zustand zwei Protonen sequentiell über zwei unbekannte Resonanz-Zustände in ^{18}Na bei $2.5^{+0.7}_{-0.3}$ MeV bzw. $4.0^{+1.5}_{-0.6}$ MeV oberhalb der $1p$-Schwelle emittiert.

Als wichtigstes Ergebnis wurden die beiden neuen, proton-ungebundenen Isotope ^{30}Ar und ^{29}Cl erstmalig nachgewiesen sowie ihre (Zerfalls-)Eigenschaften durch Messung der Zerfallsprodukte $^{28}\mathrm{S} + p + p$ bzw. $^{28}\mathrm{S} + p$ untersucht. Die Analyse der Winkel-Korrelation von ^{28}S und Proton(en) beim Zerfall im Flug liefert Informationen zu Zerfallsenergien, angeregten Zuständen und Struktur der Nuklide ^{30}Ar und ^{29}Cl. Der Grund-

sowie der erste angeregte Zustand in ^{29}Cl wurden bei $1.8^{+0.1}_{-0.1}$ MeV und $2.3^{+0.1}_{-0.1}$ MeV oberhalb der Proton-Schwelle gefunden. Der Grundzustand in ^{30}Ar liegt $2.45^{+0.05}_{-0.10}$ MeV oberhalb der 2*p*-Schwelle. Aufgrund einer signifikanten Thomas-Ehrman Verschiebung deutet die Lage dieser Niveaus auf eine Verletzung der isobaren Spiegelsymmetrie in diesen Kernen hin.

Um die experimentellen Daten zu interpretieren, um die Korrelationen der 2*p*-Zerfälle zu analysieren und um den Zerfallsmechanismus von ^{30}Ar im Detail zu verstehen wurden umfangreiche theoretische Untersuchungen und Simulationsrechnungen durchgeführt. Dabei stellte sich heraus, dass der 2*p*-Zerfall von ^{30}Ar in einem interessanten Übergangsbereich von gleichzeitiger zu sequentieller Emission der beiden Protonen liegt. Das wechselweise Zusammenspiel von Drei-Körper-Zerfall und zwei aufeinanderfolgenden Zwei-Körper-Zerfällen, welches hier erstmalig beobachtet wird, ergibt sich aus der geringen Bindungsenergie und der energetischen Lage der beteiligten Zustände in der Umgebung der Protonen-Abbruchkante: die theoretische Untersuchung der Zerfallsdynamik ergibt eine überraschende und starke Abhängigkeit der beobachteten Korrelationen im 2*p*-Zerfalls des ^{30}Ar von der Lage des Grundzustands, des Q-Wertes für 1*p*-Zerfall und der Breite des 1*p*-Zerfalls des ^{29}Cl-Grundzustands. Die experimentelle Beobachtung von zwei Zerfallszweigen des ersten angeregten ^{30}Ar$^{*}(2^{+})$-Zustands in den ersten angeregten bzw. den Grundzustand von ^{28}S wird als "Feinstruktur" des 2*p*-Zerfalls interpretiert. Der Vergleich der gemessenen ^{28}S-Proton-Winkelverteilungen mit den Ergebnissen von Monte-Carlo Rechnungen ergibt, dass die anderen angeregten Zustände des ^{30}Ar durch sequentielle Emission der Protonen via eines resonanten Zwischenzustands in ^{29}Cl zerfallen. Unter Einbeziehung aller vorliegenden Informationen wurden tentative Zerfalls- und Niveau-Schemata von ^{30}Ar und ^{29}Cl konstruiert.

Contents

List of Figures

List of Tables

1 Introduction

1.1 Nuclear Decay Modes

Exotic nuclei have a large excess of protons (or neutrons) in comparison with the stable isotopes [1], hence they are unstable and always transform to their stable daughter nuclei via one (or several) radioactive decay mode(s). So far, the discovered decay modes include α decay, β^- decay, β^+ decay or electron capture (EC), γ radiation, fission, β-delayed particle emission, one-proton radioactivity, two-proton radioactivity, and exotic-cluster emission [1]. Several of the above-mentioned decay modes are schematically illustrated in Figure 1.1.

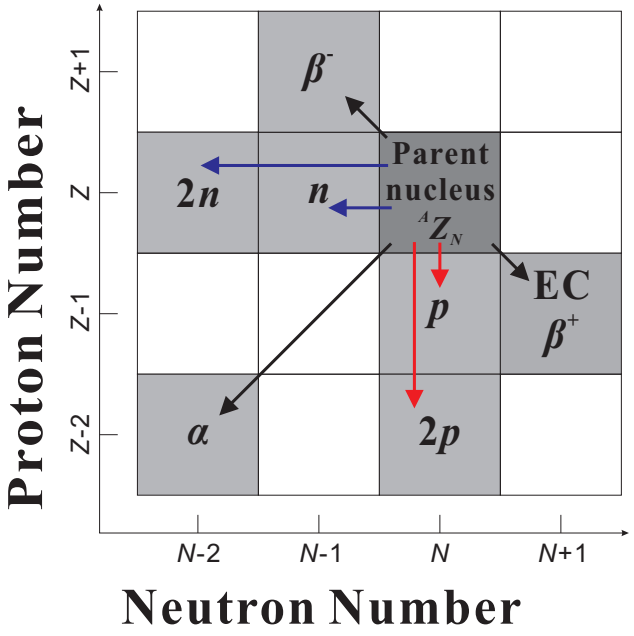

Figure 1.1: Schematic illustration of various decay modes. $^{A}Z_{N}$ represents a parent nucleus with proton number Z and neutron number N as well as the mass number A. α decay, β^- decay, β^+ decay, and electron capture are well-known decay modes which are shown by black arrows. One-proton radioactivity and two-proton radioactivity are shown by the red arrows. They were observed in the 1982 [2, 3] and in 2002 [4, 5], respectively. The blue arrows indicate the one- and two-neutron radioactivity, which have been predicted for a long time in analogy to proton radioactivity [6]. However, they have not been unambiguously observed.

[1] Some nuclei emit fragments heavier than α particle, e.g., C, O.

Figure 1.1 schematically illustrates several nuclear decay modes. Among them, α decay, β^- decay, β^+ decay, electron capture, together with γ radiation are well-known decay modes. Nuclear fission is a process which mother nucleus decays by splitting up into two similar pieces. All these decay modes were discovered in the early period of the last century. They are important phenomena in nuclear physics. They have provided rich information on the structure of atomic nucleus and found many applications in several branches of physics where nuclear properties are relevant, e.g., nuclear astrophysics.

During the last half-century, owing to the tremendous development of experimental techniques and the application of powerful experimental facilities, especially secondary beam facilities, more and more exotic nuclei both in proton-rich side and neutron-rich side became accessible. Several exotic decay modes such as β-delayed particle emission, one-proton radioactivity and two-proton radioactivity were successively discovered. Recently, an experiment studied two-neutron radioactivity of the neutron-rich nucleus ^{26}O [7, 8]. This achievement possibly opened the door for observation of a new decay mode. However, further experimental observations and theoretical investigations are required for the verification. A state-of-art review of current knowledge on the exotic nuclear decay modes can be found in [9].

1.2 Two-Proton Radioactivity

Among the observed decay modes, two-proton radioactivity was proposed for the first time by Goldansky in the early 1960s [6]. In his pioneer work, simultaneous two-proton emission was predicted to appear in the even Z isotopes beyond the proton drip-line, in which one-proton emission is energetically prohibited but the ejection of two protons is allowed due to the pairing interaction. Concerning the general condition for two-proton radioactivity, Goldansky proposed that the positive binding energy of the first proton must be larger than the half width of emitting the second one [6].

In principle, the emission of two protons from a nuclear state can be in various ways [6, 9] which are shown in Figure 1.2. In case (a), because the decay energy Q for one-proton emission ($Q_p = -S_p$) and for two-proton emission ($Q_{2p} = -S_{2p}$) are positive, both decay channels are possible. However, sequential 2*p* emission is energetically forbidden. In contrast to case (a), the sequential 2*p* decay via a narrow intermediate state of nucleus $[A-1]$ becomes possible in case (b). Panel (c) displays the so called true two-proton decay, in which one-proton emission is energetically prohibited and two-protons are emitted simultaneously. True 2*p* decay is a genuine three-body decay process which in general cannot be reduced to a sequence of two-body decays, e.g., successive one-proton emission. In this decay mode, correlations between the three decay products are important. In panel (d) and panel (e), besides the two-proton decay, the sequential emis-

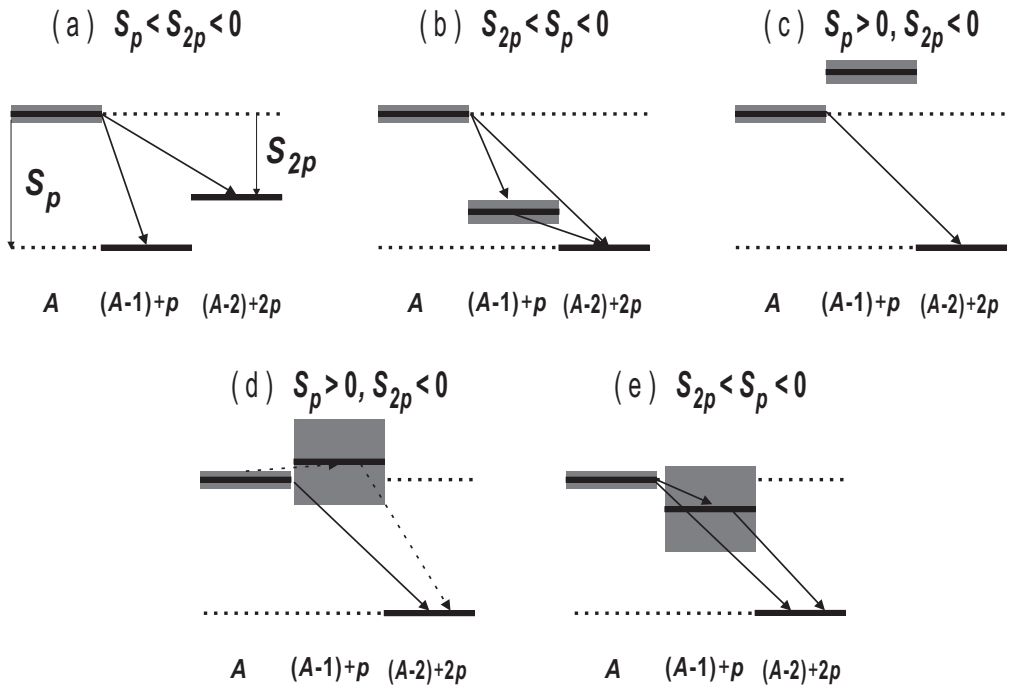

Figure 1.2: Energy conditions for different types of two-proton emission from a nuclear state. The state of the parent nucleus with mass number A decays either by direct $2p$ emission into the state of the daughter nucleus with mass number $A-2$ or by sequential emission of protons via the intermediate state of nucleus with mass number $A-1$. $S_p(Z,A) = B(Z,A) - B(Z-1,A-1)$ and $S_{2p}(Z,A) = B(Z,A) - B(Z-2,A-2)$ are one- and two-proton separation energies, respectively. The B(Z, A) is the binding energy of a nuclide with proton number Z and mass number A. (a) Both $1p$ emission and $2p$ emission are possible. (b) Sequential decay via a narrow intermediate state becomes possible. (c) True $2p$ decay. (d) and (e) Sequential decay may proceed due to a broad intermediate state. See text for details. The figure is based on the Figure 25 of Ref. [9].

sion of protons is energetically allowed due to a broad intermediate state, which the $1p$ decay energy is of the same order as the $1p$ daughter's width. Such scenarios are named as "democratic decays" [10].

1.3 Experimental Results on Two-Proton Decay

Nuclear structure studies have increasingly focused on nuclei far from stability over past years. The two-proton emission, particularly the true two-proton decay, has gained widespread appeal because it provides a novel and powerful tool for the investigation of the structure of nuclei located at and beyond the proton drip-line. After the prediction of $2p$ radioactivity, much experimental work was devoted to study this decay mode.

Although the discovery of ground-state (g.s.) 2*p* radioactivity had to wait for more than 40 years, a lot of experimental knowledge on its related phenomena (e.g., democratic decay and excited-state 2*p* emission) has been accumulated. In this section, the light nuclei which emit two protons via the democratic decay mechanism will be introduced firstly. Then the excited-state 2*p* emission will be described. It is followed by a review of two-proton radioactivity. A comprehensive summary of experimental studies on two-proton decay can be found in [11].

Table 1.1: Ground-state two-proton emitters which have been investigated experimentally. Q_{2p}, Γ, $T^{2p}_{1/2}$, and BR denote the decay energy, partial width, partial half-life, and branching ratio for the 2*p* decay, respectively.

^{A}Z	Q_{2p}/keV	Γ or $T^{2p}_{1/2}$	BR/%	Experiments
^{6}Be	1371(5)	92(6) keV		[12]
^{12}O	1820(120)	400(250) keV		[13]
	1790(40)	580(200) keV		[14]
	1800(400)	600(500) keV		[15]
	1638(24)	<72 keV		[16]
^{16}Ne	1340(80)	200(100) keV		[13]
	1399(24)	110(40) keV		[17]
	1350(80)	<200 keV		[18]
	1388(15)	82(15) keV		[19]
	1466(20)	<80 keV		[20]
^{19}Mg	750(50)	4.0(1.5) ps		[21]
		$1.21^{+0.30}_{-0.29}$ to $4.4^{+1.7}_{-1.9}$ ps		[22]
^{45}Fe	1100(100)	$4.0^{+3.3}_{-1.8}$ ms	≈80	[4]
	1140(50)	$8.5^{+6.4}_{-3.2}$ ms	70-80	[5]
	1154(16)	$2.8^{+1.0}_{-0.7}$ ms	57^{+10}_{-10}	[23]
		$3.7^{+0.4}_{-0.4}$ ms	70^{+4}_{-4}	[24]
^{48}Ni	1350(20)	$8.4^{+12.8}_{-7.0}$ ms	25^{+29}_{-19}	[23]
		$3.0^{+2.2}_{-1.2}$ ms	70^{+20}_{-20}	[25]
^{54}Zn	1480(20)	$3.7^{+2.2}_{-1.0}$ ms	87^{+10}_{-17}	[26]
	1280(210)	$1.7^{+0.7}_{-0.5}$ ms	92^{+6}_{-13}	[27]

1.3.1 Democratic Decay

Table 1.1 lists all the g.s. 2*p* emitters studied experimentally up to now. Among them, the first 2*p* unbound system which was experimentally studied is ^{6}Be [28]. In this work,

an enhancement of low energy α particles compared with a simple phase-space distribution was observed. However, no conclusions concerning the decay mechanism were reached. Later Bochkarev *et al.* performed detailed studies of ^{6}Be decays. Energy and angular distributions of the emitted particles were measured [10, 29]. The interpretation of the correlations has led to the concept of "democratic decay" [10]. In such a decay no strong energy focusing in kinematic space is formed, and the decay mechanism has a three-body feature [9]. In recent studies, Grigorenko *et al.* [30] and Egorova *et al.* [31] experimentally reconstructed the full three-body correlation pictures for 2*p* decay of the ^{6}Be ground state and its first excited state (e.s.), which provided the insight into the mechanism of "democratic decay". The experimental results were found to agree well with the predictions of a theoretical three-body model [32, 33]. Fomichev *et al.* investigated three-body $\alpha + p + p$ continuum of ^{6}Be by performing kinematically complete measurements. Detailed correlation information was obtained for ^{6}Be g.s. and first e.s. The observed negative parity continuum was interpreted as the isovector soft dipole mode associated with ^{6}Be g.s. [34].

^{12}O is another 2*p*-unbound nucleus. An early experimental study by Kekelis *et al.* indicated that ^{12}O has a significant branching ratio for diproton decay [2] [13]. However, in the following study by Kryger *et al.*, the two-proton emission from ^{12}O g.s. was observed, but no evidence for diproton decay was seen [14]. Subsequently, it was found that the ground state of ^{11}N is below that of ^{12}O, which opens the way for sequential decay [35–37]. Combined with these studies, a consistent explanation of the two-proton decay of ^{12}O g.s. in terms of sequential proton emission was established, the decay mechanism belongs to the class shown in Figure 1.2(e) [38].

One of other short-lived two-proton emitters in the light proton-rich nuclear territory is ^{16}Ne. An early study on this nucleus was performed based on the measured mass and penetrability calculation, Kekelis *et al.* suggested that ^{16}Ne has a significant branching ratio for diproton emission [13]. A recent experiment performed by Mukha *et al.* investigated 2*p* decay of ^{16}Ne by measuring the trajectories of in-flight decay products. The reconstructed ^{14}O-*p* and *p*-*p* correlations implied a genuine three-body decay mechanism [18]. Another recent experimental study on the decay of ^{16}Ne states to $^{14}O + p + p$ continuum was performed. The correlations between the momenta of the three decay products were measured and their dependence on the long-range three-body Coulomb interaction was observed [20].

[2] The diproton picture states that two protons can be considered as a single "diproton" (or ^{2}He) particle, which is tunneling through the barrier along the straight classical trajectory.

1.3.2 Two-Proton Emission from Excited States

Besides g.s. 2*p* decay, the 2*p* emission from excited states can be also found in some nuclei. These states were populated either by β decay or by nuclear reactions. The β-delayed 2*p* emission from several nuclei (^{22}Al, ^{23}Si, ^{26}P, ^{27}S, ^{31}Ar, ^{35}Ca, ^{39}Ti, ^{43}Cr, and ^{50}Ni) has been summarized and discussed in Ref. [11], it is found that all these cases belong to the sequential emission mechanism, i.e., the ejection of the two protons can be described as a sequence of two one-proton emissions.

In order to search for *p*-*p* correlations going beyond the sequential decay mechanism, the excited states of a few other 2*p* emitters were fed by nuclear reactions. Mercurio *et al.* studied the decay of excited states in ^{10}C to the 2*p* + 2α exit channel. It was found that e.s. of ^{10}C at 6.57 MeV undergoes two-proton decay to ^{8}Be g.s. [39]. In an experiment performed by Bain *et al.*, the 7.77 MeV e.s. of ^{14}O was populated by a resonance reaction and 2*p* emission from this state was found to be dominated by sequential decay [40]. Concerning the first e.s. of ^{16}Ne at 1.69 MeV, it was populated in neutron knockout reactions and an interplay between sequential and simultaneous 2*p* decay from this state was investigated [41]. The first e.s. (spin parity $J^{\pi} = 3/2^{-}$) and second e.s. ($J^{\pi} = 5/2^{-}$) of ^{17}Ne were populated via Coulomb excitations. No evidence for simultaneous 2*p* emission of the first e.s. of ^{17}Ne was found and sequential 2*p* decay from the second e.s. of ^{17}Ne was observed [42]. The simultaneous 2*p* emission from the 6.15 MeV state ($J^{\pi} = 1^{-}$) in ^{18}Ne was observed with ^{17}F + ^{1}H reaction. However, due to the limited angular coverage, diproton emission and direct three-body decay could not be distinguished by this experiment [43]. In another experiment, the same e.s. of ^{18}Ne was populated by Coulomb excitation. The evidence for diproton emission from this e.s. was reported. The democratic decay mechanism was found to have a lager contribution to the 2*p* emission [44]. Several broad resonances of ^{19}Ne have been observed and two of them were found to decay by sequential 2*p* emission [45]. In an experiment by Lin *et al.*, two-proton emission from excited states of ^{29}S was investigated by detecting the $^{27}\mathrm{Si} + p + p$ coincidence. The two-proton decay from excited states between 9.6 MeV and 10.4 MeV was found to exhibit a diproton emission feature [46].

As an interesting case, the long-lived high-spin 21^{+} isomer in ^{94}Ag decaying by 2*p* emission was reported by Mukha *et al.* [47]. On the basis of the measured *p*-*p* correlations, the evidence for simultaneous 2*p* decay of this isomer was found. Such a two-proton radioactivity behavior was attributed to a very large deformation of this isomer [47]. This discovery and related conclusions have caused several controversies [48–52]. Further experimental investigations are needed to obtain the detail information on the decay mechanism of this isomer.

Furthermore, the decay of isobaric analog state (IAS) of ^{8}B were studied and this IAS

was found to decay by prompt emitting two protons to the IAS of ^{6}Li [53, 54]. The authors claimed that such a 2p decay of IAS extended the definition of direct 2p decay to the third class. Besides the simultaneous 2p emission and democratic decay, the third case corresponds to the situation that 1p decay is energetically allowed, but isospin forbidden. Another experiment confirmed this new decay mechanism by investigating the decay from IAS in ^{12}N. The results show that it decays to the IAS in ^{10}B [16].

1.3.3 Experimental Observation of Ground-State Two-Proton Radioactivity

After its prediction more than 40 years, ground-state two-proton radioactivity was discovered for the first time in 2002 [4,5]. Two different experiments, one performed at the Fragment Separator in GSI [3] and shortly afterwards, the other at the LISE separator in GANIL [4], independently observed that the g.s. of ^{45}Fe decays by simultaneous emission of two protons. Later ^{54}Zn [26], ^{19}Mg [21], and ^{48}Ni [25] were found to be other g.s. 2p radioactive nuclei. The decay properties of all already-discovered g.s. 2p emitters can be found in Table 1.1. The discovery of two-proton radioactivity is one of the most prominent results in the studies of systems beyond the proton drip-line.

The Decay of ^{45}Fe

In both experiments which led to the discovery of the two-proton radioactivity [4, 5], the ^{45}Fe ions were produced by fragmentation reactions and they were implanted into silicon detectors. The decay energy and decay time were measured. Although only a few 2p decay events were observed in both experiments, it was sufficient to claim the discovery of a new decay mode because the experimental data are free of background and only can be explained by 2p decay hypothesis. In a subsequent experiment performed at GANIL, the decay information (e.g., decay energy and half-life) on ^{45}Fe was obtained with larger statistics and improved accuracy [23]. In 2007, Giovinazzo *et al.* reported the first direct observation of the individual protons in the two-proton decay of ^{45}Fe with the Time-Projection Chamber (TPC) [55]. Later, Miernik *et al.* utilized the novel Optical Time Projection Chamber (OTPC) [56], which is based on the optical readout the TPC signals, to image the 2p decay of ^{45}Fe. In this experiment, energy and angular correlations between two protons were determined, indicating a three-body decay character [24].

The Decay of ^{54}Zn

The nucleus ^{54}Zn was observed for the first time in 2004 [26]. In this experiment, ^{54}Zn ions were produced by the quasifragmentation of a ^{58}Ni beam. Eight ^{54}Zn implantation events were observed and seven of them were found to decay by two-proton emission. The decay energy, branching ratio, and partial half-life for 2p decay were deter-

[3] GSI Helmholtzzentrum für Schwerionenforschung GmbH, Darmstadt, Germany.
[4] Grand Accélérateur National d'Ions Lourds, Caen Cedex, France.

mined [26]. In order to identify the emitted two protons separately, a modified Time-Projection Chamber was used in a later experiment [57]. The decay energy and half-life measured by this experiment agreed with the previous experiment. Meanwhile, energy and angular distributions of decay products were also obtained.

The Decay of ^{19}Mg

A technique based on particle tracking of decays in flight (see detail in subsection 1.5.3) was applied by Mukha *et al.* to investigate the 2*p* radioactivity of ^{19}Mg [21]. In this experiment, the trajectories of 2*p* decay products of ^{19}Mg were measured by using tracking silicon strip detectors (SSDs). The 2*p*-decay vertices and fragment correlations were reconstructed. The determined 2*p* decay energy and half-life of ^{19}Mg g.s. can be found in Table 1.1. The data obtained in this experiment also revealed several excited states in ^{19}Mg, and they were found to decay by sequential emission of protons [58]. In a recent work by Voss et al. [22], the half-life of two-proton decay of ^{19}Mg g.s. was measured by utilizing another kind of experimental technique. Researchers employed a thin silicon detector positioned at varying distance downstream of the reaction target to measure the energy loss of ^{19}Mg and its two-proton decay daughter ^{17}Ne. The extracted half-life range of ^{19}Mg is displayed in Table 1.1. One can see the half-life of ^{19}Mg g.s. deduced from two experiments agree with each other.

The Decay of ^{48}Ni

In an experiment, which was performed at GANIL in 2005 [23], the decay of ^{48}Ni was observed for the first time and one decay event was found to be consistent with two-proton radioactivity. In 2011, Pomorski *et al.* studied the decay of ^{48}Ni by recording the tracks of charged particles. The direct evidence for 2*p* decay of this nuclide was obtained [25]. Recently, an experimental investigation of ^{48}Ni observed six decay events by employing the OTPC [59]. Among them, four events are assigned to g.s. 2*p* radioactivity. The decay energy of ^{48}Ni is determined as 1.29(4) MeV.

1.4 Theoretical Description of Two-Proton Emission

Accompanied with the experimental study of 2*p* emission, several theoretical models on 2*p* decay were developed. Historically, Goldansky proposed the first idea of the diproton approximation to describe the 2*p* emission phenomenon [6, 60]. In this quasiclassical approach, the two protons are assumed to form a point-like "diproton" particle (^{2}He). The diproton propagates under the barrier along a classical trajectory. Although possible binding or resonance energies were not taken into account in this model, it was helpful to understand the 2*p* emission in a simple manner. Actually, the diproton model was often used in the early 2*p* decay calculations, e.g., [61–63]. However, recent studies have revealed severe problems concerning this model [9, 64, 65].

In order to include the *p*-*p* correlation which is neglected in the diproton model, a R-matrix model was employed [66,67]. In this model, the two-proton decay is sub-divided into two sequential decays. First, the parent nucleus emits two protons which form a resonance. Second, this resonance disintegrates by ejecting the two protons. Nuclear structure effects are included via spectroscopic factors for the overlap of the wave functions of the parent and the daughter system. However, the emission dynamics is not considered in the R-matrix model.

The first quantum-mechanical model proposed for 2*p* decay is a so-called three-body model developed by Grigorenko *et al.* [32, 33]. Jacobi coordinates are adopted in this model to treat the three-body system consisting of an inert core and two protons. The application of the realistic proton-proton and core-proton interactions allows for a description of the emission dynamics and predictions of the lifetime as well as the fragment correlations. The three-body model has been widely used in recent 2*p* decay studies, e.g., [20, 21, 27, 30, 68]. It is worth mentioning that the three-body model has reasonably explained unexpectedly long half-lives of all measured true 2*p*-emitters, which are regarded as a result of a considerable influence of few-body centrifugal and Coulomb barriers together with nuclear structure effects. Nevertheless, nuclear structure information can be only taken into account at the level of single-particle energies, thus 2*p* precursors with dominating collective configurations (e.g., 21^+ isomer of ^{94}Ag) cannot be addressed in this model.

Another model on 2*p* decay is the shell model embedded in the continuum (SMEC) [69]. Because it can treat the coupling to the continuum, the SMEC was expected to deal with loosely bound or even unbound nucleons well. This model was extended to treat nuclei with two loosely bound nucleons [70]. However, due to the lack of three-body asymptotic channels, the calculation of various correlation functions in the SMEC framework is hindered [11].

Besides the above-mentioned models, some other theoretical approaches were also applied to investigate the two-proton decays and related phenomena. The relativistic mean-field theory was employed to study the light-medium nuclei and several potential candidates were predicted to exhibit two-proton radioactivity [71]. The covariant density functional theory was used to study the nuclei beyond the proton drip-line. The half-lives of some proton emitters were calculated [72, 73]. A time-dependent approach was utilized to calculate the decay width for two-proton emission and to study the effect of the correlation between the two emitted protons. It was found that the paring interaction may significantly enhance the probability for the diproton decay [74]. Recently, Delion *et al.* employed a simple model within the framework of scattering theory to study two-proton emission [75]. A strong dependence of the pairing gap and decay width

on the proton-proton interaction strength was revealed. A series of work by Fortune and coworker employed a weak coupling and simple potential-model to calculate mass, width, and other properties of some 2*p* emitters, e.g. ^{16}Ne [76] and ^{19}Mg [77–79].

1.4.1 Two-Proton Radioactivity Landscape

In the pioneer work of Goldansky, who predicted the existence of 2*p* radioactivity for the first time [6], several candidates were proposed which may exhibit this novel exotic decay mode. Based on the masses of nuclei available at that time, Goldansky proposed some proton-rich nuclei which fulfill an energy criterion as the potential candidates for observing the 2*p* radioactivity. Following a similar manner, Jänecke studied the properties of the 2*p* decay process based on the calculated masses of light nuclei and state widths. Several light nuclei were named as candidates for the 2*p* decay [80]. In the same work, the author also pointed out that the definition of 2*p* radioactivity involves a condition pertaining to energies and a condition related to the lifetimes or the widths of the decaying states. However, the latter condition is difficult to be well-defined. In a later work, Goldansky updated the tabulation of 2*p* radioactivity candidates by considering an explicit energy condition and a approximate lifetime criterion [81]. These studies served as the first guidance for the experimental search of 2*p* radioactivity.

After the discovery of 2*p* radioactivity of ^{45}Fe in 2002, Grigorenko *et al.* used the abovementioned three-body model to systematically study lifetime dependencies on the decay energy and three-body correlations for several nuclei [82]. Dozens of prospective true 2*p* emitters were predicted, and they are shown in the Figure 1.3. Among these candidates, besides ^{45}Fe, ^{19}Mg, ^{48}Ni, and ^{54}Zn have been proven to be true 2*p* emitters.

In a recent study, the global landscape of g.s. 2*p* radioactivity has been quantified by using the nuclear density functional theory [83]. Based on the calculated binding energies and 2*p* decay half-lives, many g.s. 2*p*-decay candidates have been identified by applying the following energy and lifetime conditions:

$$\begin{aligned} S_{2p} < 0,\ S_p > 0, \\ 10^{-7}\mathrm{s} < T_{1/2}^{2p} < 10^{-1}\mathrm{s}. \end{aligned} \tag{1.1}$$

The main conclusion of this work is that 2*p*-decaying isotopes exist in almost every isotopic chain between Ar and Pb, which indicates that g.s. 2*p* radioactivity is a typical feature for the proton-unbound isotopes with even atomic numbers. According to the predictions, the upper end of the 2*p*-decay territory is hindered by α decay, which totally dominates above Pb. The nuclei of the most interest are around ^{103}Te - ^{110}Ba, where the competition between 2*p* emission and α decay is predicted. Since these two decay modes were never observed before to coexist in the same nucleus, such an experi-

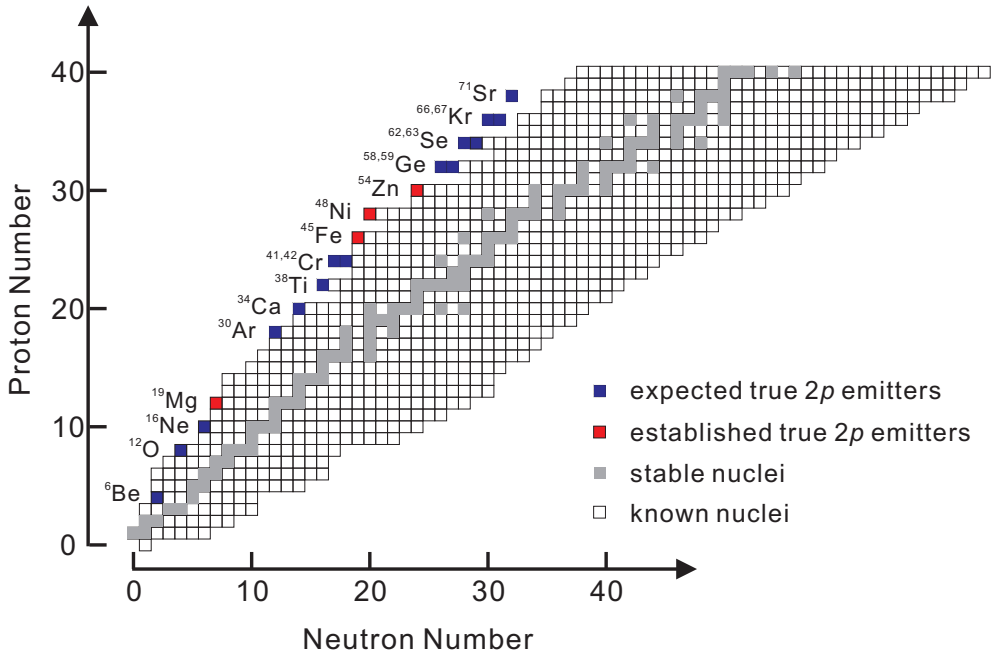

Figure 1.3: The landscape of true 2*p* emitters predicted by the three-body model [82]. The known nuclei are marked by hollow squares, stable nuclei by grey squares. The established g.s. true 2*p* emitters are highlighted by red boxes, while expected true 2*p* decay candidates are shown by blue boxes.

mental observation will provide an excellent test of nuclear structure models and deeper understanding of the dynamics of charged particle emission from nuclei.

1.5 Experimental Techniques Concerning the Two-Proton Decay Studies

As described in the previous section, dozens of nuclei have been predicted as 2*p* radioactivity candidates, and all of them are located at or beyond the proton drip-line of the nuclear landscape. In general, one can choose one of three established experimental methods to study a particular candidate depending on its lifetime. Those three approaches include implantation-decay method, missing (invariant) mass method, and in-flight decay method. In the following, these experimental methods will be introduced.

1.5.1 Implantation Decay Method

In implantation experiments, the nuclei of interest are stopped in a detector (e.g., OTPC). The lifetime and the decay energy can be obtained by registering the decay events. This method is appropriate for studying the nuclei with lifetimes from characteristic time for

β-decay (in the range from millisecond (ms) to s) to time required for fragment separation (about 10^{-8} s). Therefore, the implantation method can be employed for studies of the decays of relatively long-lived 2*p* emitters. The early experimental studies of g.s. 2*p* emitters (e.g., ^{45}Fe [4, 5]) adopted the implantation method. However, due to the use of thick silicon detectors, the observation of individual protons was hindered [57]. In order to observe the protons emitted from the parent nucleus directly, two kinds of implantation detector were developed based on the principle of TPC. Scientists at CEN Bordeaux – Gradignan made a special TPC with electric readout which is based on charge amplification in the gas by using gas electron multipliers (GEMs) [84]. Independently, scientists at the University of Warsaw developed the OTPC by combining the technique of multistep avalanche chamber with optical imaging [56]. By means of these TPC-based detectors, two-proton decay of ^{45}Fe [24, 55], ^{54}Zn [27, 57], and ^{48}Ni [25] were directly observed. Without exception, all these 2*p* precursors have half-lives of the order of milliseconds which are suitable for the implantation method.

1.5.2 Missing Mass Method

In the case of relatively short-lived nuclei (e.g., shorter than hundreds of nanoseconds (ns)), the implantation method is inapplicable since the nuclei decay before they can be implanted. One may choose the missing mass (or invariant mass) method to study these nuclei. This method was applied in the studies of light 2*p* emitters, e.g., ^{6}Be [10] and ^{12}O [14]. The range of widths measurable in the missing mass experiments is tens of keV and more (or lifetimes less than 10^{-19} s). Considering the lifetime range which is suitable for the implantation method, there is a 12 orders of magnitude gap between the lifetime intervals measurable by the implantation and missing (invariant) mass experiments. In order to fill this gap and to search several promising 2*p* radioactivity candidates (e.g., ^{19}Mg) which were predicted to have lifetimes of the order of picoseconds (ps) [82], the in-flight decay technique was proposed in the early 2000s [85]. This novel experimental method is described below.

1.5.3 In-Flight Decay Method

The in-flight decay experiment was developed to perform the radioactive decay studies of proton-unbound nuclei with lifetimes ps to ns where the conventional implantation and missing mass methods cannot be used. The idea of the in-flight decay technique is schematically outlined in Figure 1.4(a). Here the 2*p* decay of ^{19}Mg is shown as an example. The ^{19}Mg ions can be produced via one-neutron knockout from ^{20}Mg ions. After a short flight path, ^{19}Mg may decay by emitting two protons and a heavy ion (HI) daughter nucleus ^{17}Ne. As seen in Figure 1.4, a tracking detector array can be positioned downstream of the reaction target, which allows to measure the positions of decay products thus to reconstruct their trajectories.

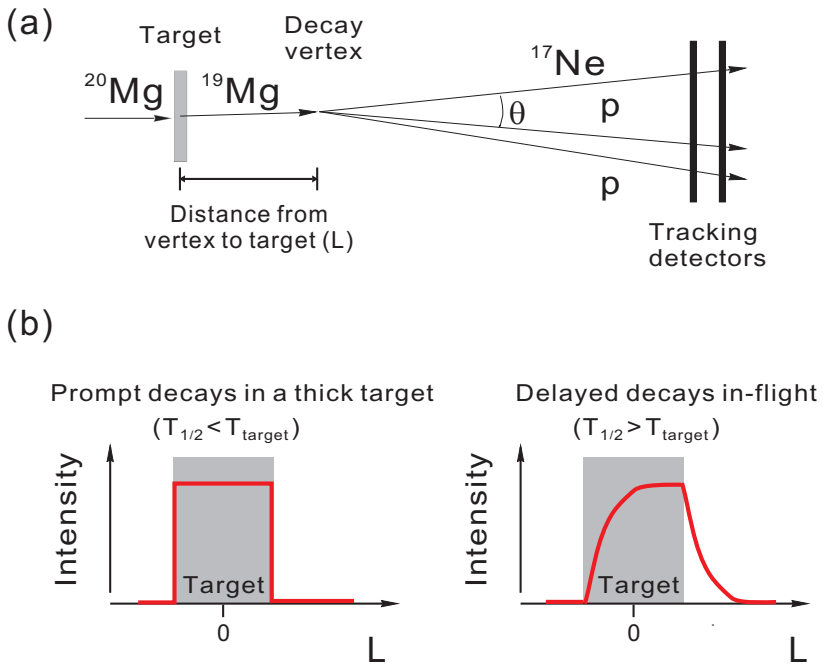

Figure 1.4: Principle of in-flight decay experiments exemplified by the decay of ^{19}Mg. (a) Schematic layout of detectors used to track the two-proton decay of ^{19}Mg in-flight and derive its decay vertex. (b) A sketch of two ideal vertex profiles of prompt decay and delayed in-flight decay, respectively. See text for details.

Based on the measured trajectories of protons and of the heavy recoil ion, the coordinates of each decay can be defined as the vertex of three fragments' trajectories, i.e., the point of closest approach of trajectories of three products. Depending on the decay time, the measured decay vertex distribution normally can be divided into two components, which are schematically shown in Figure 1.4(b). One is characterized by a uniform distribution within the reaction target which corresponds to the so-called prompt decay case, e.g., the dissociation of ^{20}Mg into the nonresonant $^{17}\mathrm{Ne} + p + p$ continuum and prompt decay of very short-lived states in ^{19}Mg inside the target. In the prompt decay case, the half-life ($T_{1/2}$) of the decay is normally much smaller than the flight time for the ion passing through the target (T_{target}). Another component is expected to exhibit "growing" and "decay" curves along the beam direction which may be due to the radioactive decays of relatively long-lived ^{19}Mg g.s. [21]. Such a delayed-decay component is analogous to counting the decay products as a function of time in a standard radioactivity experiment. The half-life value of the decay can be derived by fitting an exponential function to the vertex profile. In order to disentangle the prompt and delayed decay components, a precise measurement of all fragment trajectories is required, which allows for reconstructing each decay vertex accurately [86].

Besides the half-life of the 2*p* precursor may be extracted from the measured decay vertex distribution, the spectroscopic information on the state of the precursor may be deduced from the measured angles between the trajectories of decay products (e.g., θ in Figure 1.4(a)). Generally, the states of 2*p* precursor can undergo sequential two-proton emission or direct 2*p* decay. In the former case, the decay process can be reduced to a sequence of two single-proton emissions, i.e., two sequential two-body decays. In the latter case, the three-body decay kinematics should be considered. In the following, the principle of the in-flight decay spectroscopy for investigating 2*p*-unbound nuclei via the measurement of angular correlations of the decay products (e.g., angular HI-*p* correlation) is described. The kinematics concerning the above-mentioned two decay processes, i.e., two-body decay and three-body decay, are briefly introduced. Throughout this subsection units are used in which $\hbar = c = 1$.

First let us consider the sequential 2*p* decay case. As mentioned previously, it actually includes two two-body decays. A general description of two-body decay kinematics can be found in many references, e.g., [87]. Here, we briefly introduce the kinematics concerning the single-proton emission, which is applicable to sequential emission of protons. The decay products of single-proton emission include a proton and a HI daughter nucleus. In the rest frame of the mother nucleus (rest frame), the momentum vector (hereafter $\vec{p}_{\text{cm}}$) of proton and HI are equal in magnitude and opposite in direction because of the momentum conservation. According to the energy conservation, the magnitude of $\vec{p}_{\text{cm}}$ is given by

$$\begin{aligned} p_{\text{cm}} &= \frac{1}{2M}\sqrt{[M^2-(m_p-m_{\text{HI}})^2][M^2-(m_p+m_{\text{HI}})^2]} \\ &= \frac{1}{2M}\sqrt{(M+m_p-m_{\text{HI}})(M-m_p+m_{\text{HI}})(M+m_p+m_{\text{HI}})Q}, \end{aligned} \quad (1.2)$$

where M, m_p, and m_{HI} are the mass of the mother nucleus, the mass of the proton, and the mass of the HI, respectively. The quantity Q is the decay energy of the mother nucleus, which is given by $Q = M - m_p - m_{\text{HI}}$. The above equation indicates that in the rest frame the magnitude of the momenta of decay products and hence also their energies are determined by the masses of the three particles. In the laboratory frame (lab frame) which the z axis is along the direction of flight of the mother nucleus, the magnitude of decay product's momentum can be also obtained by requiring energy and momentum conservation. For instance, the magnitude of the proton momentum ($\vec{k}_p$) is given by

$$k_p = \frac{(M^2+m_p^2-m_{\text{HI}}^2)P\cos\theta_p \pm 2E\sqrt{M^2p_{\text{cm}}^2 - m_p^2P^2\sin^2\theta_p}}{2(M^2+P^2\sin^2\theta_p)}. \quad (1.3)$$

In equation 1.3, P is the magnitude of the momentum ($\vec{P}$) of the mother nucleus, E is the energy of the mother nucleus, which is given by $E = \sqrt{M^2+P^2}$, θ_p is the polar

angle of the proton, i.e., the angle between $\vec{k}_p$ and z axis. If P is very large and $p_{\rm cm}$ is relatively small (i.e., the velocity of the mother nucleus in the lab frame is much larger than the velocities of the decay products in the rest frame.), the condition $\frac{Mp_{\rm cm}}{m_p P} < 1$ is fulfilled. In such a case, an immediate result from equation 1.3 is that there is a maximum value of proton polar angle $\theta_p(\max)$, because the reality of k_p demands the $M^2 p_{\rm cm}^2 - m_p^2 P^2 \sin^2\theta_p \geq 0$. The $\theta_p(\max)$ is given by

$$\begin{aligned} \sin\theta_p(\max) &= \frac{Mp_{\rm cm}}{m_p P} \\ &= \frac{\sqrt{Q}}{2m_p\sqrt{T}}\sqrt{\frac{(2m_p+Q)(2m_{\rm HI}+Q)(2m_p+2m_{\rm HI}+Q)}{T+2(m_p+m_{\rm HI}+Q)}}, \end{aligned} \quad (1.4)$$

where T is the kinetic energy of the mother nucleus in the lab frame, and it is given by $T = \sqrt{M^2+P^2} - M$. If the mother nuclei are mono-energetic (i.e., constant T), the $\theta_p(\max)$ is determined by the Q value and the masses of the three particles according to the above equation. Generally, for the decay of a high-energy nucleus, Q is a small quantity (of the order a few MeV) in comparison with $m_p, m_{\rm HI}$, and T, one can perform the Taylor's expansion in $\sqrt{Q}$ for the expression in the right-hand side of equation 1.4 and the leading order result is

$$\sin\theta_p(\max) \approx \sqrt{\frac{2m_{\rm HI}(m_p+m_{\rm HI})}{m_p T[T+2(m_p+m_{\rm HI})]}}\sqrt{Q}. \quad (1.5)$$

The above expression illustrates that the maximum value of polar angle in the lab frame is approximately proportional to the square root of mother nucleus's decay energy.

Given the fact that the mass of a heavy decay product (e.g., ^{17}Ne) is normally much larger than the mass of the proton, in the lab frame, the polar angle of HI $\theta_{\rm HI}$ is much smaller than θ_p, i,e., $\theta_{\rm HI} \ll \theta_p$. Therefore, the angle between the momenta of HI and proton ($\theta_{\text{HI-}p}$) in the lab frame is given by

$$\theta_{\text{HI-}p} = \theta_p + \theta_{\rm HI} \approx \theta_p. \quad (1.6)$$

The above equation demonstrates that the maximum value $\theta_{\text{HI-}p}(\max)$ of $\theta_{\text{HI-}p}$ approximately equals to the maximum value of proton polar angle $\theta_p(\max)$, which is determined by equation 1.4. Such a situation is schematically shown by Figure 1.5(a), which illustrates the kinematics for the simple case of isotropic and mono-energetic one-proton emission from a high-energy precursor, e.g., ^{18}Na. The momentum distribution of HI in the lab frame is centered around the momentum of the mother nucleus. The kinematic enhancement presents at the maximum possible angle between HI and proton $\theta_{\text{HI-}p}(\max)$, where the proton is emitted almost orthogonally relative to the HI's momentum vector. If one can measure the trajectories of proton and HI thus measure the angle

$\theta_{\text{HI-}p}$ precisely, the Q value of the proton emission can be deduced by inspecting the $\theta_{\text{HI-}p}$(max).

Now let us derive the distribution of the angle between the decay products in the lab frame $w(\theta_{\text{HI-}p})$. Starting from the distribution $w^*(\cos\theta^*)$ of the cosine of the decay angle θ^* in the rest frame, the distribution $w(\cos\theta_{\text{HI-}p})$ of the cosine of the angle $\theta_{\text{HI-}p}$ in the lab frame can be obtained by

$$w(\cos\theta_{\text{HI-}p}) = \frac{d\cos\theta^*}{d\cos\theta_{\text{HI-}p}} w^*(\cos\theta^*). \tag{1.7}$$

In case of an isotropic decay in the rest frame, the distribution $w^*(\cos\theta^*)$ is constant: $w^*(\cos\theta^*) = \frac{1}{2}$. The general relation between $\cos\theta^*$ and $\cos\theta_{\text{HI-}p}$ is so complicated due to the Lorentz transformation from the rest frame to the lab frame that we do not write it here. The reader who is interested in the the exact expression is referred to Ref. [87]. For arbitrary masses, it is not easy to uncover the $\theta_{\text{HI-}p}$ dependence of $w(\cos\theta_{\text{HI-}p})$ from equation 1.7. Under the circumstance that the mother nucleus is much heavier than the proton and the decay energy is much smaller than the proton mass, the dependence of $w(\cos\theta_{\text{HI-}p})$ on $\theta_{\text{HI-}p}$ can be approximated by

$$w(\cos\theta_{\text{HI-}p}) \approx \frac{a}{\sqrt{\cos\theta_{\text{HI-}p} - b}}. \tag{1.8}$$

In equation 1.8, a and b are positive constants, which are given by $a = \frac{v}{4}\sqrt{\frac{m_p}{Q(1-v^2)}}$ and $b = 1 - \frac{Q(1-v^2)}{m_p v^2}$, respectively, v is the the velocity of the mother nucleus in the lab frame. Correspondingly, the distribution $w(\theta_{\text{HI-}p})$ can be obtained by

$$w(\theta_{\text{HI-}p}) = \sin\theta_{\text{HI-}p} w(\cos\theta_{\text{HI-}p}). \tag{1.9}$$

Such a distribution is schematically displayed in Figure 1.5(b). Note that equation 1.8 implies the existence of a maximum angle between HI and proton. Moreover, the $\theta_{\text{HI-}p}$ spectrum exhibits a sharp peak at the maximum value $\theta_{\text{HI-}p}$(max). Such typical features are the basis for the analysis of the measured $\theta_{\text{HI-}p}$ distribution in the in-flight decay experiment. By observing the peak position of the $\theta_{\text{HI-}p}$ spectrum, one can obtain the $\theta_{\text{HI-}p}$(max) and thus deduce the decay energy.

Let us turn now to the direct 2*p* decay. This is a three-body decay process and in general nine degrees of freedom are required for the description of three decay products in the final state if spin degrees of freedom are neglected. A comprehensive description of the kinematics concerning the direct 2*p* decay is complicated. As shown in section 1.4, several theoretical models have been developed to describe the decay dynamics of the direct 2*p* decay, such as the SMEC and three-body model. In order to provide some general

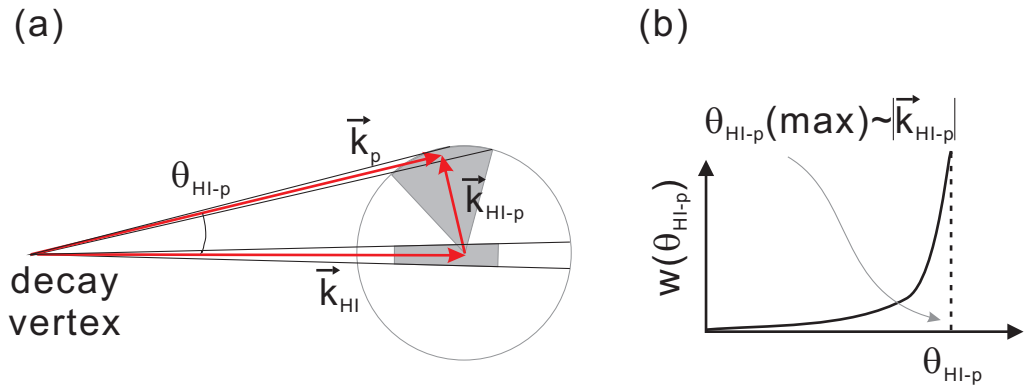

Figure 1.5: (a) Schematic interpretation of the kinematics concerning the isotropic mono-energetic proton emission from an energetic nucleus. $\vec{k}_{\mathrm{HI}}, \vec{k}_p$, and $\vec{k}_{\mathrm{HI}\text{-}p}$ represent the momentum of the heavy ion daughter nucleus, the momentum of the proton, and the relative momentum between proton and HI, respectively. For a given $\vec{k}_{\mathrm{HI}\text{-}p}$, the kinematic enhancement (shaded area) of $\theta_{\mathrm{HI}\text{-}p}$ appears at the maximum possible angle $\theta_{\mathrm{HI}\text{-}p}$(max). (b) Corresponding angular HI-p distribution exhibiting a peak related to the proton decay energy.

features especially the energy and momentum correlations of the 2p decay products, a brief introduction of the three-body model is described here. The detailed descriptions of this model can be found in Refs. [32, 65, 82, 88].

In the three-body model, the dynamics of a system with A particles is reduced to the core+p+p three-body dynamics. Such a three-body system can be investigated by using the Jacobi coordinates defined in the Jacobi system. For example, two "irreducible" Jacobi systems in coordinate and momentum spaces, so-called "T" and "Y" systems, are shown in Figure 1.6. Correspondingly, several Jacobi vectors and correlation parameters are defined in the following:

$$\begin{aligned}
\vec{k}_x &= \frac{A_2\vec{k}_1 - A_1\vec{k}_2}{A_1 + A_2}, \\
\vec{k}_y &= \frac{A_3(\vec{k}_1 + \vec{k}_2) - (A_1 + A_2)\vec{k}_3}{A_1 + A_2 + A_3}, \\
Q_{2p} &= E_x + E_y = \frac{k_x^2}{2M_x} + \frac{k_y^2}{2M_y}, \\
\varepsilon &= E_x/Q_{2p}, \\
\cos(\theta_k) &= \frac{\vec{k}_x \cdot \vec{k}_y}{k_x k_y}.
\end{aligned} \tag{1.10}$$

In these equations, A_1, A_2, and A_3 are the mass number of the decay product 1, 2, and

3 respectively, M_x and M_y are the reduced masses of the X and Y subsystem. $\vec{k}_1$, $\vec{k}_2$, and $\vec{k}_3$ are the momenta of the decay product 1, 2, and 3 in the cartesian system. $\vec{k}_x$ and $\vec{k}_y$ are the Jacobi momenta. Q_{2p} is the total 2*p* decay energy, while E_x and E_y are the energies of the X and Y subsystem. ε is the parameter which describes the energy distribution between any two of the decay products, while θ_k is the angle between the Jacobi momenta.

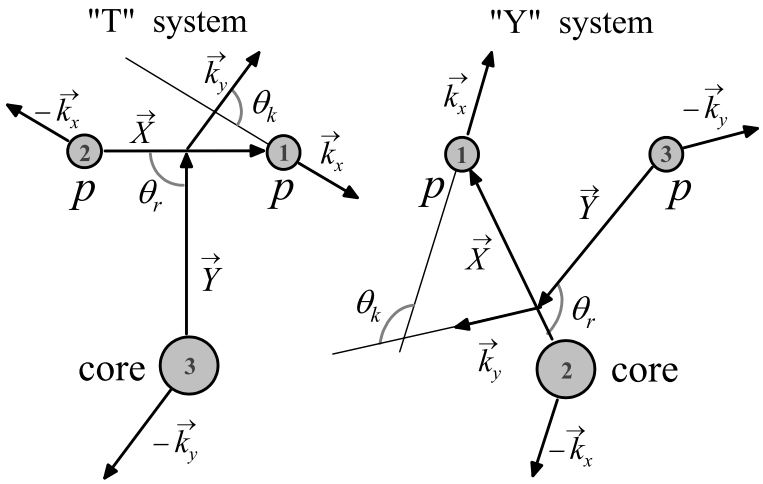

Figure 1.6: Two Jacobi systems, "T" and "Y", with respective kinematical variables used for the description of the core + *p* + *p* three-body system in coordinate and momentum spaces. Figure taken from [82].

Based on the utilization of simplified three-body Hamiltonians, which allows a factorization of the Green's function, the three-body Schrödinger equation is solved by using the hyperspherical harmonics method [89]. Then the distributions of above-listed kinematic variables and correlation parameters can be constructed. These distributions provide insight into the decay dynamics and the structure of the mother nucleus. It is worth mentioning that the distributions in different Jacobi systems are just different representations of the same physical picture.

The three-body model has been successfully applied to describe several true 2*p* emitters, e.g. ^{6}Be [31,90], ^{16}Ne [33,91], ^{19}Mg [18,58,92,93], and ^{45}Fe [94]. Despite the fact that the structures of these 2*p* precursors are different, some general features of direct 2*p* decay were revealed. Among them, a very important feature concerning the energy (or momentum) correlations between two protons is that in "Y" Jacobi system the particles are concentrated at $\varepsilon \sim 0.5$ (when energies of two protons are equal) [9, 64, 82]. Such a feature can be clearly seen from Figure 1.7(a), which shows the energy distributions between core and one of the protons in "Y" Jacobi system for several true 2*p* emitters

calculated by using the three-body model [82]. It is evident that all the distributions have a practically symmetric peak, which indicates two protons emitted in the direct 2*p* decay tend to have similar energies. One obvious reason for this feature is the permutation symmetry between two protons. This feature agrees with the general prediction of Goldansky that the energies of both emitted protons in direct 2*p* decay should preferentially be equal [6], and it is regarded as a genuine signal of true two-proton decay. Due to such an energy correlation, the transverse momentum correlation between two protons is expected to be located along an arc area whose radius reflects the Q_{2p}. Since the angular correlation reflects the transverse momentum correlation, the decay energy of the parent state of the mother nucleus can be derived from the measured angular correlations [68, 95]. As an example, Figure 1.7(b) shows the distributions of the angle between ^{17}Ne and the protons for the direct 2*p* decay of ^{19}Mg ground state. The experimental angular *p*-^{17}Ne spectrum (dots with error bars in Figure 1.7(b)) exhibits a narrow peak and the shape is practically similar as the calculated energy distribution for ^{19}Mg by the three-body model (pink curve in Figure 1.7(a)). The 2*p* decay energy of ^{19}Mg g.s. was determined by comparing the angular ^{17}Ne-*p* correlation predicted by the three-body model (solid curve in Figure 1.7(b)) and the experimental data. Such a procedure is similar to the identification of the reaction channel by using the Dalitz plot and it will be briefly described in chapter 5. The detailed explanation of the procedure can be found n Refs. [68, 95].

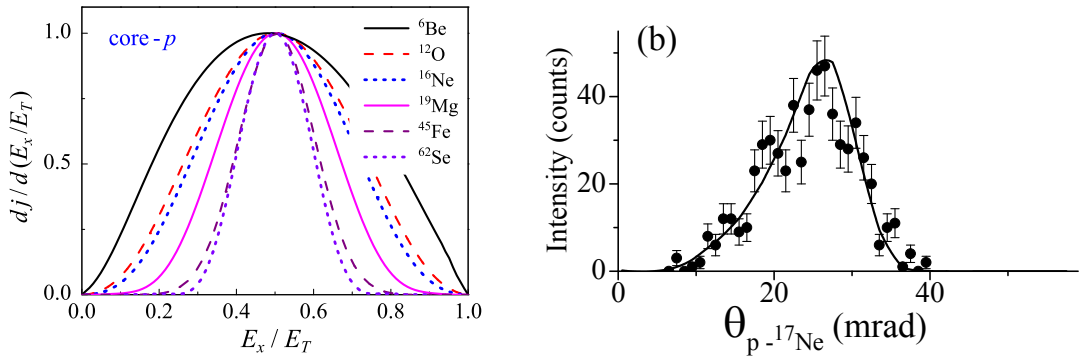

Figure 1.7: (a) The energy distributions between core and proton ("Y" Jacobi system) for several true 2*p* emitters predicted by a three-body model. One may notice that the heavier the nucleus is, the narrower is the distribution. Figure taken from [82]. (b) The distributions of the angle between ^{17}Ne and proton for the direct 2*p* decay of the ^{19}Mg ground state. The dots with error bars show the experimental data and the the solid curve displays the best-fit simulation of the three-body model by assuming $Q_{2p}(^{19}\mathrm{Mg}) = 0.76$ MeV. Figure taken from [58].

In summary, the in-flight decay spectroscopy by the tracking technique is based on the

measurement of the angular correlations between decay products. Valuable information concerning the decay of the parent nucleus such as the Q value can be extracted. This kind of experimental technique has been successfully employed for the investigation of 2*p* radioactivity. In 2007, the tracking technique was applied at the Fragment Separator in GSI for the first time to study the two-proton radioactivity of the sd-shell nucleus ^{19}Mg. In order to check the validity of the in-flight decay method, the 2*p* decay of known g.s. of ^{16}Ne, the 1*p* decay of several known states of ^{15}F, and the 1*p* decay of known g.s. of ^{19}Na were studied. The deduced decay energies [68] are in quantitative agreement with the literature value obtained by the different experimental methods. Moreover, a previously-unknown excited state of ^{16}Ne at 7.6(2) MeV was observed, which was confirmed later by another experiment using the invariant mass method [19]. The decay energy of this new ^{16}Ne level measured by two experiments agrees well. These calibration studies demonstrate that the in-flight decay method is a technique for the precise investigation of the two-proton decays. After testing the experimental procedure, the 2*p* radioactivity of ^{19}Mg g.s. was discovered by measuring the trajectories of all decay fragments [21]. Several excited states of this 2*p* emitter were observed by means of the in-flight decay spectroscopy [58, 68].

There are several advantages of in-flight decay experiments for searching the two-proton radioactivity. First, a straightforward derivation of the lifetime and the measurement of fragment correlations may be achieved simultaneously. Therefore, the in-flight decay measurement can provide informative results. Second, in comparison with the implantation method, more intensive production of 2*p* emitter is expected in the in-flight decay experiment. Compared with the missing mass or invariant mass method, the in-flight decay method allows for using a thicker reaction target (of 2 to 5 $\mathrm{g/cm^2}$) because the projectile straggling in the target does not affect the precision of half-life extraction. Last but not least, the decay energy of narrow states in the 2*p* precursor or intermediate resonances of 1*p* nucleus can be relatively precisely deduced from the measured angular correlations in a broad energy range [86].

1.6 Motivation

As a newly-discovered exotic decay mode, two-proton radioactivity provides a novel tool for nuclear structure studies at and beyond the proton drip-line. It may also play a certain role in the studies of nuclear astrophysics [96]. An example is the so-called "waiting point" nuclei in r*p*-process, which may be bridged via (2*p*, γ) reactions. Since two-proton decay is the inverse process of (2*p*, γ), the investigation of 2*p* decay may provide insight into these nucleosynthesis processes [97, 98]. Two-proton radioactivity has triggered many experimental developments and theoretical activities. For example, the in-flight decay method by tracking was initially developed for the in-flight 2*p* decay

experiments. Nowadays, a certain level of knowledge has been achieved on 2*p* decay studies. However, future experiments and improved theoretical models are called for better understanding of this decay mode. As an experimental search for 2*p* radioactivity of exotic nuclei, the present work attempts to study a previously-unknown *sd*-shell nucleus ^{30}Ar which is predicted to be a candidate for 2*p* radioactivity [82]. Since the in-flight decay spectroscopy has been successfully applied in the discovery of the *sd*-shell true 2*p* emitter ^{19}Mg, therefore we adopted this technique again in order to investigate the decays of ^{30}Ar. The experiment was performed at the Fragment Separator. The contents of the present thesis are mainly based on the analysis of the data obtained in this experiment. In the next chapter, the experimental setup and experimental procedure will be described. Afterwards, the calibration and alignment of the tracking detectors will be demonstrated. Then the main results of data analysis will be given followed by some discussions. Finally, a summary of the present work and an outlook on future radioactivity studies will be stated.

2 Experimental Setup

2.1 Experimental Objectives

In August 2012, the experiment S388: "Two-proton decay of ^{30}Ar" was performed at the Fragment Separator of GSI. The main purpose of this experiment was to search the unknown nuclide ^{30}Ar and to study its decay. This chapter introduces the experimental setup employed in the experiment.

2.2 The GSI Accelerator Laboratory

GSI is a well-known heavy ion research center located at Darmstadt, Germany. The GSI accelerator complex (Figure 2.1) consists of the UNIversal Linear ACcelerator (UNILAC) coupled to the heavy-ion synchrotron (SIS18) [99]. The UNILAC can accelerate ions of all kinds up to 20 percent speed of light (60000 km/s). The ions from UNILAC can be directly used for some experiments, e.g. for the synthesis of new elements. Alternatively, the ion beam from UNILAC can be injected into the SIS18 for further acceleration. The SIS18 can accelerate all ions, from proton to uranium, to a maximum magnetic rigidity of 18 Tm, which corresponds to an energy of 4.5 GeV in the case of protons and 1 GeV/u in the case of $^{238}U^{73+}$. Primary beams from SIS18 are transported to the production target at the entrance of the FRagment Separator (FRS) [100], where high energy secondary radioactive ion beams can be produced via projectile fragmentation or fission. The secondary fragments can be spatially separated with the FRS and then investigated at the different focal planes of the FRS, or can be injected into the Experimental Storage Ring (ESR) [101], or can be transported to other experimental facilities.

2.3 The Fragment Separator FRS

The FRS is an in-flight magnetic separator and spectrometer for radioactive ion beams and it consists of several bending dipole magnets, focusing quadrupole magnets and sextupole magnets, the latter for 2nd-order correction. The layout of the FRS together with its several focal planes (F1 to F4) is displayed in Figure 2.2. The FRS is usually employed for the production and selection of exotic ion beams resulting from fragmentation reactions. The procedure is briefly described below.

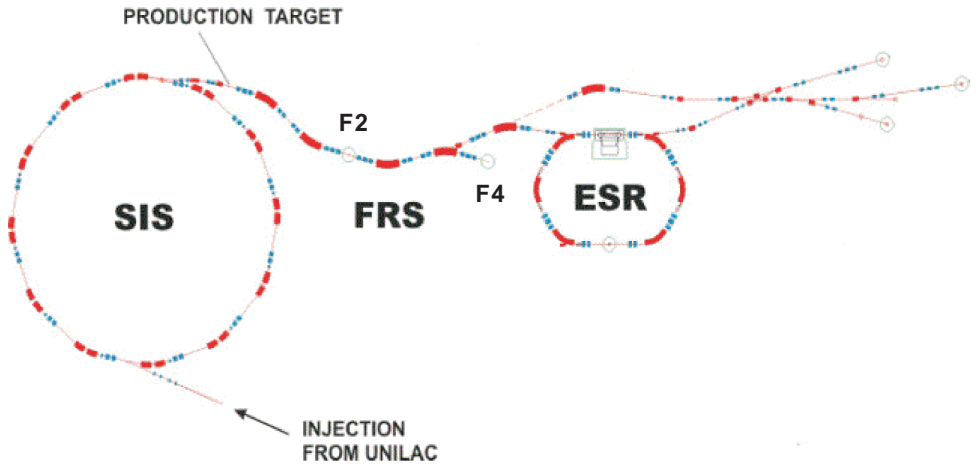

Figure 2.1: Schematic view of the GSI accelerator facility. The beam from UNILAC can be injected into the SIS18 for further acceleration up to relativistic energies. At the entrance of the FRS, the primary beam interacts with the production target, and the produced secondary beam can be transported to the different focal planes (e.g, F2 and F4) of the FRS or to the ESR or to other experimental facilities. Figure based on [102].

The high-energy beams extracted from SIS18 are magnetically guided onto the production target which is located in front of the FRS (see Figure 2.2). Depending on the velocity and ion species of the primary beam, a wide range of isotopes is produced as the result of the nuclear fragmentation reactions. With the combination of the magnetic rigidity ($B\rho$, B is the magnetic field which is uniform and orthogonal to the particle trajectory, and ρ is the deflection radius.) analysis and the ionization energy loss (ΔE) in the degrader, the fragments of interest can be chosen in the FRS by employing the so-called $B\rho - \Delta E - B\rho$ method. Then the selected secondary exotic beams can be investigated either within the FRS, e.g., at focal planes F2 and F4, or can be delivered to further experimental setups, such as ESR.

During the present experimental search of ^{30}Ar, the primary 885 MeV/u ^{36}Ar beam with an intensity of 2×10^9 pps was accelerated by the SIS18 and guided to impinge on a 8 $\mathrm{g/cm^2}$ primary ^{9}Be target at the entrance of the FRS. Many kinds of fragments were produced via the projectile fragmentation. For our experimental purpose, the 620 MeV/u ^{31}Ar fragments with an average intensity of 50 pps were selected as the secondary beam and transported by the first half of the FRS to bombard the secondary ^{9}Be target located at the middle focal plane F2. The thickness and the transverse dimension of the secondary target is 4.8 $\mathrm{g/cm^2}$ and 5×5 $\mathrm{cm^2}$, respectively. At the first focal plane F1, an aluminum wedge degrader was installed in order to achieve an achromatic focus-

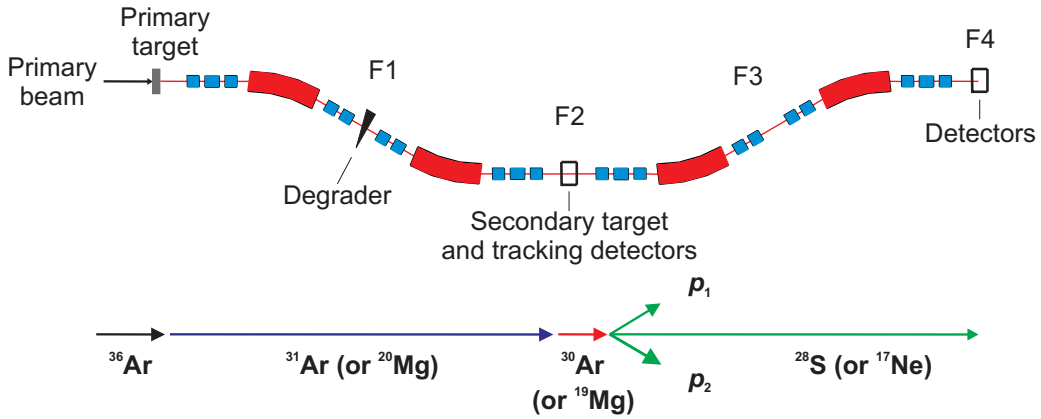

Figure 2.2: Upper part: Layout of the FRS with its several focal planes, F1 to F4. The beam enters from the left and hits the primary target. Large red sectors indicate the bending dipole magnets and smaller blue boxes represent focusing quadrupole magnets. The black triangle shows the wedge-shaped degrader in F1. The locations of detectors used in the experiment are schematically plotted with black boxes in F2 and F4. The detail of employed detectors in the present work is described in section 2.4. Figure based on [103]. Lower part: The reactions of interest concerning the production and decay of ^{30}Ar and ^{19}Mg.

ing of ^{31}Ar at the secondary ^{9}Be target. ^{30}Ar nuclei were produced via one-neutron (1n) knockout from ^{31}Ar ions. The decay products of ^{30}Ar were tracked by a silicon strip detector array placed just downstream of the secondary target. The second half of the FRS was tuned to transmit the heavy ion daughter nucleus, e.g. ^{28}S, down to F4 with high acceptance in angle and momentum. For calibration purposes, the previously-known 2p radioactive nuclei ^{19}Mg were also produced by 1n knockout from ^{20}Mg ions obtained by fragmenting a 685 MeV/u ^{36}Ar beam. Its 2p decay properties were remeasured. Reactions of interest in our experiment are outlined in the lower part of Figure 2.2 and summarized as follows.

- $^{36}\mathrm{Ar}$ projectile fragmentation $^{31}\mathrm{Ar}$ 1n knockout $^{30}\mathrm{Ar} \rightarrow {}^{28}\mathrm{S} + p + p$
- $^{36}\mathrm{Ar}$ projectile fragmentation $^{20}\mathrm{Mg}$ 1n knockout $^{19}\mathrm{Mg} \rightarrow {}^{17}\mathrm{Ne} + p + p$

2.3.1 Ion-Optical Settings of the FRS

In the S388 experiment, the FRS was operated in a separator-spectrometer mode. The first half of the FRS (hereafter TA - F2) was used to separate different ion species resulting from the fragmentation reactions in the primary target. The secondary beam of interest (e.g., ^{31}Ar) was selected and transported to impinge on the reaction target placed at the middle focal plane F2. The outgoing particles from the reaction target were analyzed by the second half of the FRS (hereafter F2 - F4), which was operated

as a magnetic spectrometer. The magnet settings of F2 - F4 were tuned to transmit the targeted ions (e.g., ^{28}S) down to the final focal plane F4. Such an operation mode of the FRS requires a special ion-optical setting, which is briefly described below.

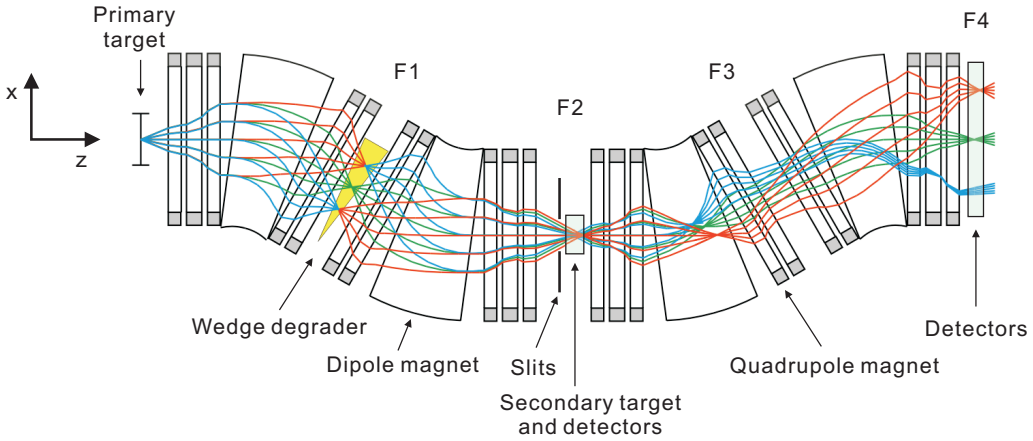

Figure 2.3: Scheme of the FRS ion-optical system. The ion-optical elements of the FRS include dipole magnets and quadrupole magnets. The colored lines represent the calculated trajectories of ^{31}Ar ions of three different energies and of five different angles. The section TA - F2 is achromatic by means of a wedge-shaped degrader placed at F1. The box at F2 denotes the experimental station including secondary target and tracking detectors. The horizontal slits at F2 is displayed. The section F2 - F4 is operated in a dispersive mode and the beam is transmitted to the final focal plane. Detectors for the particle identification are represented by the box at F4. See text for details. Figure based on [104].

Since the transverse dimension of the secondary target and tracking detectors are small, a focused secondary beam is required in the S388 experiment to have a small beam spot on the secondary target. Such a requirement was fulfilled by employing a specially-shaped degrader to invert the momentum deviation (from the reference particle) of the secondary beam. The thickness of the degrader along the optical axis was 5 $\mathrm{g/cm^2}$ [1] and the wedge angle was 194 mrad. Figure 2.3 shows the ion-optical setting of the FRS used in the experiment, which was calculated with the code GICOSY [105, 106]. The colored lines show the trajectories of ^{31}Ar ions of three different energies and of five different angles after production by fragmenting a ^{36}Ar beam on the primary ^{9}Be target. With the combination of the ion-optical elements of the FRS (dipole magnets and quadrupole magnets) and the atomic energy loss in the wedge-shaped aluminum degrader placed at the dispersive focal plane F1, the optical system TA - F2 was tuned to spatially separate the ^{31}Ar fragment beam from other fragments at F1 and to provide an achromatic image at the middle focus F2. Moreover, the horizontal (X) slits at F1 (not shown in Figure 2.3)

[1] This value corresponds to about 20% of the range of ^{31}Ar ion under current experimental condition.

and F2 were employed to assist in rejecting the unwanted ions at F2. The position of X-slit at F1 is ± 14 mm and the position of X-slit at F2 is ± 15 mm. With this setting, the secondary ^{31}Ar beam was selected and transported to F2 with a small beam spot on the secondary target. The second half of the FRS was operated in a dispersive mode. The optical system F2 - F4 was tuned to transmit ^{28}S ions as the centered beam down to F4, where the full Particle IDentification (PID) in A and Z can be achieved.

The transmission properties of the FRS can be described by the calculated longitudinal momentum (p) and angular acceptance. For the section TA - F2, the momentum acceptance ($\Delta p/p$) was limited by closing the slits at F1 to $\Delta p/p = \pm 0.71\%$. The corresponding angular acceptance in the horizontal plane (X plane) was ± 14 mrad, while the angular acceptance in the vertical plane (Y plane) was ± 13 mrad. For a beam starting at F2 and going to F4, the momentum acceptance was $\pm 2.8\%$ and the angular acceptance was ± 20 mrad in both X and Y planes.

2.4 Detector Setup

The main detectors employed in the present experiment are sketched in Figure 2.4. The location of tracking detectors were mainly at the FRS middle focal plane, F2. Two Time-Projection Chambers (TPC1 and TPC2) were used to track the incoming ^{31}Ar (or ^{20}Mg) projectiles. A silicon strip detector (SSD) array which consisted of four large-area SSDs [107] was employed to measure positions of two protons and the heavy recoil ion (^{28}S or ^{17}Ne) resulting from the in-flight 2*p* decay. The position measurement by SSDs allowed us to reconstruct all fragment trajectories and to derive the decay vertex together with angular HI-*p* and *p*-*p* correlations. In the second half of the FRS, the incoming heavy ions were unambiguously identified by their magnetic rigidity determined from the FRS magnet setting and the ions' positions measured with TPCs, time of flight measured with two position-sensitive SCIntillators (SCI1 and SCI2), and energy deposition in an MUltiple Sampling Ionizing Chamber (MUSIC). In addition, an Optical Time-Projection Chamber (OTPC) was installed at F4 to detect beta decays of stopped ^{31}Ar ions. It is worth mentioning that the beta-delayed 3p decays of ^{31}Ar have been observed and investigated [108].

2.4.1 Silicon Strip Detectors for Charged Particle Tracking

SSDs play a key role in the in-flight decay technique because they can provide precise tracking, vertex determination, energy and multiplicity measurement with high efficiency and acceptance [109]. The SSD array employed in the S388 experiment was positioned as shown in Figure 2.5. Two SSDs were placed in-beam, around 55 mm (SSD0) and 65 mm (SSD1) behind the secondary target, with the purpose of tracking and charge-identifying heavy ions down to protons. Another two SSDs were placed

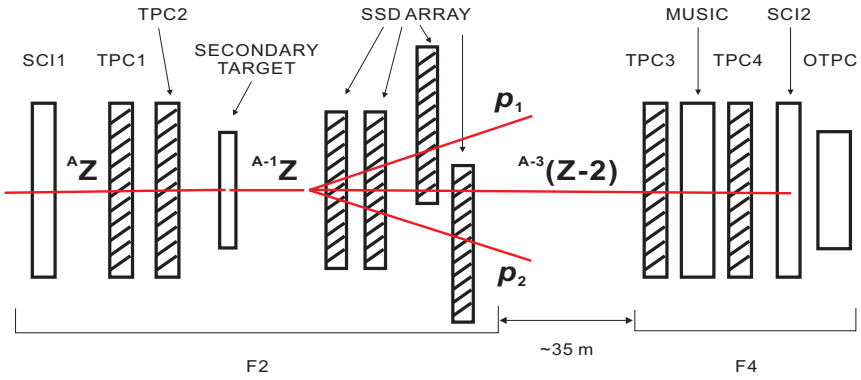

Figure 2.4: Sketch of the detector setup. The secondary beam ${}^{A}Z$ (^{31}Ar or ^{20}Mg) was tracked by TPC1 and TPC2 before impinging on the secondary target. The trajectories of two protons and HI daughter nucleus ${}^{A-3}(Z-2)$ resulting from the decay of 2p precursor ${}^{A-1}Z$ (^{30}Ar or ^{19}Mg) were measured by the SSD array. At the focal plane F4, the energy deposition of HI in MUSIC was recorded. The time-of-flight of HI from F2 to F4 ($\sim$35 m) was measured by using SCI1 and SCI2. The OTPC was employed to study the decays of stopped ions.

about 295 mm (SSD2) and 305 mm (SSD3) away from the secondary target and can be used for set coincidence with the front two detectors.

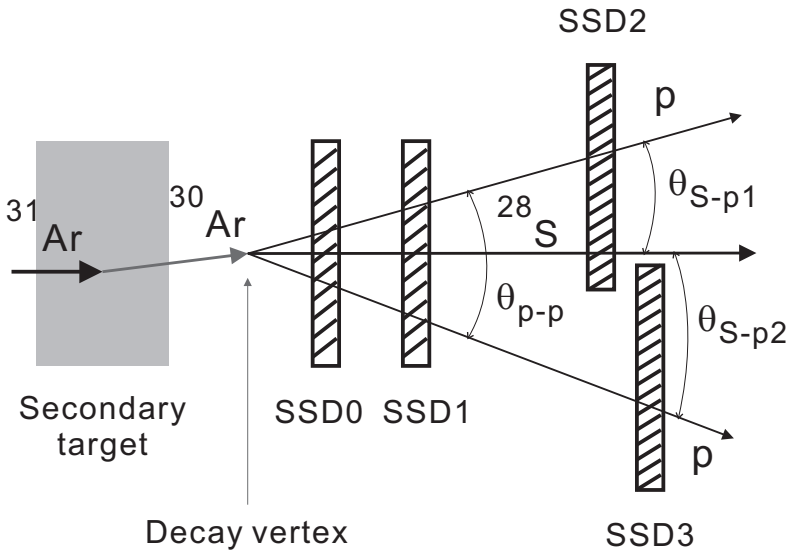

Figure 2.5: Demonstration of tracking 2p decays of ^{30}Ar by using the silicon strip detectors. By measuring the positions of coincident hits of 2p and the heavy fragment, i.e., ^{28}S, the trajectories of all three decay products can be reconstructed. Then the corresponding decay vertex as well as the angular p-p (θ_{p-p}) and HI-p ($\theta_{\mathrm{S-p1}}$, $\theta_{\mathrm{S-p2}}$) correlations can be derived.

The SSDs were developed based on the silicon tracker of the AMS02 [2] project [110]. They were designed especially to possess a large dynamic range. The SSD has a rectangular shape. The demission of the active silicon sensor is 72×41 mm^2 with the thickness of 0.3 mm. The SSD is double-sided and a schematic drawing of its sensor is shown in Figure 2.6(a). The side where strips are perpendicular to the long edge is the junction side (S-side) while the rear side is the ohmic side (K-side). There are 640 read-out strips at a pitch size of $d_S = 110$ µm in the S-side and 384 read-out strips at a pitch size of $d_K = 104$ µm in the K-side. So the total number of read-out strips of one sensor is 1024.

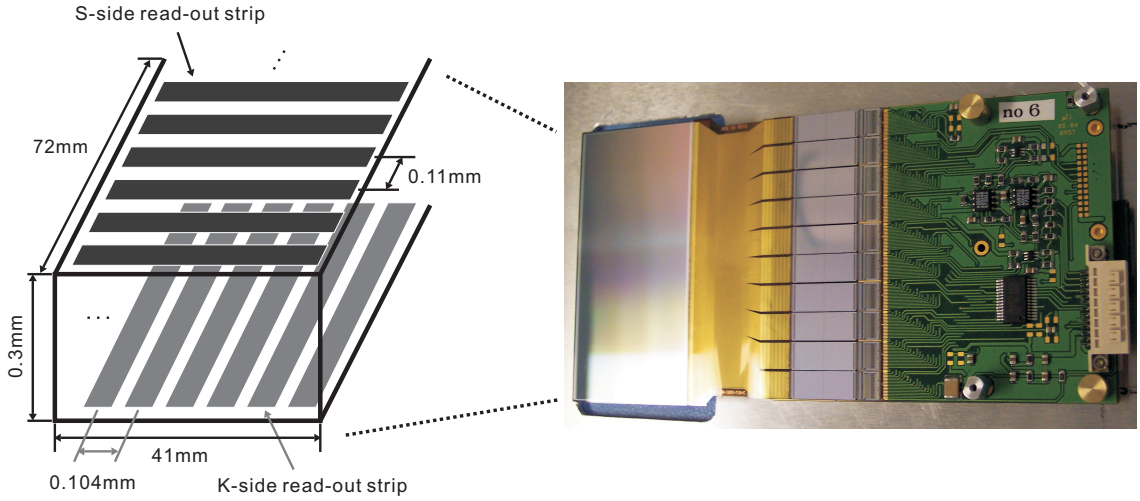

Figure 2.6: (a) Schematic drawing of the active silicon sensor in the SSD [111]. There are 640 read-out strips in the S-side while 384 read-out strips in the K-side. (b) Photograph of a SSD showing from left to right: the silicon sensor, the cable, the coupling capacitors, the VA chips, the front-end electronics, and the S-side connector.

Figure 2.6(b) shows a photograph of the SSD, which consists of an active Si sensor and the attached front-end electronics. It can be seen that the 640 strip signal lines are guided away from the Si sensor and are then subdivided into 10 groups of signal blocks. Every block has 64 lines and they are AC coupled to one VA64_hdr9 chip [112] by 64 channel capacitor chips where every capacitor has 700pF. Similarly, on the back side (K-side), there are five signal blocks connected to 5 VA64_hdr9 chips. The VA64_hdr9 chip is the key component of the front-end electronics. It has 64 analog channels. Each channel corresponds to a individual strip line and it consists of a charge-sensitive preamplifier, a pulse shaper and a sample-and-hold circuitry [111]. All 64 analog channels in one VA64_hdr9 chip are connected to a voltage-current output buffer via an analog multiplexer, which allows the sequential readout of the chip with a speed of 5 MHz. Then the

[2] Alpha Magnetic Spectrometer

serialized differential analog signals are fed into 3 parallel working Analog-to-Digital Converters (ADCs) on a NIM module called SIlicon Strip DEtector REadout Module (SIDEREM) [113]. After digitalization, the raw data is sent to a VME interface module (SAM5) for integration into the GSI Data Acquisition System (DAQ) called Multi Branch System (MBS) [114].

In the experiment, when charged particles penetrate a SSD, electron-hole (e-h) pairs are created in the vicinity of charged particle tracks. The ionization charge is collected by a group of adjacent strips on both S- and K- sides. Such a group of strips is called a cluster. Because more than one strip is involved, the position resolution of such a cluster is usually better than the pitch of the strips. Taking the previous experiment as an example, the resolution of position measured by SSDs was 14 μm for Ne(Mg) ions [68].

2.5 Data Acquisition and Triggers

In our experiment, the data acquisition system was VME-based electronics and consisted of several branches within the GSI MBS framework. The different tasks (e.g., readout, event building, taping) concerning the DAQ were handled by different processors to increase the data recording rate. The readout of digitizers (ADCs, QDCs, etc.) which connected to the scintillators and MUSIC were handled by a RIO-4 processor. The outputs of ADCs and TDCs for TPCs were processed by a RIO-3 processor, while the SSD readout was handled by two RIO-4 processors. The data from these processors were sent to a master PC, which formatted the complete events and controlled the data storage.

Two triggers were used during the S388 experiment. The main trigger was set for the coincidence between the time signal given by SCI1 at the middle focal plane F2 and the SCI2 at the last focal plane F4, i.e., “SCI1 and SCI2”. The purpose of the main trigger is to identify the heavy ion daughter nucleus passing through the second half of the FRS (from F2 to F4) and to spot the in-flight decays. For the calibration purpose, another trigger was defined by the signal from SCI1 but without the signal from SCI2, i.e., “SCI1 and $\overline{\mathrm{SCI2}}$”. These triggers were controlled via a acquisition trigger module.

3 Calibration of Silicon Strip Detectors

In order to achieve the best-possible resolution of position and angle measurement by SSDs, several calibration and alignment procedures were performed. Before the experiment, the performance of SSDs was studied with cosmic rays. In the subsequent data analysis after the experiment, the responses of SSDs to the charged-particle hits were calibrated with the heavy ions. Afterwards, the positions of SSDs were corrected by introducing an offset alignment and a tilt correction in the offline data analysis. In this chapter, the procedure and related results concerning the calibration of SSDs are described.

3.1 Calibration of Silicon Strip Detectors with Cosmic Rays

Before the experiment, a calibration procedure was conducted with cosmic rays to test the performance of SSDs. Given the fact that every SSD has a few dead strips, which cannot be read-out properly or not at all due to aging or a disconnected bonding wire, this calibration procedure is helpful for identifying the dead strips in SSDs.

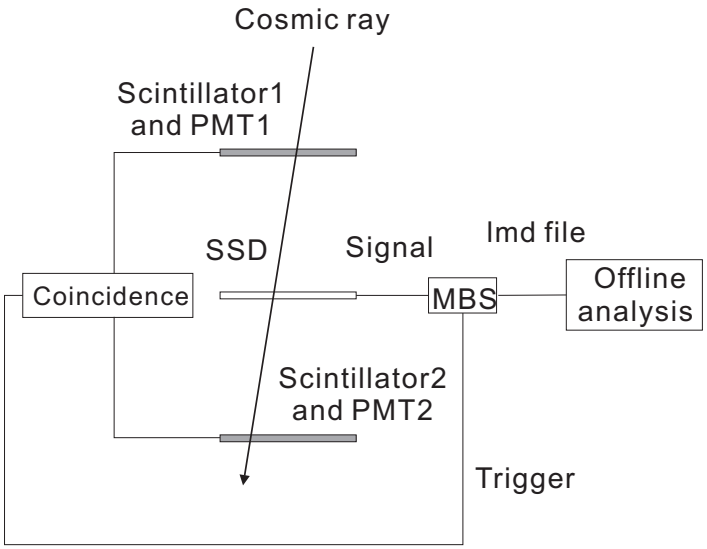

Figure 3.1: Schematic drawing of the setup employed in the calibration procedure.

3.1.1 Description of the Calibration Procedure

The experimental setup is schematically shown in Figure 3.1. Two scintillators were placed above and below the SSD and they were connected by two photomultipliers

(PMT) for signal readout. The coincidence of signals from two photomultipliers was used to provide a trigger for the data acquisition system. In between, the SSD detected cosmic rays (mostly muons) which passed through the whole detection system. All four SSDs were tested and raw data were recoded in terms of list mode data (lmd) files to be used for offline analysis.

3.1.2 Separation of Pedestal Events from Cosmic-Ray Events

Figure 3.2 demonstrates a typical spectrum of the events registered by one strip of a SSD. The main part of the spectrum is normal-distributed ("Gaussian-like") and most of these events correspond to the pedestal (see detail in section 3.2). There are a few events with energy deposition a bit larger than the average pedestal level, and they belong to the incident cosmic-ray particles. Since both real events containing particle hit information and pedestal events recording just pedestals were stored in the same spectrum, it is necessary to separate them. By means of the separated spectrum, one can identify the problematic strips which may be the dead strips. Here "problematic" means the criterion used to identify the dead strips in this section is a necessary but not sufficient condition. The finally dead strips were identified by combining the criterion used here with that in subsection 3.2.3.

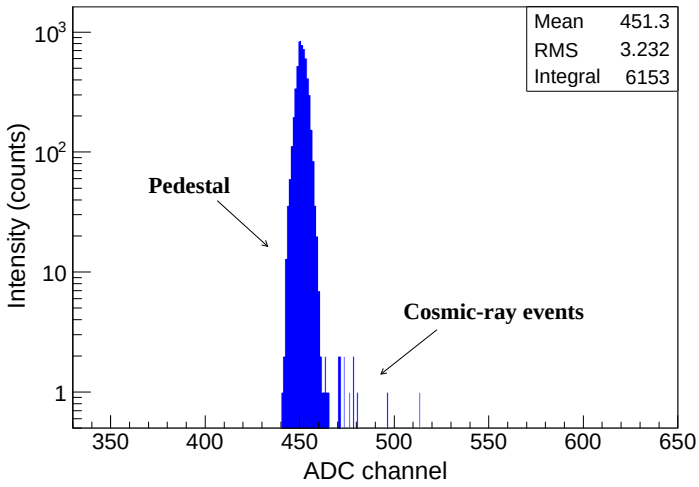

Figure 3.2: Energy deposition distribution of events registered by one strip of a SSD in terms of ADC channels. The main pedestal part can be seen clearly. A few cosmic-ray events with larger energy deposition are observed as well. Note that the y axis is on the log scale.

The separation of real events and pedestal events was performed via the following procedure.

- Calculation of the *mean* and root-mean-square (*rms*) of the energy deposition distribution (raw spectrum) for each strip.
- Usage of a 5*rms* cut for each spectrum. The events with an energy deposition which is within the *mean*∓ 5*rms* correspond to the pedestal (pedestal events), while the events with energy deposition exceeding the *mean*$+5$*rms* belong to cosmic-ray hits.

Based on the strip-by-strip analysis, the pedestal events and real events were separated for a total of 4096 strips in all 4 SSDs. Figure 3.3 displays the pedestal part [panel (a)] and the cosmic-ray event part [panel (b)] which originally belong to the spectrum shown in Figure 3.2.

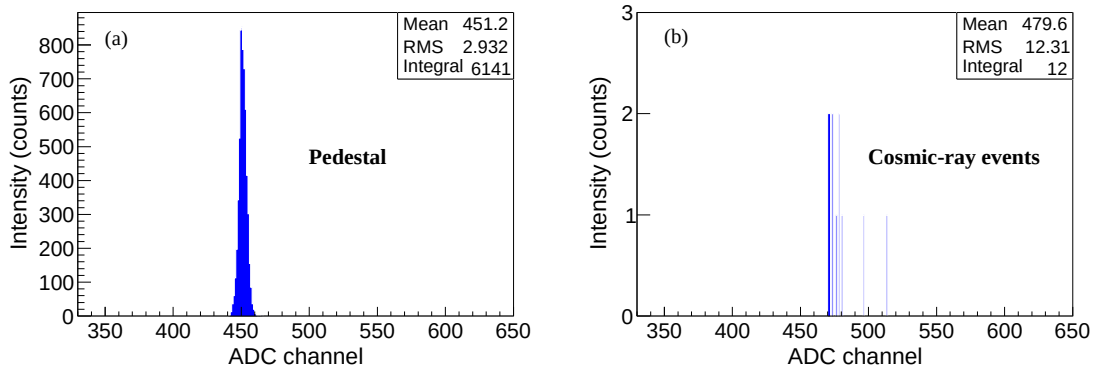

Figure 3.3: Separation of raw spectrum shown in Figure 3.2. (a) Pedestal spectrum. (b) Cosmic-ray hit events.

Combining the "real events" spectrum and the corresponding pedestal spectrum, problematic strips in every SSD can be identified. Given the fact that a large amount of events were accumulated, in principle, the charged particles in cosmic rays (e.g., muons) could be registered by every strip. In this sense, it is very possible that those strips without detected cosmic-ray hits are suspicious. Therefore, the strips which show pedestals only were assigned to be problematic strips. Table 3.1 lists the problematic strips for all 4 SSDs. In comparison with SSD0 and SSD1, it is evident that SSD2 and SSD3 have more problematic strips.

3.2 Pedestal Determination of Silicon Strip Detectors

In a silicon strip detector, 3 ADCs are used for digitizing the analog signals. Two of them are in charge for the S-side signals and the third one is responsible for the K-side signals. The ADC can only handle positive signals. It was found that if an ion deposits

Table 3.1: Problematic strips.

Detector	Problematic strip number
0	640, 800, 801, 907, 935, 937
1	328, 538, 727
2	8, 41, 58, 70, 72, 73, 77, 83, 93, 100, 108, 123, 137, 160, 182, 208, 214, 215, 216, 219, 223, 230, 255, 277, 324, 335, 336, 338, 346, 364, 368
3	6, 32, 77, 108, 181, 189, 297, 346, 374, 375, 490, 509, 514, 560, 593, 604, 643

a large amount of energy in a certain strip of a SSD, sometimes the output signals of neighboring strips dramatically decrease. Such an effect may cause a negative baseline in the output waveform so that the ADC could not work. In order to avoid this situation, the front-end electronics of the SSD in current use was originally designed to set a constant offset for each strip which allows the output signals to be always positive. Even in the case of no passage of charged-particles, the output ADC value is at a certain positive level, typically of 500 ADC channel, which is called a pedestal. Pedestal is useful to avoid the misplacement of the baseline. Since the obtained total signal from each strip always includes the pedestal value, one should determine the pedestal firstly and then subtract it from the total signal in order to obtain the energy deposition of the incident particle.

3.2.1 Calibration for the FRS Experiment

In order to obtain the pedestal for every strip, the front-end electronics of all four SSDs were tested by using a pulse generator before and after the S388 experiment. During these two calibration runs, the output signals of each strip had only the pedestal value because there were no penetrating particles. Therefore, these two sets of data can be employed to determine the pedestal of every strip. As an example, Figure 3.4 shows the pedestal distributions of one strip in the SSD0, which were recorded during the calibration runs before (Figure 3.4(a)) and after (Figure 3.4(b)) the S388 experiment, respectively. Both spectra show "Gaussian-like" patterns and they have almost the same *mean* value and only slightly different *rms* value, which demonstrate a stable pedestal of this strip.

3.2.2 Determination of a Pedestal for Each Strip

On the basis of the event-by-event analysis, one can determine the pedestal and average noise level for each strip, which are defined by the *mean* and *rms* of the pedestal distribution, respectively. As an example, Figure 3.5 displays the pedestal value (in units of

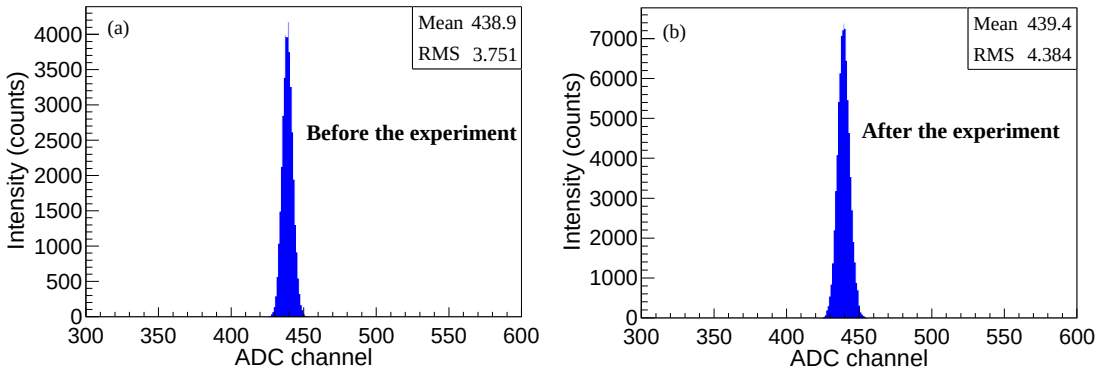

Figure 3.4: Pedestal distributions of one strip in SSD0 measured before (a) and after (b) the experiment. See text for details.

ADC channel) obtained for all strips in the SSD0 based on the data recorded during the calibration runs before (Figure 3.5(a)) and after the experiment (Figure 3.5(b)), respectively. In comparison of the two patterns, we found that the pedestal values for a certain strip obtained before and after the experiment are similar. A typical pedestal level is around 500 ADC channels. The 16-cluster feature in both patterns are attributed to the readout electronics of the SSD, i.e., every 64 strips are connected to a VA64_hdr9 chip and a total of 16 VA64_hdr9 chips are in one SSD.

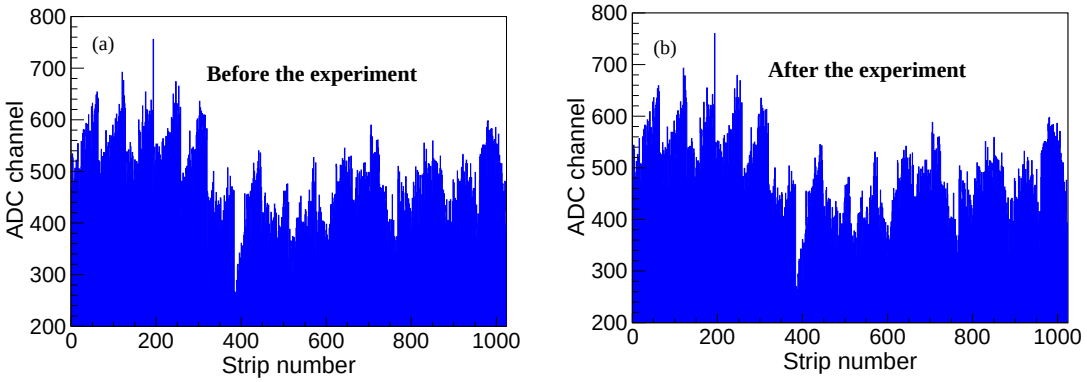

Figure 3.5: Pedestal of all strips in the SSD0 measured before (a) and after (b) the experiment. See text for details.

Similar as Figure 3.5, Figure 3.6 shows the average noise level of all 1024 strips in the SSD0. It is obvious that the patterns of strip noise obtained by analyzing the data taken from the calibration runs before and after the experiment are similar. The three-step structure in both panels is owing to the 3 ADCs used in one SSD. One can see that the typical strip noise value of the SSD0 is around 6.0 ADC channels for the first half of S-side strips (strip number 0-319) and around 4.0 ADC channels for the second half of

S-side strips (strip number 320-639) as well as 4.5 ADC channels for the K-side strips (strip number 640-1023).

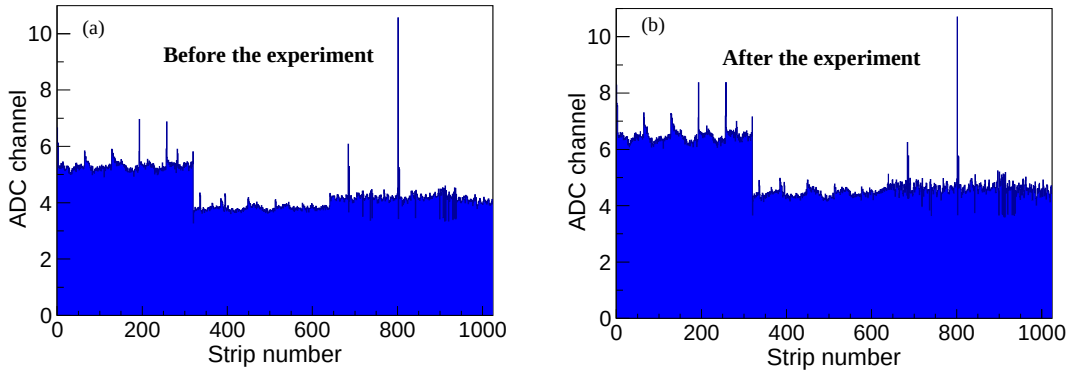

Figure 3.6: Average noise level of all strips in the SSD0 measured before (a) and after (b) the experiment. See text for details.

3.2.3 Identification of Dead and Noisy Strips

As mentioned earlier, every SSD has several dead strips. Since dead strips fail to give a proper response to the particle hit, they must be identified and corrected. Besides the dead strips, an identification of the noisy strips, which give a large noise level, is also needed.

In subsection 3.1.2, the problematic strips have been identified, and they are listed in Table 3.1. The criterion applied there is an essential condition for identifying dead strips. Based on the average strip noise extracted from the data recorded during the calibration runs before and after the S388 experiment, here we added another criterion for the identification of the dead strips, i.e., the average noise level of the dead strip should be smaller by 3*rms* than the *mean* value of the average noise level of strips connected to the same ADC. With the combination of this condition and the one described in subsection 3.1.2, the strips which fulfill the two selection conditions are treated as dead strips. Regarding the noisy strips which always have large noise levels, they are identified if their noise are larger by 3*rms* than the *mean* value of the average noise level of strips connected to the same ADC. By employing these selection rules, the dead and noisy strips for each SSD were identified and they are listed in Table 3.2.

3.3 Calibration of Silicon Strip Detectors with Heavy Ions

In order to obtain the charge identification capability and spatial resolution of SSDs used in the S388 experiment, all four detectors were calibrated with the heavy ions

Table 3.2: Dead and noisy strips.

Detector	Dead strip number	Noisy strip number
0	none	0, 1, 2, 193, 257, 684, 801
1	328	257, 327, 329, 878, 879
2	8, 41, 58, 77, 93, 100, 108, 137, 160, 182, 208, 214, 215, 216, 223, 230, 255	93, 418, 648
3	6, 32, 77, 108, 181, 189, 346, 374, 375, 490, 509, 514, 560, 593, 604	193, 297, 402, 642, 643, 705, 920, 921

which were produced during the experiment. In this section the calibration procedure is described and corresponding results are shown.

In the experiment, the ADC channels of the readout strips include a pedestal, a common-mode noise, a strip noise and an event signal. In order to eliminate the influence of random noise and to analyze the true event signal, the following steps were performed during the data processing:

- Subtraction of the pedestals
- Gain correction
- Dead and noisy strips treatment
- Subtraction of the common-mode noise

With the above procedure, the clean event signal can be obtained. Afterwards, the heavy ion cluster will be identified and the so-called cluster integral will be calculated by the following equation:

$$E = \sum_{i=l}^{N} e_i, \tag{3.1}$$

where E is the cluster integral (or total energy deposition) and e_i denotes the signal of a strip (numbered n_i) belonging to the cluster. l represents the first, and N the last strip of the cluster.

3.3.1 Subtraction of Pedestals

Figure 3.7(a) displays the raw data of an event with a single ion hit in the SSD3. The two sharp peaks show strip clusters where the HI impinges on the S- and K-sides of the

SSD3, respectively. The detail on the formation and identification of a cluster will be discussed in subsection 3.3.5.

One can clearly see that the ADC channel given by every readout strip in Figure 3.7(a) includes a pedestal. Thus the first step of data processing is the subtraction of the pedestal for every strip, which has been obtained by analyzing the data from calibration runs (see section 3.2). Given the fact that the experimental conditions for the calibration run just after the experiment are similar to those in the real experiment, the pedestals which were measured after the experiment were employed in the pedestal subtraction.

Figure 3.7(b) shows the event waveform after the pedestals were subtracted from the raw data. Comparing with Figure 3.7(a), the baseline of the pedestal subtracted waveform locates around zero. The small deviations from 0 are attributed to the common-mode noise and the strip noise.

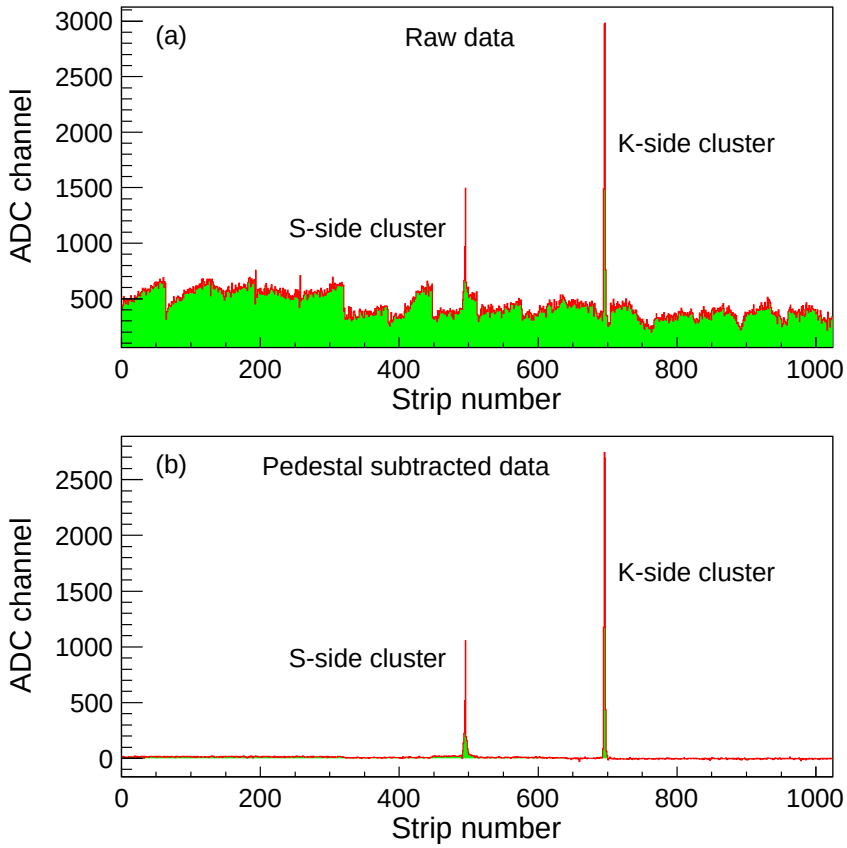

Figure 3.7: Comparison of the raw data (a) and the pedestal-subtracted data (b). The two peaks in both panels correspond to the S-side and K-side strip clusters respectively introduced by a single ion hit.

3.3.2 Gain Correction

After the pedestal subtraction, a correction to the strip's response (or gain) is necessary. Although the channel gains on the same VA64_hdr9 chip are almost uniform, each VA64_hdr9 chip can easily have a different gain due to the unavoidable construction differences in the chips [111]. The gain mismatch among different VA64_hdr9 chips can lead to a distortion of the cluster integral distribution, which decreases the position resolution. The panel (a) of Figure 3.8 displays the cluster integral distribution for ^{28}S ions registered by a series of strips in the SSD0 without the gain correction, and a systematically distorted pattern can be clearly seen. In order to make the chips gain matched, the gain correction was applied for all strips.

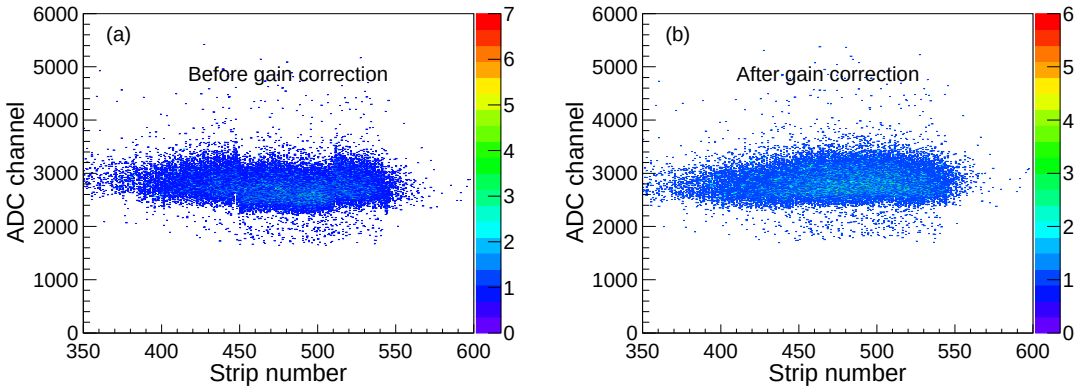

Figure 3.8: Effect of the gain correction. Panel (a) shows the ^{28}S cluster integral distribution versus a series of strips in the S-side of the SSD0 obtained before the gain correction. Panel (b) displays the same distribution after the gain correction.

The correction coefficients were achieved via the following procedure. First, the ^{24}Mg ions produced by the fragmentation of ^{36}Ar beam were adopted to gate the valid events. The reason for choosing ^{24}Mg ions is the large yield of this ion species and its broad spatial distribution in the SSD array. The ^{24}Mg ions were selected to obtain enough clusters for all strips. In the second step, the *mean* of cluster integral for each strip ($Mean_C$) was calculated by plotting the ^{24}Mg cluster integral distribution for that strip. Meanwhile, the total *mean* of the cluster integral for all strips in S-side ($Mean_S$) and K-side ($Mean_K$) were also computed. Finally, the gain correction coefficient (C_g) for each S-side (K-side) strip was calculated by scaling the average cluster integral of a certain strip to that of the whole S-side (K-side), i.e.,

$$C_g = \frac{Mean_C}{Mean_{S,K}}. \tag{3.2}$$

Once the gain correction coefficient was determined, the pedestal-subtracted ADC channel of each strip was divided by the coefficient. By performing the gain correction, the

distortion of cluster integral distribution can be restored. The Figure 3.8(b) displays the effect of the gain correction.

3.3.3 Dead and Noisy Strips Treatment

Based on the pedestal-subtracted data, one can correct the energy deposition recorded by the dead and noisy strips which are identified in subsection 3.2.3. By assuming a linear charge sharing between strips, a linear interpolation method was adopted for the treatment of the dead and noisy strips, i.e., the energy deposition recorded by a dead (noisy) strip was estimated by averaging the energy deposition recorded by the neighboring normal strips. This treatment can be expressed via the following equation:

$$e_i(d,n) = \frac{e_{i-1} + e_{i+1}}{2}, \tag{3.3}$$

where e_{i-1}, e_{i+1} represent the energy deposition (in units of ADC channels) of the normal strip numbered $i-1$ and $i+1$, respectively. $e_i(d,n)$ is the energy deposition of the dead (noisy) strip with the strip number i after the correction. By employing such a treatment for all dead and noisy strips listed in Table 3.2, the distortion of the measured energy deposition distribution due to the dead and noisy strips are recovered.

3.3.4 Subtraction of the Common-Mode Noise

The next step of the data analysis is the subtraction of the common-mode noise. In general, there are two kinds of common-mode noise concerning the SSD data. The first one represents an uniform shift over all strips connected to one ADC via the same output line and we name it pipeline-based common-mode noise. Another kind of common-mode noise indicates a similar shift common to all strips connected to one VA64_hdr9 chip. This can be explained by the fact that every 64 readout strips are AC-coupled to the same VA64_hdr9 chip [110, 111]. We call it chip-based common-mode noise. In this subsection, the calculation and subtraction of the aforementioned two kinds of common-mode noise are illustrated.

As illustrated in section 3.2, 1024 strips of one SSD are connected to 3 ADCs via 3 output lines. Among them, 2 output lines are used to readout the signals from S-side strips. Thus each of them is responsible for 320 strips. Similarly, there is 1 output line which was used to output signals from all 384 strips in K-side to 1 ADC. Due to this configuration, an uniform shift over all strips connected to the ADC via the same output line always appears, i.e, pipeline-based common-mode noise. In our data analysis, after the pedestal subtraction, gain correction, and dead and noisy strips treatment, the average value of the residual signals of strips, which connect to the same ADC via the same output line, was calculated as the pipeline-based common-mode noise for that output line. As the signals of strips involved in a HI cluster include both common-mode noise

and the real event signal, these strips were excluded from the calculations by setting a suitable threshold.

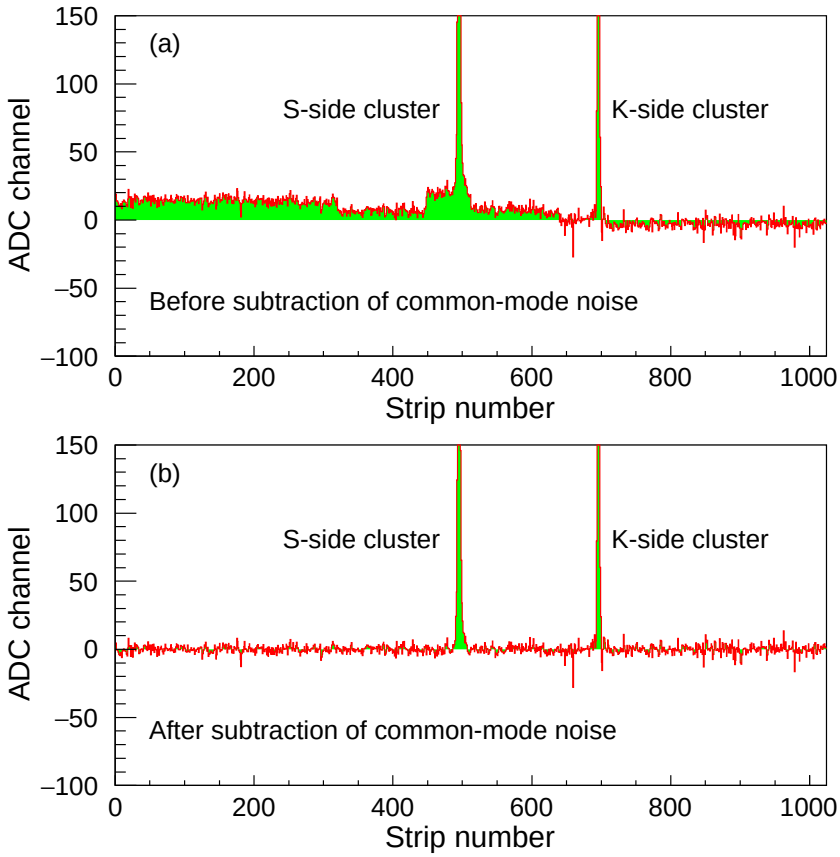

Figure 3.9: Subtraction of the common-mode noise. The signals measured by all strips of a SSD for one event with a single ion hit before (a) and after (b) subtraction of the pipeline-based common-mode noise and the chip-based common-mode noise.

Besides the pipeline-based common-mode noise, there is still another signal shift common to all strips connected to the same VA64_hdr9 chip. As an example, such a shift can be clearly seen in the panel (a) of Figure 3.9 for all the 10 chips in the S-side of one SSD. It is evident that the shift is mainly due to the noise varying chip by chip, i.e., chip-based common-mode noise. One can also observe a slight constant shift common to all strips in the K-side of this SSD, which can be attributed to a pipeline-based common-mode noise. After calculation of the pipeline-based common-mode noise, the chip-based common-mode noise was computed by averaging the signals of every strip which was read out by the same VA64_hdr9 chip. Then the total common-mode noise was obtained by adding the pipeline-based common-mode noise and the chip-based common-mode noise. Afterwards, subtraction of the total common-mode noise was processed for

every strip. The resulted data represent the event signal. Figure 3.9(b) displays the same waveform as shown by Figure 3.9(a) after subtraction of the common-mode noise.

3.3.5 Heavy-Ion Cluster Identification

In the S388 experiment, several kinds of ions were produced in primary and secondary reactions. When these charged particles (e.g., heavy ions or protons) pass a SSD, a number of adjacent strips both on S-side and on K-side are triggered due to capacitive coupling between neighboring strips. Such a group of strips are called a cluster, which collects the ionization charge generated by the incident charged particle. Therefore, the total signal of a cluster (i.e. cluster integral) represents the total energy deposited into the cluster. Panels (a) and (b) of Figure 3.10 display two clusters which were produced in the S-side and K-side of a SSD due to an ^{31}Ar ion hit.

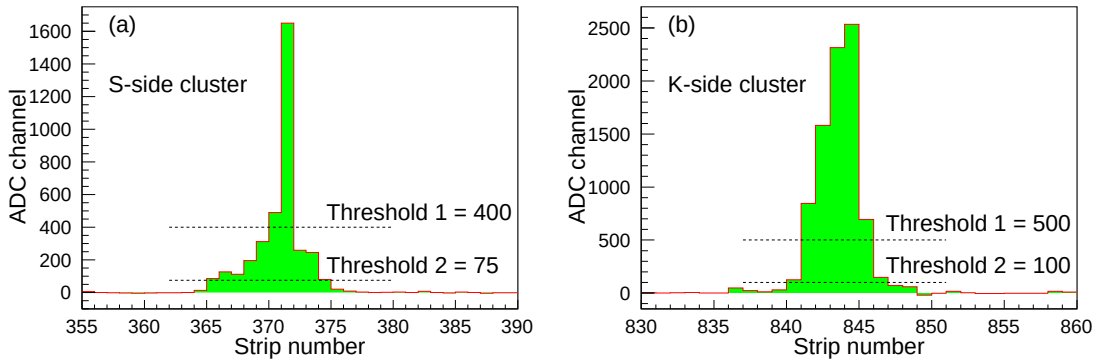

Figure 3.10: The S-side cluster (a) and K-side cluster (b) produced by an ^{31}Ar ion impinging on a SSD. Two thresholds in panel (a) and panel (b) were employed to identify heavy-ion clusters produced in S- and K-sides, respectively.

After performing the pedestal subtraction, the gain correction, the dead (noisy) strips treatment, and the common-mode noise subtraction, heavy-ion clusters were identified. The identification procedure is detailed below:

- A cluster seed was defined at the strip with signal exceeding the first threshold (assumed of 400 ADC channels for the S-side cluster and of 500 ADC channels for the K-side cluster, see Threshold 1 in Figure 3.10).
- The adjacent channels with signals smaller than the signal of the cluster seed but greater than the second threshold (chosen to be of 75 ADC channels for the S-side cluster and of 100 ADC channels for the K-side cluster, see Threshold 2 in Figure 3.10) were included in the cluster.

Based on the event-by-event analysis, all strip clusters caused by ^{31}Ar and ^{28}S ions were identified. Figure 3.11 shows the obtained cluster width (defined as the number

of adjacent strips showing a signal above the second threshold) distribution measured by the SSD1. Since the clusters produced in K-side always have the pronounced central strip, the K-side clusters have a narrower average cluster width in comparison with the S-side clusters.

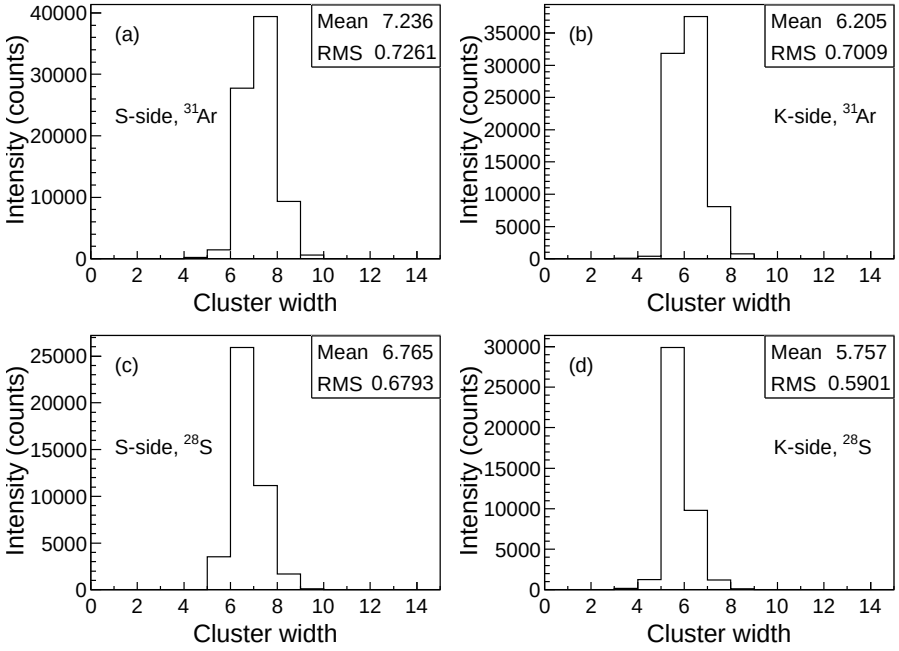

Figure 3.11: Cluster width distribution measured by the S-side and K-side of SSD1.

After the identification of a HI cluster, one can calculate the cluster integral by employing equation 3.1. Figure 3.12 shows the distributions of the ^{31}Ar and ^{28}S cluster integral calculated for the S-side and K-side of SSD1. The distributions from all SSDs are similar.

Once the cluster integral is obtained, the charge-weighted center of gravity (CoG) of a cluster can be computed as:

$$CoG = \frac{\sum_{i=l}^{N} n_i \times e_i}{\sum_{i=l}^{N} e_i} = \frac{\sum_{i=l}^{N} n_i \times e_i}{E}. \tag{3.4}$$

The CoG indicates the cluster position (i.e., the hit position of an ion) in terms of the strip number. By multiplying the strip pitch (i.e., the distance between the centers of two readout strips), one can derive a cluster position $X_{S,K}$ with respect to the center of

the SSD, which can be expressed as

$$\begin{aligned} X_S &= (CoG - 319.5) \times d_S, \\ X_K &= (CoG - 831.5) \times d_K, \end{aligned} \tag{3.5}$$

where the d_S and d_K are the strip pitch in S-side and that in K-side, respectively. The strip pitch is equivalent to the net active width of each readout strip. The value of d_S and d_K can be found in subsection 2.4.1. After the geometric alignment of the detector planes, the position of the HI cluster can be converted to the particle impact position in the lab frame.

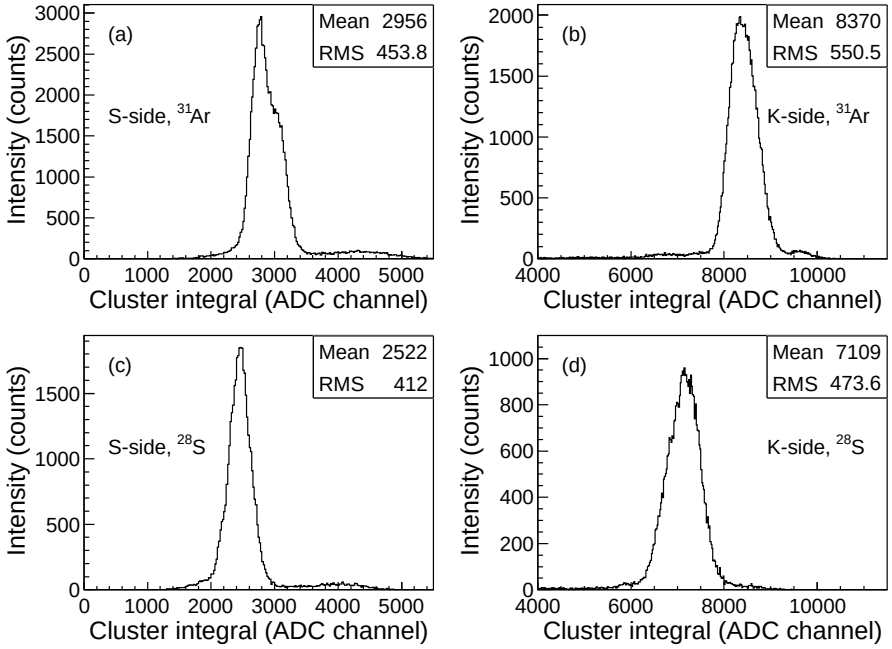

Figure 3.12: Cluster integral distributions from SSD1. Panels (a) and (b) represent the distributions of energy deposition measured by S-side and K-side clusters due to ^{31}Ar hits, respectively. Panels (c) and (d) correspond to the ^{28}S clusters.

3.4 Alignment of SSDs

After calibration of the SSDs, the ion's hit position is given by the CoG which indicates the ion's position with respect to the center of the SSD. In order to obtain the ion's position in the lab frame, the positions of SSDs relative to the lab frame must be taken into account. Considering the possible misalignment of SSDs during the mounting procedure, e.g., the misalignment of the vacuum chamber which was used to hold the SSDs, all four SSDs should be aligned in the offline data analysis, which allows for

a high accuracy of position and angle measurements. Another necessity of the alignment is due to the fact that some SSDs, namely SSD2 and SSD3, were placed off the beam axis (z direction) to cover a larger solid angle for tracking the decay products during the S388 experiment. Such a configuration is schematically plotted in panel (a) of Figure 3.13 which shows the position of four SSDs relative to the secondary target. In order to achieve the ion's hit positions in SSD2 and SSD3 relative to the lab frame, it is necessary to align the centers of SSD2 and SSD3 with respect to the beam axis. In the present work, the alignment of SSDs was performed by two steps. First, all SSDs were shifted with certain small offsets in x and y directions, i.e., an offset alignment was performed. Second, a tilt correction was performed for all SSDs by rotating the detectors around x, y, and z dimensions. A schematic explanation of the offset alinement and the tilt correction is displayed in the Figure 3.13(b).

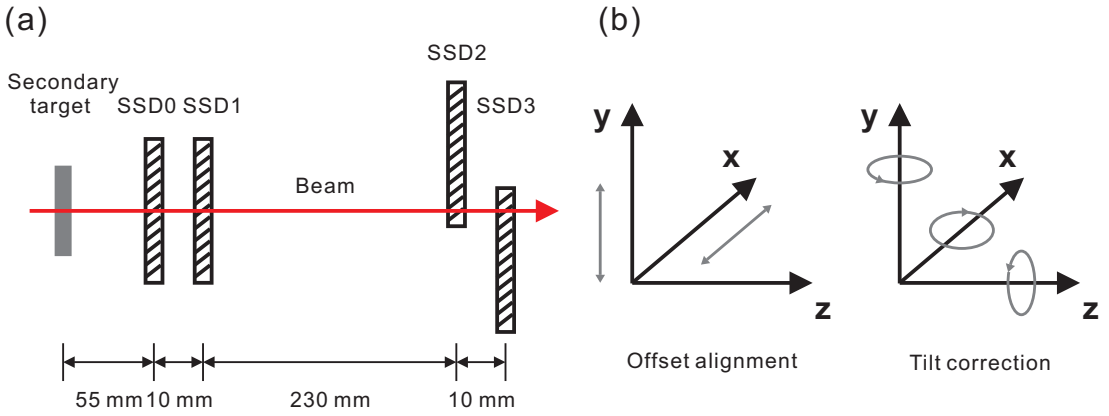

Figure 3.13: Offset alignment and tilt correction. (a) The positions of the SSDs with respect to the secondary target. The beam axis is shown by the red arrow. (b) Schematic explanation of the offset alignment and the tilt correction. See text for details.

3.4.1 Offset Alignment

In principle, the imperfect geometrical alignment of a SSD in three dimensions can be compensated by shifting detector in x, y, and z directions by certain offsets. Given the fact that SSDs measure x and y coordinates of charged ions, while z coordinates of the ions are given by the location of the respective SSD along the beam axis (perpendicular to the SSD plane), which can be relatively precisely measured, the offset alignment was performed only for x and y dimensions. Two steps were processed to obtain the corresponding offsets.

As the first step, we selected the SSD1 as the reference detector and its position was aligned relative to the secondary target's position. Considering that both SSD0 and SSD1 were positioned in the beam line during the experiment, one can choose any of

them as the reference detector. For convenience, the SSD1 was chosen as the reference detector in the present work. As shown in Figure 2.4, two TPCs were located in front of the SSD array during the S388 experiment. These TPCs can measure ion's position with a high resolution which is typically around 200 μm [115, 116]. By utilizing the position information measured by the TPCs for the ions which pass through both TPCs and SSDs, the deviation of reference SSD's center from beam axis can be corrected.

Since the ^{31}Ar ion beam was selected as the secondary beam to pass the first half of the FRS during the experiment, the ^{31}Ar ions were centered at F2. Thus ^{31}Ar ions were employed to obtain the offsets in x and y directions for the reference SSD, i.e., SSD1. By means of the known distances between two TPCs and SSDs as well as two hit positions measured by TPC1 and TPC2 respectively, one can obtain the ^{31}Ar's nominal position in certain SSD by extrapolating the two hits in TPCs to the position in the SSD under a straight-line assumption. This assumption states that "heavy ion's trajectory is a straight line". Then the extrapolated x and y coordinates were compared with the real one measured by SSD1, and the difference between them were calculated. The distributions of x- and y-coordinate difference were plotted after accumulating a large amount of events. The *mean* values of the distributions were adopted as the offset in x and y dimensions for SSD1, respectively. Afterwards, the SSD1 was aligned both in x and in y directions according to the respective offsets.

After the offset alignment of the reference SSD (i.e., SSD1) with the help of TPCs, the positions of other SSDs (i.e., SSD0, SSD2, and SSD3) were aligned with respect to the SSD1, i.e., an adjustment to other SSDs' position relative to the SSD1. In order to obtain the offset for such an alignment, a lot of events with ^{31}Ar ions passing through all four SSDs were selected. The x and y coordinates of ^{31}Ar obtained by the SSD0, SSD2, and SSD3 were compared to those obtained by SSD1, and the corresponding differences were computed. The distribution of coordinate difference was plotted, and the *mean* value of the coordinate difference was adopted as the offset for a certain detector with respect to SSD1.

The offsets for the alignment of all four SSDs are shown in Table 3.3. One may notice that the offsets in y direction for SSD2 and SSD3 are much larger than those for SSD0 and SSD1. The reason is due to the fact that the centers' locations of SSD0 and SSD1 were in the beam line, while the centers' locations of SSD2 and SSD3 were shifted off the beam up and down respectively.

3.4.2 Tilt Correction

Besides the offset alignment, another kind of alignment which concerns the orientation of SSDs is still necessary. Due to the possible misalignment of the vacuum chamber

Table 3.3: Offsets and rotation angles for the alignment of the SSDs.

SSD	0	1	2	3
Offset in x (mm)	-0.9325	-2.1	3.513	1.1592
Offset in y (mm)	0.4189	1.2870	18.0951	-17.0261
Rotation around x (mrad)	1.0	1.0	1.0	1.0
Rotation around y (mrad)	0.2	0.2	0.2	0.2
Rotation around z (mrad)	0.2	8.5	0.1	0.1

used for holding the SSDs or an inaccurate mounting of SSD itself, the orientation of a SSD may deviate from its nominal position. Such a misalignment can be restored by applying a tilt correction in the offline data analysis. The events with single ^{31}Ar ion crossing all four SSDs were selected, and the trajectory of every ^{31}Ar ion was reconstructed by using the coordinates measured by SSDs. Since SSD0 and SSD1 were located just behind the secondary target, while SSD2 and SSD3 were placed a bit far from the secondary target (see Figure 3.13(a)), the ^{31}Ar ion's trajectory was reconstructed by combining the ion's position in one of the SSDs near the target (SSD0 or SSD1) and the ion's position in one of the SSDs far away from the target (SSD2 or SSD3). Then the x and y coordinates of an ^{31}Ar ion in the secondary-target plane were derived from the two alternative trajectories given by the different SSD pairs, e.g., SSD0 - SSD3 and SSD1 - SSD3. The differences δx and δy should be very small since the trajectory of a high-energy ^{31}Ar ion almost follows a straight line. However, due to the misalignment or other reasons, δx and δy may be not very small. In order to minimize the differences δx and δy, the detector plane of every SSD was tilted around x, y, and z dimensions. By changing the rotation angles iteratively, all the angles for the tilt correction were optimized. Corresponding values used for the tilt correction are tabulated in Table 3.3.

3.5 Position Resolution

Through the above-mentioned offset alignment and tilt correction, the whole SSD array was aligned. The relative position among SSDs, which is crucial for the vertex determination and the fragment correlation reconstruction, was also properly adjusted. Figure 3.14 illustrates the δx and δy distribution for the ^{31}Ar ions after the alignment. In both x and y directions, the projection of the δx - δy distribution yields a full width at half maximum (FWHM) of several tens of micrometers. The achieved tracking accuracy serves well for the present physics case.

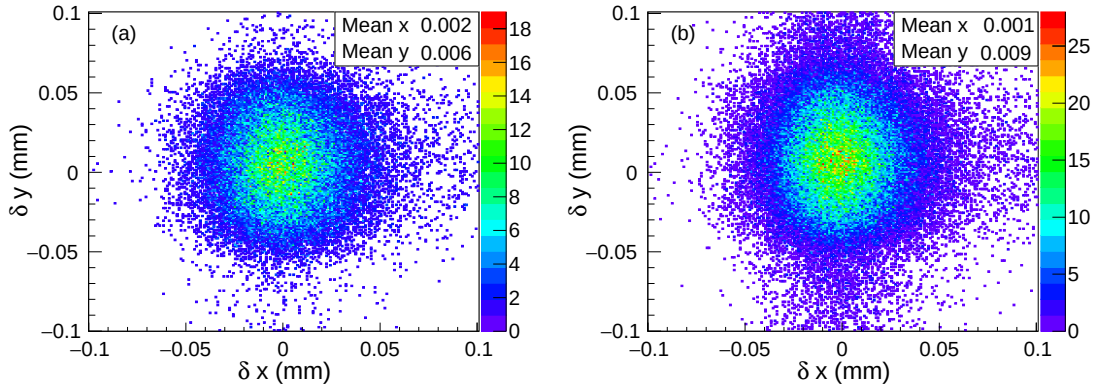

Figure 3.14: Position uncertainties (δx and δy) obtained for ^{31}Ar ions at the secondary target in the (x, y)-transverse directions. (a) δx and δy were evaluated from the differences between two alternative (x, y)-coordinate values of the ^{31}Ar positions at the target derived from two alternative ^{31}Ar trajectories defined by the SSD pairs SSD0 - SSD2 and SSD1 - SSD2, respectively. (b) Same as (a) but obtained from two alternative ^{31}Ar trajectories defined by the SSD pairs SSD0 - SSD3 and SSD1 - SSD3, respectively.

4 Tracking the Two-Proton Decay Products

The main goal of the present experiment is the production of hitherto unknown ^{30}Ar ions and the investigation of the ^{30}Ar states by tracking their 2*p*-decay products. In addition, the previously-known 2*p* radioactive nucleus ^{19}Mg [21] was also produced, and its 2*p* decay was remeasured for calibration purposes, e.g., determination of angular and half-life resolutions as well as the detection efficiency. Therefore, the offline analysis of the S388 experimental data includes two parts: the remeasurement of the 2*p* decay of ^{19}Mg and the investigation of the 2*p* decay of ^{30}Ar.

As shown in subsection 1.5.3, the identification of the short-lived 2*p* precursors (^{30}Ar or ^{19}Mg) can be realized by tracking its decay products, i.e., the HI daughter nucleus and the two protons. The measurement of trajectories of these decay fragments plays a key role in tracking of in-flight 2*p* decays. In the present work, the tracking procedure includes the following three steps:

- Identification of heavy ions at the final focal plane of the FRS.
- Identification of protons.
- Identification of the 2*p*-decay event by tracking the trajectories of all decay products in coincidence.

4.1 Identification of Heavy Ions

The heavy ions arriving at the final focal plane of the FRS F4 can be distinguished by their magnetic rigidity $B\rho$, time-of-flight (TOF), and energy deposition ΔE. Through such a $B\rho$-TOF-ΔE measurement, the mass-to-charge ratio (A/Q, Q is the ionic charge number) and proton number Z can be determined.

In the S388 experiment, the $B\rho$ of the ion was determined from the FRS magnet setting and the ion's position measured with TPCs. The TOF for the ion traveling from F2 to F4 was measured by using the scintillator SCI1 at F2 and scintillator SCI2 at F4. The ion's velocity v can be deduced from its TOF in the second half of the FRS by equation

$$v = \frac{S}{\mathrm{TOF} - T_0}, \tag{4.1}$$

where S is the flight path and T_0 is an offset corresponding to the time delay in cables and electronics. Once the v is obtained, the A/Q can be determined by using the following

equation

$$\frac{A}{Q} = \frac{B\rho e}{\beta\gamma cu}, \tag{4.2}$$

where e is the electron charge, c is the speed of light, u is the atomic mass unit, β is the ion's velocity in unit of the speed of light ($\beta = v/c$), γ is the Lorentz factor $\gamma = \sqrt{1-\beta^2}$.

Given the fact that the energy deposition ΔE of the HI in the MUSIC detector at F4 is nearly proportional to the square of the ion's charge Q, the Q can be calculated form the ΔE measured by the MUSIC. At the high energies used in the present experiment (several hundred MeV/u), most ions are fully stripped, so that we have a good approximation $Q = Z$. Therefore, the HI's proton number Z can be determined from ΔE measurements. By plotting the distribution of Z versus A/Q, the identification of HI can be achieved since each isotope has a unique combination of Z and A/Q.

4.2 Identification of Protons

4.2.1 Minimum Ionizing Particles Produced in Secondary Target

In order to track a 2*p*-decay event, both HI decay daughter and two protons are needed to be identified in coincidence. When a 2*p* precursor decays in-flight, its decay products including the protons and HI daughter nucleus are emitted. They can be detected by the SSDs which were located downstream of the secondary target. As shown in section 3.3, the HI normally deposits a large amount of energy and thus generates a strong signal in the SSD which can be easily identified. However, the identification of protons is a little bit tough due to the contamination of other minimum ionizing particles (MIPs), e.g., δ-electrons. When a charged particle, in particular a HI, impinges on the secondary target, its energy deposition could generate the MIPs. Since those MIPs may pass through the SSDs and generate similar signals as those created by protons, these MIPs pose a significant challenge to identify the protons. In order to avoid the wrong assignment of protons, the discrimination of protons from other MIPs is performed by a coincidence of signals from several SSDs.

4.2.2 Identification of Proton Candidates

The identification of the protons started with the search of the proton candidates registered by individual SSDs. Following the same procedure as that conducted for HI (see section 3.3.5 for detail), the proton candidates can be found by requiring the peak signal of a charged-particle hit exceeding a certain threshold and the signal of its neighboring strip exceeding another smaller threshold. Furthermore, the peak signal of a proton candidate is also required to be smaller than the threshold of a HI in order to rule out

the HI hit. The selected proton candidates could be either real protons or other MIPs. Since the background levels in S-side strips slightly differ from those in K-side strips, the thresholds employed to test the signals generated by the proton-candidate hits in the S-side are different from those used for the K-side. According to the knowledge gained from the previous experiment, most of protons trigger 1 or 2 strips [68]. Therefore, in the present data analysis, the maximum number of strips triggered by a proton-candidate hit is limited to be less than 3. Furthermore, keeping in mind that the electric noise may also exceed the thresholds, thus a random signal may be treated as a proton candidate, the total number of proton candidates allowed in one detector side is limited to be less than 13.

4.2.3 Discrimination of Protons from Other Minimum Ionizing Particles

After the identification of proton candidates, a so-called "straight-line" trajectory selection is applied to distinguish the real protons from other MIPs (e.g., δ-electrons) with the combination of several SSDs. Figure 4.1 schematically shows such a "straight-line" criterion. In this example, a proton candidate impinges on SSD0, SSD1, and SSD2 and introduces a hit in each SSD (hereafter hit0, hit1, and hit2 respectively). On the basis of three hit positions, the trajectory of the proton candidate can be reconstructed by connecting the hit0 and the hit2 (trajectory02), or by connecting the hit1 and the hit2 (trajectory12), or by connecting the hit0 and the hit1 (trajectory01). In the ideal case without scattering, the proton candidate will follow a "straight-line" trajectory during the passage through three detectors. In such a case the angle between the trajectory12 and the trajectory01 (i.e., θ shown in Figure 4.1) is zero. However, in reality, the θ is always non-zero due to the scattering in the SSDs and the uncertainty of position measurement. Given the fact that most MIP contaminants are lighter than the protons, thus they can be more easily deviated due to the multiple scattering when they pass through the SSD array. One can eliminate most of the contaminants by requiring a near "straight-line" trajectory, i.e., imposing a threshold on the θ. The proton candidate with the θ which is smaller than the threshold was regarded as a proton. In case that both HI and proton were found in the same event, the search of a 2*p* decay event can be performed. In the following, a tracking procedure of the 2*p* decay of ^{19}Mg is illustrated firstly. Then a search for the 2*p* decay of ^{30}Ar is described.

4.3 Tracking the 2*p* Decay of ^{19}Mg

In the present experiment, the previously-known 2*p* radioactive nucleus ^{19}Mg was produced by 1n knockout from the ^{20}Mg ion obtained by fragmenting a 685 MeV/u ^{36}Ar beam in a ^{9}Be target of thickness 4.8 $\mathrm{g/cm^2}$. Since the 2*p* decay of ^{19}Mg has been studied in the previous S271 experiment and the spectroscopic results on the several low-lying states of ^{19}Mg is known [21, 58, 68], for the calibration purpose, the in-flight

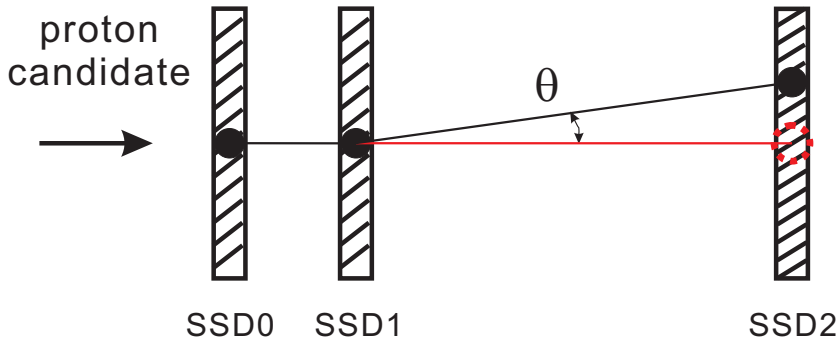

Figure 4.1: Schematic explanation of the "straight-line" criterion. Solid circles represent the hit positions of a proton candidate in the SSDs, while the round circle indicates the expected position in SSD2 which is obtained by straight-line extrapolation of the trajectory determined by proton candidate's hit positions in SSD0 and SSD1. The angle θ characterizes the deviation between the real trajectory of a proton candidate and the ideal straight-line trajectory. See text for details.

decays of ^{19}Mg were remeasured. During this reference measurement, the first half of the FRS was optimized to select and transport the secondary ^{20}Mg beam and the second half of the FRS was tuned to transmit the ^{17}Ne ions (hereafter ^{20}Mg-^{17}Ne setting). In order to identify the ^{19}Mg 2*p* decay events, the identification of decay daughter ^{17}Ne and two protons was performed by following the above-mentioned procedure and the ^{17}Ne+*p*+*p* coincidence was then searched.

4.3.1 Production and Identification of ^{17}Ne

The identification of heavy ions detected at F4 during the reference measurement with the ^{20}Mg-^{17}Ne setting was performed by employing the aforementioned $B\rho$-TOF-ΔE method. Corresponding results are shown in Figure 4.2. In this PID plot, each nuclide occupies a unique position according to its proton number Z and mass-to-charge ratio A/Q. Therefore, the heavy ion of interest can be identified unambiguously. In Figure 4.2, the ions of interest including ^{20}Mg and ^{17}Ne nuclei are emphasized by circles. Basically, the ^{17}Ne ions which reached F4 can be divided into two categories according to their production area. The first production area is the primary target region and the main production mechanism is the fragmentation of primary ^{36}Ar beam. These ^{17}Ne nuclei were transported from primary target area down to F4 and we name them the primary ^{17}Ne nuclei. The other production area is the secondary target area at F2. One may expect several reactions which may produce ^{17}Ne, such as the fragmentation of secondary ^{20}Mg beam and the 1n knockout of ^{20}Mg ion followed by the 2*p* decay of ^{19}Mg. We call those ^{17}Ne ions the secondary ^{17}Ne nuclei. The secondary ^{17}Ne nucleus is the ion of our interest since it may be created from the 2*p* decay of ^{19}Mg.

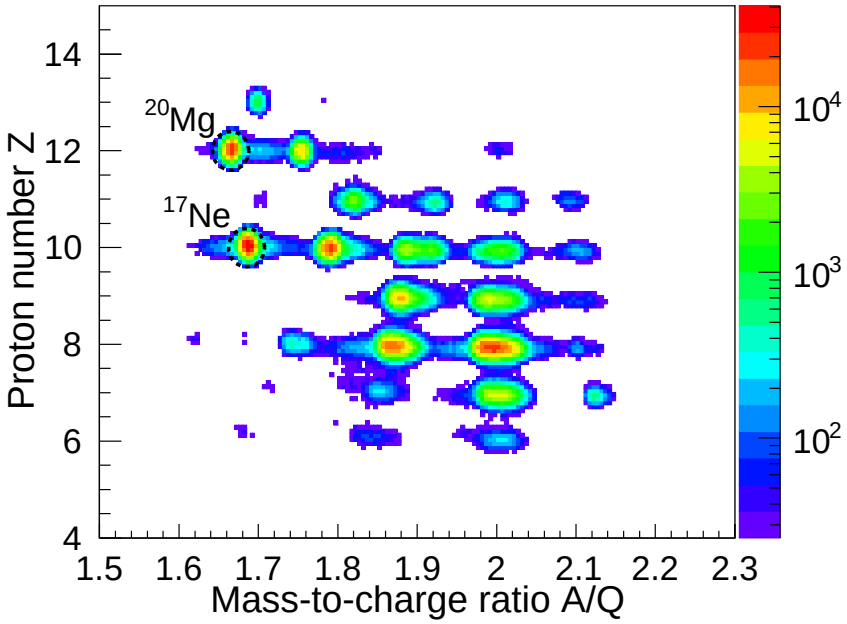

Figure 4.2: Two-dimensional cluster plot of Z vs A/Q for the heavy ions detected at F4 during the reference measurement with the ^{20}Mg-^{17}Ne setting. The first half of the FRS was optimized to transport the ^{20}Mg beam and the second half of the FRS was tuned to transmit the ^{17}Ne ions.

In the offline data analysis, some selections were performed to discriminate secondary ^{17}Ne nuclei from primary ^{17}Ne nuclei. Given the fact that the ^{20}Mg beam was selected as the secondary beam, thus ^{20}Mg ions were centered in the middle focal plane of the FRS F2. The primary ^{17}Ne nuclei had non-central profile. Two conditions were applied in the data analysis by means of the signals measured by detectors placed in F2 area. The first condition is the energy deposition of the HI in the TPC2 located in front of the secondary target should be within the range corresponding to the ^{20}Mg ions. Such a selection can rule out most of primary ^{17}Ne nuclei and ensure that the selected ^{17}Ne nuclei are related to the ^{20}Mg-induced reactions. The second condition was conducted to further select the secondary ^{17}Ne nuclei by requiring that the position of HI hit in the SSD0 and SSD1 should be at the center of the SSD. Since most of primary ^{17}Ne nuclei hit the non-center area of the SSD0 and SSD1, such a selection can further reduce the contaminant primary ^{17}Ne nuclei.

4.3.2 Identification of the 2*p* Decay of ^{19}Mg by Tracking Coincident $^{17}\mathrm{Ne} + p + p$ Trajectories

On the basis of the measured trajectory of a secondary ^{17}Ne nucleus and the trajectories of proton candidates, which fulfill the “straight-line” criterion, the minimum distance

between ^{17}Ne's trajectory and trajectory of proton candidate was calculated. Then the minimum distance was compared to a threshold. The proton candidates with the minimum distances smaller than the threshold were selected. The threshold value of 300 μm was determined by considering the accuracy of position measurement by SSDs and the requested experimental precision. As schematically shown in Figure 2.5, the vertex of a 2*p*-decay event is defined as the "meeting point" of the trajectories of two proton and the HI's trajectory. It is worth mentioning that the "meeting point" cannot be determined perfectly due to the experimental uncertainty. Therefore, in our data analysis, the "meeting point" of two trajectories was defined as the middle point of two points in the two respective trajectories where the distance between them is minimum. If the minimum distance between the trajectory of proton and HI' trajectory was smaller than the above-mentioned threshold, we assumed that proton and HI meet in one point. The corresponding "meeting point" was regarded as the vertex of $^{17}\mathrm{Ne} + p$ double coincidence. For a ^{19}Mg 2*p*-decay event, since there are two protons and one heavy ion recoil (^{17}Ne), thus two vertices from two $^{17}\mathrm{Ne} + p$ double coincidences can be reconstructed.

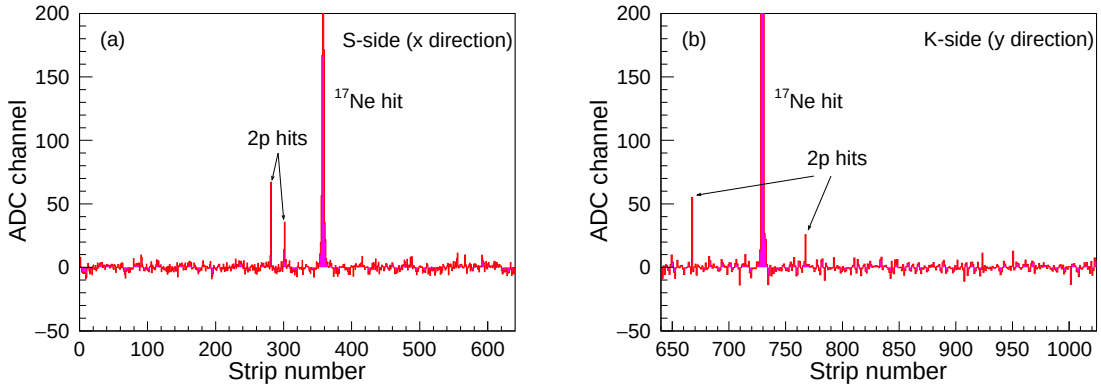

Figure 4.3: A ^{19}Mg 2*p* decay event registered by one SSD. The ^{17}Ne ion hit and two-proton hits are clearly identified in S-side (a) and K-side (b) of the SSD.

Based on the two vertices derived from two $^{17}\mathrm{Ne} + p$ double coincidences, one can further search for a triple $^{17}\mathrm{Ne} + p + p$ coincidence. To do so, the difference of two Z coordinates (Zdiff) of two decay vertices is calculated and Zdiff is required to be smaller than a threshold in order to indicate both protons and ^{17}Ne ion were produced in one decay event. The value for this criterion is adopted by studying the distribution of Zdiff and by taking into account the position measurement accuracy by SSDs. Once the above condition is fulfilled, one can be convinced that both two protons and the ^{17}Ne originate from a ^{19}Mg 2*p* decay event. Figure 4.3 shows a ^{19}Mg 2*p* decay event with the coincident hits of two protons and the ^{17}Ne ion in one SSD.

4.4 Tracking the 2*p* Decay of ^{30}Ar

A procedure similar as that explained in the previous section was employed to identify the 2*p* decays of previously-unknown nucleus ^{30}Ar. In this section, the identification of HI decay daughter ^{28}S will be illustrated firstly, then the search of the 2*p* decay of ^{30}Ar by tracking its decay products will be demonstrated.

4.4.1 Production and Identification of ^{28}S

In a similar manner to ^{17}Ne, the ^{28}S ions detected in the present experiment were divided into the primary ^{28}S nuclei and the secondary ^{28}S nuclei. The primary ^{28}S nuclei were produced via the fragmentation of primary ^{36}Ar beam in the primary target and the secondary ^{28}S nuclei were created by the ^{31}Ar-induced reactions in the secondary target, such as the direct fragmentation of ^{31}Ar and the one-neutron removal of ^{31}Ar followed by 2*p* decay of ^{30}Ar. Both primary and secondary ^{28}S nuclei may reach F4 area and they can be distinguished from other ion species by employing the previously-introduced $B\rho$-TOF-ΔE method. Figure 4.4 shows a two-dimensional PID plot for the ions reached F4. The ions of interest including ^{28}S and ^{31}Ar are well separated from other species and they are highlighted by the circles. Besides ^{28}S and ^{31}Ar, one may notice that other ion species with higher A/Q value (mainly in the surroundings of $N = Z$ nuclei) also reached F4 as seen in Figure 4.4. The origin of these ions is not very clear. Despite dedicated efforts to suppress these unexpected fragments during the experiment, however, many of them still reached F4. The explanation for this puzzle calls for future experimental studies and theoretical simulations. Nevertheless, these nuclei have no influence on the identification and selection of ^{28}S ions, because they can be identified unambiguously and thus can be excluded easily. In our data analysis, the ^{28}S nuclei were selected by a gate in the PID plot. The influence of other species were eliminated. In order to identify the secondary ^{28}S nuclei and to further identify the ^{30}Ar decay events, two conditions on the energy deposition in TPC2 of incoming ions were applied to the select ^{31}Ar ions in front of the secondary target. Just behind the secondary target, the position of the ^{28}S ions were also examined to gate the secondary ^{28}S nuclei.

4.4.2 Identification of Secondary ^{28}S Nuclei

In order to trace the source of ^{28}S nuclei, the incident ion species in front of the secondary target were investigated. Given the fact that the TPC can measure both ion's position and its energy deposition, the incoming ion species into the secondary target can be investigated by their energy deposition and positions measured by TPCs which were located in front of the secondary target. Such an inspection is necessary to identify the secondary ^{28}S nuclei, which originated from the ^{31}Ar-induced reactions in the secondary target.

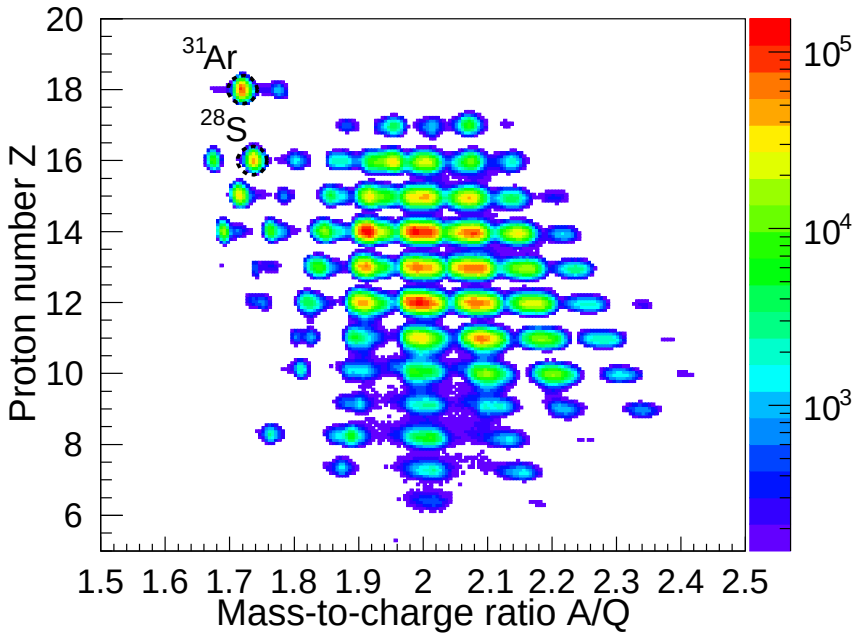

Figure 4.4: Two-dimensional cluster plot of Z vs A/Q for the heavy ions detected at F4 during the production measurements with the ^{31}Ar-^{28}S setting. The first half of the FRS was optimized to transport a 620 MeV/u ^{31}Ar beam and the second half of the FRS was tuned to transmit the ^{28}S ions.

As described in subsection 2.3.1, the ion-optical setting of the FRS in the present experiment was employed to transport the ^{31}Ar secondary beam by the first half of the FRS and to transmit ^{28}S ions from the secondary target down to F4 (hereafter ^{31}Ar-^{28}S setting). For the calibration purpose, another ion-optical setting was also applied in the experiment. In this setting, the ^{31}Ar fragments were selected by the first half of the FRS and the second half of the FRS was tuned to transport the ^{31}Ar ions down to last focal plane F4 (hereafter ^{31}Ar-^{31}Ar setting). Given the fact that the primary beam energy and the settings (e.g., Bρ) of the first half of the FRS are the same in both ion-optical settings, the energy deposition of ^{31}Ar ions in the TPC2 and their impact positions in the secondary target measured in the calibration measurement with the ^{31}Ar-^{31}Ar setting can be utilized to identify the incoming argon ions into the secondary target in the production measurements with the ^{31}Ar-^{28}S setting.

Figure 4.5(a) shows the energy deposition of ^{31}Ar and of ^{28}S ions in TPC2 versus their positions x in the secondary target. The ions' position in the secondary target were obtained by extrapolating the two hits in TPC1 and TPC2 located in front of the secondary target to the position in the secondary target. The data were obtained by gating the events with the ^{31}Ar or ^{28}S ion which reached F4 in the calibration measurement with

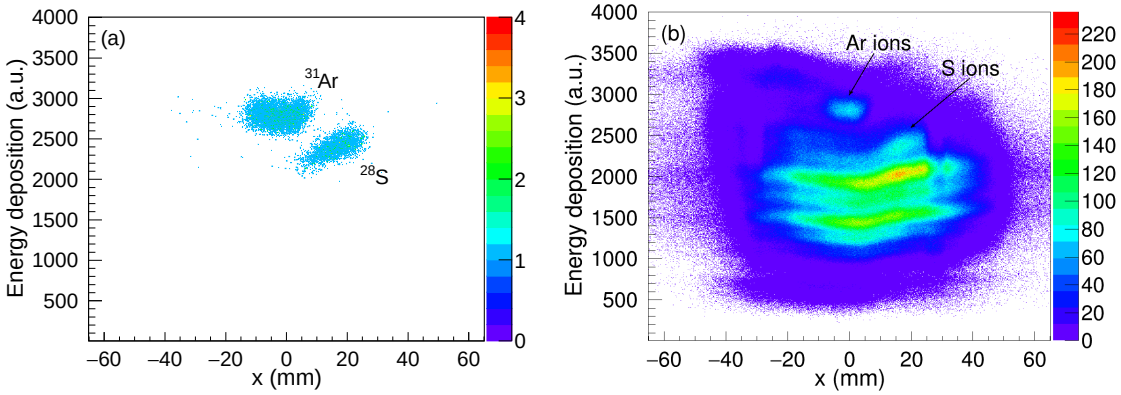

Figure 4.5: (a) The energy deposition of ^{31}Ar and of ^{28}S ions in TPC2 versus their positions x in the secondary target. Data is taken from the calibration measurement with the ^{31}Ar-^{31}Ar setting. (b) Same as (a) but for multiple ion species produced in the production measurements with the ^{31}Ar-^{28}S setting. The locations of argon ($Z = 18$) and the sulfur ($Z = 16$) isotopes are indicated. See text for details.

the ^{31}Ar-^{31}Ar setting. Based on the distribution, one can obtain the range of the energy deposition in TPC2 and the locations in the secondary target of ^{31}Ar ions and ^{28}S ions. Similar distribution for several kinds of ion species which were produced in the production measurements with the ^{31}Ar-^{28}S setting is displayed in Figure 4.5(b). In comparison of the panel (a) and the panel (b), it is clear that the ^{31}Ar ions produced in the production measurements with the ^{31}Ar-^{28}S setting are mainly within the area marked by "Ar ions". Since the ^{31}Ar fragments were selected as the centered beam and were transmitted by the first half of the FRS, one may naturally conclude that the ions in the area labeled with "Ar ions" in Figure 4.5(b) are mainly ^{31}Ar ions. It is possible that some other argon isotopes (e.g., ^{32}Ar) may be also transported to impinge on the secondary target. However, the intensity of ^{32}Ar is relatively small in comparison with ^{31}Ar. According to the LISE++ [117] simulation of the ions' transmission through the FRS with the ^{31}Ar-^{28}S setting, the intensity of ^{32}Ar at secondary target area is only about 3% of the intensity of ^{31}Ar. There is also noticeable difference between their locations at the secondary target of about 9 mm. In the experiment, the slits at F1 (opened of ± 14 mm) and F2 (opened of ± 15 mm) stopped most of ^{32}Ar ions. The small amount of ^{32}Ar ions may still reach the secondary target but become unresolvable with ^{31}Ar ions, because the distribution of ^{31}Ar ions' position x has a width (FWHM) of 12 mm, see Figure 4.5(a). LISE++ simulation shows the width of distribution of position x in secondary target for ^{31}Ar spot and for ^{32}Ar spot should be 6 mm and 7 mm, respectively. An assumed considerable admixture of ^{32}Ar and ^{31}Ar at F2 should result in a distribution of position x with the width of 16 mm. This is not the case in the experimental distribution of position x of Ar ions (see the blob indicated by "Ar ions" in Figure 4.5(b)). Therefore, one can conclude that Ar ions which impinged on the secondary target in the experiment are mainly ^{31}Ar

ions, and the very small admixture of ^{32}Ar ions can be neglected. In order to gate ^{31}Ar nucleus in front of the secondary target, which is helpful to identify the secondary ^{28}S nuclei behind the secondary target, two energy deposition thresholds were applied in order to define the range of incoming ions' energy deposition in the TPC2 during the analysis of the data taken from production measurements with the ^{31}Ar-^{28}S setting.

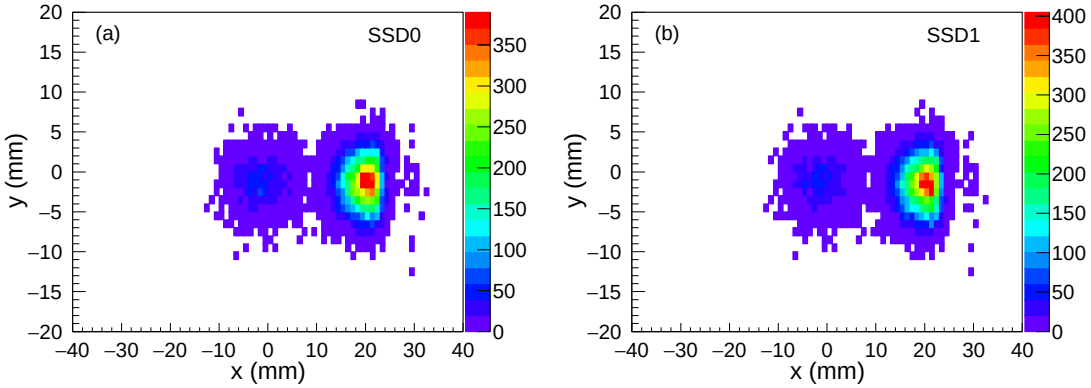

Figure 4.6: The positions of ^{28}S ions measured by the SSD0 (a) and SSD1 (b). Data is taken from the production measurements with the ^{31}Ar-^{28}S setting.

Besides the above-mentioned gate on the energy deposition of the incident ions in the TPC2, the position distributions of ^{28}S ions in the SSD0 and SSD1 were also examined. The purpose here is to discriminate further the secondary ^{28}S nuclei from primary ^{28}S ions according to their different hit positions on the first two SSDs. Figure 4.6(a) and Figure 4.6(b) show the positions of ^{28}S ions measured by SSD0 and SSD1, respectively. One can clearly see the ^{28}S ions are distributed in two distinct clusters. According to the ^{28}S's position indicated in Figure 4.5(a), most of primary ^{28}S nuclei's positions in the secondary target are off-center. Given the fact that the SSD0 and SSD1 were placed just behind the secondary target and the centers of these two detectors as well as the center of the secondary target were aligned along the beam axis, the position cluster which is off the center of the SSD0 and SSD1 should be produced by the primary ^{28}S nuclei. Concerning the cluster which is located at center of the SSD0 (or SSD1), presumably it was produced by the secondary ^{28}S nuclei since the ^{31}Ar ions were selected as the centered beam to impinge on the secondary target and the secondary ^{28}S nuclei were produced by the ^{31}Ar-induced reactions. In order to select the ion with position in the central cluster, two conditions on the x coordinates of the ^{28}S ions measured by the SSD0 and the SSD1 were applied. Such a selection effectively reduced the primary ^{28}S contaminants. As explained in subsection 4.4.1, the secondary ^{28}S nuclei may be produced by several kinds of ^{31}Ar-induced reactions. In order to identify those ^{28}S ions which were produced by the $2p$ decays of ^{30}Ar, after above-introduced selections, the secondary ^{28}S nuclei were further tested by searching the $^{28}\mathrm{S}+p+p$ coincidences. The

procedure is described in the following subsection.

4.4.3 Identification of the 2*p* Decay of ^{30}Ar by Tracking Coincident $^{28}\mathrm{S} + p + p$ Trajectories

Once the secondary ^{28}S nucleus was identified in one event, the proton candidates were found by performing the procedure described in section 4.2. Afterwards, several conditions and thresholds were applied to identify the ^{28}S + p + p coincidence. Such a procedure is similar as that employed for the identification of ^{19}Mg decay events. The selection procedure can be divided into three steps. First, the trajectories of proton candidates and that of ^{28}S were reconstructed by using the coordinates measured by SSDs. Second, the "meeting point" between proton candidates's trajectory and ^{28}S's trajectory was measured and then the "meeting point" was tested by a threshold in order to check whether it is a vertex for a ^{28}S + p double coincidence. Third, the difference between the Z coordinates of two vertices (i.e., Zdiff) derived from two ^{28}S + p double coincidences was calculated and the Zdiff was tested by another threshold to identify the $^{28}\mathrm{S} + p + p$ triple coincidence. If a triple coincidence $^{28}\mathrm{S} + p + p$ was identified, an ^{30}Ar 2p decay event was found. In comparison with the identification of the ^{19}Mg 2p decay events, it is worth mentioning that different value of thresholds (or conditions) were adopted to search the ^{30}Ar 2p decay events because the experimental conditions (e.g, energy of primary beam) employed to produce the ^{30}Ar were different from those used to create the ^{19}Mg. Figure 4.7 displays one ^{30}Ar 2p decay event. The hit of daughter nucleus ^{28}S and two-proton hits are clearly seen.

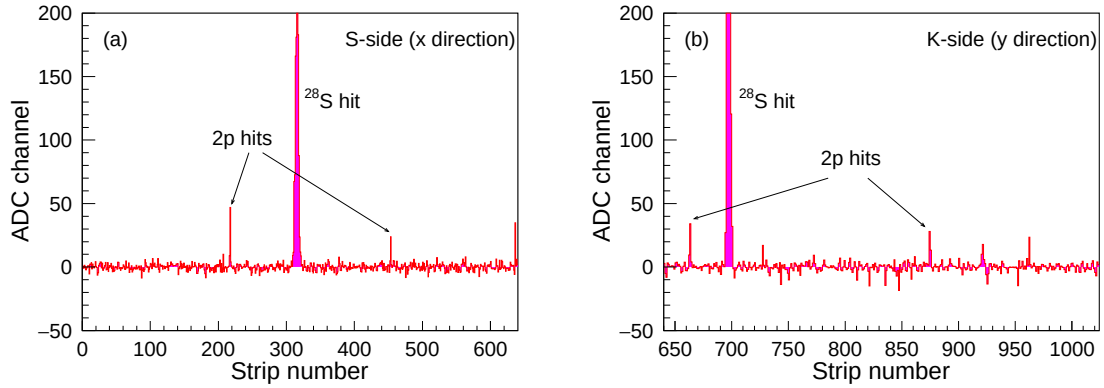

Figure 4.7: An ^{30}Ar 2p decay event registered by one SSD. The ^{28}S hit and two-proton hits are clearly identified on S-side (a) and K-side (b) of the SSD.

In the present work, all events related to the 2p decay of ^{30}Ar were identified by the above introduced procedure. Based on the measured coincident $^{28}\mathrm{S} + p + p$ trajectories, the 2p decay vertex of ^{30}Ar was determined. The position of vertex allows us to find where the decay happened and thus provides information on the location of parent nu-

cleus. Figure 4.8 shows the distribution of vertex's coordinates in the transverse plane (i.e., (x, y) plane) for all identified $^{28}\mathrm{S}+p+p$ coincidences. It can be clearly seen that the distribution is centered around $(x, y) = (0, 0)$, which matches the location of secondary ^{28}S nuclei (the central clusters in Figure 4.6) and ^{31}Ar's location in the secondary target (see Figure 4.5(b)). This demonstrates that $^{28}\mathrm{S}+p+p$ coincidences originated from the ^{31}Ar-induced reactions.

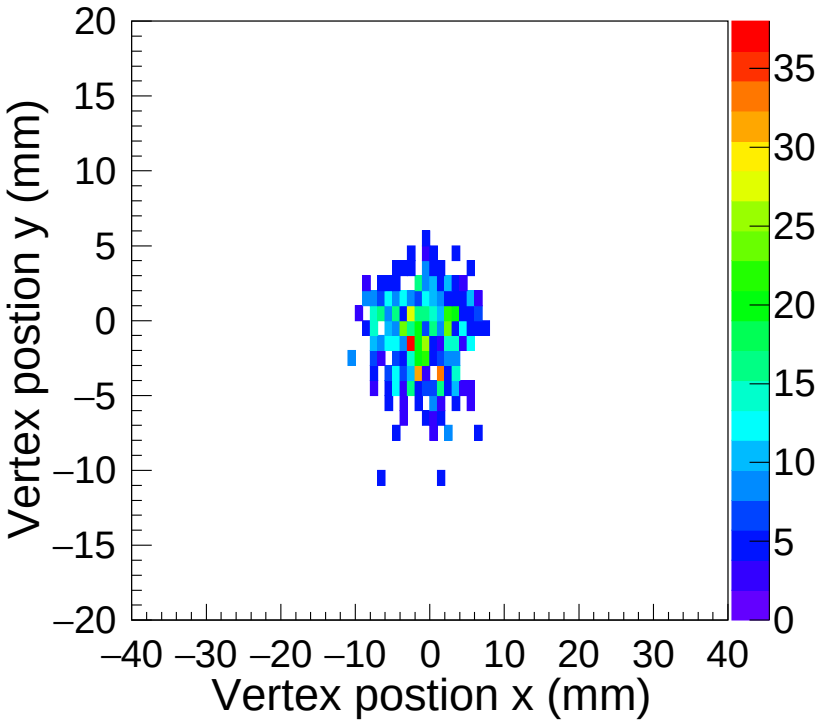

Figure 4.8: Distribution of vertex's coordinate x and y for measured $^{28}\mathrm{S}+p+p$ coincidences.

5 Spectroscopic Results of ^{19}Mg Deduced from ^{17}Ne-Proton Angular Correlations

In the previous chapter, the identification of 2*p* decay of ^{19}Mg and ^{30}Ar is demonstrated. In this chapter and the next chapter, the nuclear structure information on the observed states in ^{19}Mg and ^{30}Ar deduced from the HI-proton angular correlations will be presented.

Given the fact that the angular correlations reflect the transverse momentum correlations, which are often employed to identify nuclear states and to pin down the decay channels [68, 95], the measured angular correlations of protons with respect to the 2*p*-decay daughter nucleus provide insight into the structure of the 2*p* precursor's state. Therefore, the angular HI-proton correlations can be utilized to identify the states of mother nuclei and to deduce their decay properties (e.g., decay energy and width). As mentioned in subsection 1.5.3, this method has been successfully applied in previous investigations on ^{19}Mg and ^{16}Ne [18, 58, 68]. In the same manner, the angles between 2*p*-decay products of ^{19}Mg and ^{30}Ar were measured and the HI-proton angular correlations were reconstructed in the present work. By analyzing the ^{17}Ne-proton angular correlations deduced from the ^{19}Mg decay events, the spectroscopic information about ^{19}Mg states are obtained, which are presented in this chapter. In the next two chapters, we will turn to study the ^{28}S-proton angular correlations stemming from decays of the unknown nucleus ^{30}Ar. It is worth mentioning that throughout this chapter the energy of states in ^{19}Mg and ^{18}Na are given relative to the respective ^{17}Ne+*p*+*p* and ^{17}Ne+*p* thresholds.

5.1 ^{17}Ne-Proton Angular Correlations in 2*p* Decay of ^{19}Mg

Based on the measured trajectories of ^{17}Ne and two protons which were emitted by the 2*p* decay of ^{19}Mg, the angle between ^{17}Ne's track and proton's track ($\theta_{^{17}\mathrm{Ne\text{-}p}}$) as well as the angle between both protons' trajectories ($\theta_{p\text{-}p}$) are obtained. Corresponding ^{17}Ne-*p* angular correlations were reconstructed for all $^{17}\mathrm{Ne} + p + p$ coincidences. Figure 5.1(a) shows the scatter plot ($\theta_{^{17}\mathrm{Ne\text{-}p1}}$, $\theta_{^{17}\mathrm{Ne\text{-}p2}}$) for the measured angles between ^{17}Ne and both protons. Since both protons cannot be distinguished, the distribution is symmetrized with respect to proton permutations, and proton indexes are given for illustration purpose only. In this angular correlation plot, there are several statistical enhancements which provide the information on the 2*p* states in ^{19}Mg and 1*p* resonances in ^{18}Na. Among the most intense 2*p*-decay channels, events with the smallest $\theta_{^{17}\mathrm{Ne\text{-}p}}$ angles fall

into a distinct cluster centered around $\theta_{^{17}\text{Ne-p}} = 27$ mrad. According to the knowledge on the known states of ^{19}Mg obtained from previous experimental studies [21,58], these events are attributed to the simultaneous $2p$ decay from the g.s. of ^{19}Mg.

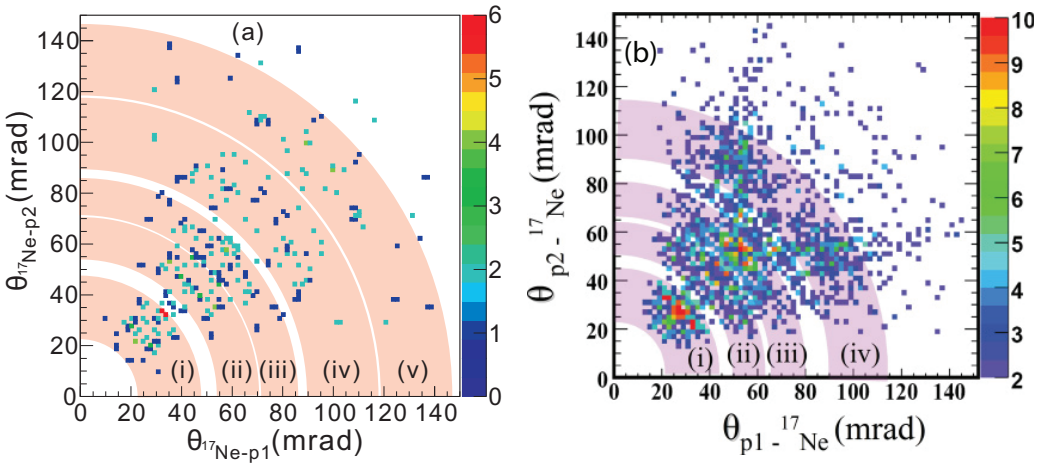

Figure 5.1: ^{17}Ne-proton angular correlations derived from $^{17}\text{Ne} + p + p$ coincidences measured in the present experiment (panel (a)) and in the previous experiment [58] (panel (b)). The arcs labeled by Roman numerals indicate several states of ^{19}Mg.

By comparing the ^{17}Ne-proton angular correlations measured in the present experiment (see Figure 5.1(a)) with that obtained in previous S271 experiment (see Figure 5.1(b)), one can clearly observe that the statistics obtained in the present experiment is much less than previous data. Nevertheless, the measured ^{17}Ne-p angular correlations indicate that several low-lying states of ^{19}Mg observed in previous experiment were also detected in the present experiment, which include the g.s. (labeled with (i)) and several previously-known excited states (labeled with (ii), (iii), and (iv)). Besides the known states, the present data also provide hints on an unknown excited state of ^{19}Mg which is labeled by (v). Such a comparison proves that the tracking method works well even with the limited statistics and the experimental resolution obtained in the present experiment serves well for our purposes.

The decay mechanism of the observed ^{19}Mg states can be pinned down by analyzing the measured ^{17}Ne-p angular correlations. As sketched by Figure 5.2, three $2p$-decay mechanisms are normally considered, i.e., simultaneous three-body decay, sequential emission of protons via a narrow intermediate state in the intermediate nucleus, and de-excitation of broad continuum parent states by $2p$ emission with final-state interactions. Depending on the particular decay mechanism, corresponding angular correlation pattern between HI daughter nucleus and proton shows a characteristic shape. In the simultaneous $2p$ decay case, the energies of both emitted protons should preferentially be

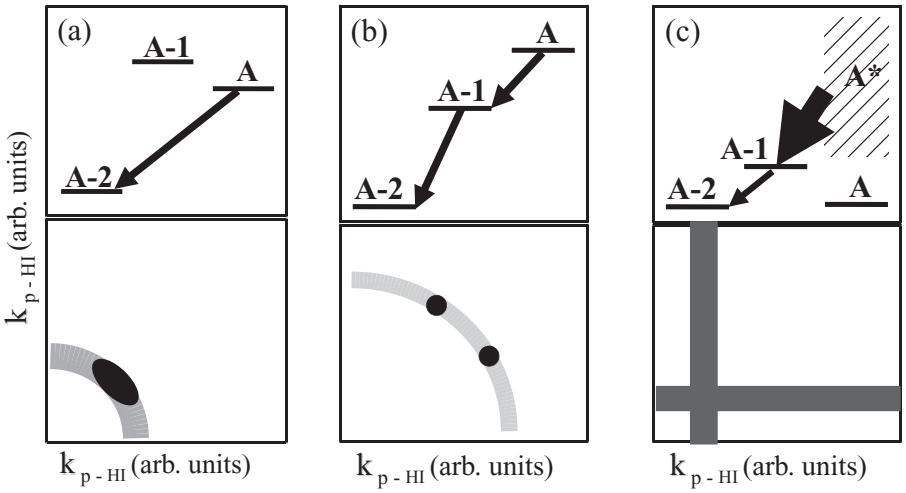

Figure 5.2: Schematic drawings of transverse momentum (lower panels) correlations expected for different cases of 2*p* emission (upper panels). The decay of the parent nucleus with mass number A to the daughter nucleus with mass number $A-2$ proceeds via three decay mechanisms: (a) true three-body decay, (b) sequential emission of protons via a narrow intermediate state in nucleus with mass number $A-1$, and (c) decay of broad continuum states. Figure taken from [68].

equal [6, 82]. The angular correlation between HI and proton is located along a quadrant, whose radius reflects the Q_{2p} value. Most of the events are in the peak indicated by the dark spot in the lower panel of Figure 5.2(a). In the case of sequential emission of two protons via a narrow resonance in the intermediate nucleus, the angular HI-proton correlation plot should yield double peaks [118] as indicated by the black dots in the lower panel of Figure 5.2(b). In the case of the 2*p* emission from broad continuum parent states with final-state interactions in the HI-*p* pairs, the angular HI-*p* correlation pattern should be featured by broad distributions along narrow "slices" as shown in the lower panel of Figure 5.2(c). Ideally, one may expect that the 2*p* precursor of interest may decay by following one of the above three mechanisms. However, in reality several proton branches may appear resulting in complicated spectra with several statistical enhancements in the angular HI-*p* correlations. This can be seen in Figure 5.1(a).

In order to better reveal the decay properties from the measured ^{17}Ne-proton angular correlations shown in Figure 5.1(a), one may use the fact that the two protons emitted by one state of ^{19}Mg share the same total decay energy thus $\theta_{^{17}\mathrm{Ne\text{-}p}}$ correlations from 2*p* decays of the same narrow state are accumulated along the arc with the radius

$$\rho_\theta(^{17}\mathrm{Ne} + \mathrm{p} + \mathrm{p}) = \sqrt{\theta^2_{^{17}\mathrm{Ne\text{-}p1}} + \theta^2_{^{17}\mathrm{Ne\text{-}p2}}} = \mathrm{const.}$$

Since ρ_θ is related to the energy sum of both emitted protons and therefore to the Q_{2p}

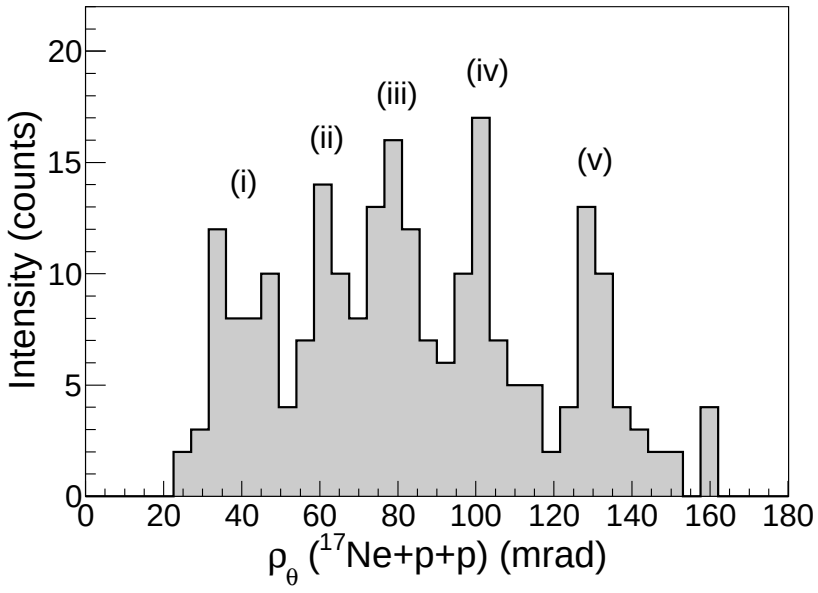

Figure 5.3: The ρ_θ spectrum measured for ^{19}Mg 2*p* decays. The peak in this figure and the arc in Figure 5.1(a) labeled with the same Roman numeral are one-to-one correspondence. See text for details.

of the parent state by the relation $Q_{2p} \sim \rho_\theta^2$ [58], one can obtain the indication of the parent state and its 2*p*-decay energy by studying the distribution of ρ_θ. The ρ_θ spectrum always has fewer peaks which allow us to select specific excitation-energy regions for the investigation.

In the present study, the ρ_θ distribution measured for ^{19}Mg 2*p* decays is displayed in Figure 5.3. Several well-separated intense peaks, which indicate the 2*p* decays of various states in ^{19}Mg, are clearly seen and labeled by Roman numerals. Correspondingly, Figure 5.1(a) are ^{17}Ne-*p* angular correlations from the decays of these states in ^{19}Mg. The peak in Figure 5.3 and the arc in Figure 5.1(a) labeled with the same Roman numeral consist of the same events. By gating on a particular ρ_θ peak, the decay events from a certain ^{19}Mg state can be selected. In the following, the observed states of ^{19}Mg will be investigated by interpreting corresponding ^{17}Ne-*p* angular correlations in terms of the Monte Carlo simulations.

5.2 Monte Carlo Simulations of the Detector Response to the 2*p* Decay of ^{19}Mg

In order to simulate the conversion from momentum to angular correlations in 2*p* decay and to deduce decay properties of the observed nuclear states form the measured

^{17}Ne-p angular correlations, the detailed Monte Carlo (MC) simulations of the detector response to the 2p decay of ^{19}Mg were performed by using the GEANT framework [119]. The GEANT package includes relativistic kinematics and all important processes of interaction between relativistic particles and various materials. Furthermore, the incoming-beam characteristics, detector resolutions, and reaction kinematics were also taken into account in the simulations.

In our simulations, the state of ^{19}Mg was assumed to have a resonance energy Q_{2p} and a finite lifetime. Two decay mechanisms were considered. The first one is the simultaneous 2p-decay of the ^{19}Mg g.s. To simulate such a three-body decay process, the momenta of three decay products are needed, and they were provided by the three-body model calculations [32, 64, 92]. Another decay mechanism is the sequential emission of protons from ^{19}Mg e.s. via intermediate states of ^{18}Na. Other physics input is the kinetic energy of ^{19}Mg ion impinging on the target, which was estimated by using the LISE++ simulation of the FRS magnetic spectrometer under the ^{20}Mg-^{17}Ne setting. Concerning the secondary reaction target and detectors in the MC simulations, their material and geometry were implemented by using the same parameters as the secondary target and SSDs employed in the real experiment. In general, the MC simulations started at a randomly chosen $^{17}\mathrm{Ne}+p+p$ vertex inside the reaction target and followed by the passage of protons and ^{17}Ne through the remainder of the reaction target and the detectors. The angular straggling, detection efficiency, and the experimental uncertainties in position determination, vertex reconstruction, and angle measurement, etc. were taken into account. During the simulations, all selection conditions and thresholds applied in the data analysis were used in the same way, which allowed the results of the MC simulations to be treated identically to the experimental data.

5.2.1 2p Radioactivity of the ^{19}Mg Ground State

In order to quantitatively interpret the ^{17}Ne-p angular correlations indicated by the arc (i) in Figure 5.1(a) and the peak (i) in 5.3, MC simulations of the detector response to the simultaneous 2p decay of the ^{19}Mg g.s. were performed by assuming various values of Q_{2p}. Then each simulated $\theta_{^{17}\mathrm{Ne\text{-}p}}$ spectrum was compared with the experimental $\theta_{^{17}\mathrm{Ne\text{-}p}}$ distribution obtained by selecting events in the arc-gate (i) of Figure 5.1(a), i.e., $22.5 < \rho_\theta < 47.0$ mrad. Such a comparison is shown in Figure 5.4(a), in which the angular $\theta_{^{17}\mathrm{Ne\text{-}p}}$ correlations obtained from the simulation of ^{19}Mg g.s. decay with $Q_{2p} = 0.87$ MeV is compared with the experimental $\theta_{^{17}\mathrm{Ne\text{-}p}}$ distribution selected by using the arc-gate (i). One can see the quantitative agreement between the simulation and the data. In order to evaluate the compatibility in shape between simulation and data, the probability that the simulated $\theta_{^{17}\mathrm{Ne\text{-}p}}$ distribution matches the experimental pattern was calculated by using a standard statistical Kolmogorov-Smirnov test [120]. The stars in Figure 5.4(b) show such probability as a function of Q_{2p}, while the solid

curve is the fit of the probability distribution by a skewed Gaussian function. Based on the fitting function, the optimal decay energy which corresponds to the highest probability is $Q_{2p} = 0.87$ MeV. The Q_{2p} range where the simulation can reproduce the data with probabilities above 50% is accepted as the uncertainty of the fitted value. Thus the 2*p*-decay of ^{19}Mg g.s. derived from the present work is $Q_{2p} = 0.87^{+0.24}_{-0.07}$ MeV, which is consistent with previous data: 0.76(6) MeV [58]. Therefore, the data from the present experiment have confirmed the simultaneous 2*p* decay of ^{19}Mg g.s. In comparison with previous data, one may notice that Q_{2p} of ^{19}Mg g.s. obtained by the present work carries larger uncertainty, which can be understood by two reasons. First, the thick target ($\sim$2.66 cm) used in the present experiment leads to stronger multiple scattering, and thus larger angular straggling inside the target. Second, since the ^{19}Mg is treated as the reference nucleus, a relatively short measurement time was granted for the investigation of the 2*p* decay of ^{19}Mg. Therefore, only a small amount of decay events was identified in the present experiment, which causes a large statistical error.

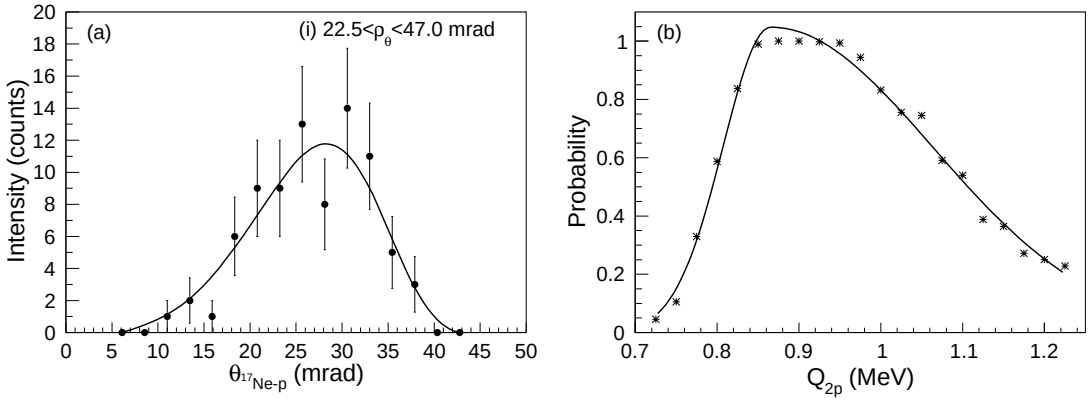

Figure 5.4: (a) Measured ^{17}Ne-*p* angular correlations (full circles with statistical errors) derived from the $^{17}\mathrm{Ne} + p + p$ coincidences with the gate $22.5 < \rho_\theta < 47.0$ mrad, which corresponds to the peak (i) in Figure 5.3 and arc (i) in Figure 5.1(a). The solid curve represents the $\theta_{^{17}\mathrm{Ne\text{-}p}}$ distribution obtained from the MC simulation of the detector response to the direct 2*p* decay of ^{19}Mg g.s. with $Q_{2p} = 0.87$ MeV. (b) Distribution of probability that simulation reproduces the data of Figure 5.4(a) as a function of Q_{2p}. The curve displays the fit to the probability distribution by a skewed Gaussian function.

5.2.2 2*p* Decay of the Known ^{19}Mg Excited States

Concerning the peaks and arcs (ii), (iii), and (iv), one may expect that they originate from 2*p* decays of several previously-known low-lying excited states of ^{19}Mg since the positions and ranges of these arcs almost coincide with the respective arcs displayed in Figure 5.1(b). In order to verify our guess and interpret these states in a quantitative way, the MC simulations were performed and then compared with the experimental data.

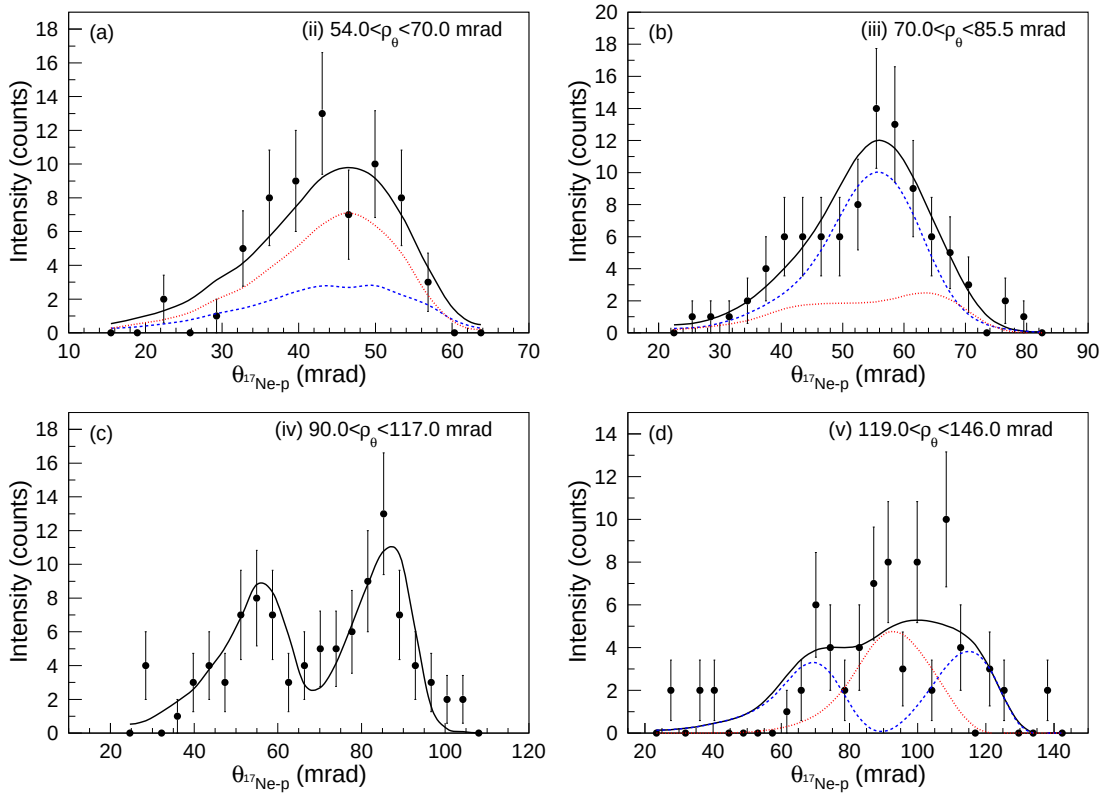

Figure 5.5: Same as Figure 5.4(a) but for the excited states of ^{19}Mg. (a) The 2*p* decay of e.s. gated by (ii), $54.0 < \rho_\theta < 70.0$ mrad. The solid curve displays the simulation of the sequential 2*p* decay of ^{19}Mg state at 2.5 MeV via ^{18}Na states at 1.23 MeV (dotted curve) and 1.55 MeV (dashed curve). (b) The 2*p* decays gated by (iii), $70.0 < \rho_\theta < 85.5$ mrad. The solid curve is the simulation of the sequential 2*p* decay of ^{19}Mg state at 3.2 MeV via the 1.55 MeV (dashed curve) and 2.084 MeV (dotted curve) levels in ^{18}Na. (c) The 2*p* decays gated by (iv), $90.0 < \rho_\theta < 117.0$ mrad. The result of the simulation to the sequential 2*p* emission of ^{19}Mg state at 5.1 MeV via 1.55 MeV state of ^{18}Na state is depicted by the solid curve. (d) The 2*p* decay of a new e.s. in ^{19}Mg gated by (v), $119.0 < \rho_\theta < 146.0$ mrad. The dashed curve and dotted curve are the $\theta_{^{17}\text{Ne-p}}$ distributions obtained by simulations of sequential proton emission of ^{19}Mg state at 8.9 MeV via two unknown observed ^{18}Na states at 2.5 MeV and 4.0 MeV, respectively. The solid curve shows the sum fit.

In Figure 5.5(a), the $\theta_{^{17}\text{Ne-p}}$ correlation obtained by imposing the arc gate (ii), $54.0 < \rho_\theta < 70.0$ mrad is shown by black dots with statistical errors. Corresponding peak (ii) in the ρ_θ spectrum (see Figure 5.3) illustrates the 2*p* decays from a single state in ^{19}Mg. To interpret the observed ^{17}Ne-*p* angular correlations deduced from this state, the MC simulation was performed by assuming a sequential decay mechanism: $^{19}\text{Mg}^* \rightarrow$

$^{18}\mathrm{Na}^{*} + p \rightarrow {}^{17}\mathrm{Ne} + p + p$. The input parameters concerning the ^{19}Mg state are the 2*p*-decay energy $Q_{2p} = 2.5$ MeV and the width $\Gamma = 0.4$ MeV. The parameters regarding two ^{18}Na states are 1*p*-decay energies $Q_{1p}(1^{-}) = 1.23$ MeV and $Q_{1p}(2^{-}) = 1.55$ MeV, respectively. The simulated $\theta_{^{17}\mathrm{Ne\text{-}p}}$ distribution is displayed by the solid curve in Figure 5.5(a). The simulation reproduces the data very well. Therefore, the results obtained from the present experiment confirm the sequential 2*p* emission of the previously known ^{19}Mg $3/2^{-}$ state. The newly determined $Q_{2p} = 2.5^{+0.8}_{-0.4}$ MeV is in agreement with previous data 2.14(23) MeV.

In the same manner, we performed MC simulations in order to quantitatively study the events in the arc (iii) in Figure 5.1(a) and peak (iii) in Figure 5.3. The experimental $\theta_{^{17}\mathrm{Ne\text{-}p}}$ distribution selected from 2*p* decay events with the condition of $70.0 < \rho_{\theta} < 85.5$ mrad is plotted in Figure 5.5(b). The simulations of the detector response to the sequential 2*p* emission of the ^{19}Mg e.s. via two intermediate states in ^{18}Na were performed. The input parameter concerning the ^{19}Mg state is $Q_{2p} = 3.2$ MeV. The resonance energy for two states of ^{18}Na are 1.55 MeV and 2.084 MeV respectively. The branching ratios for the two above-mentioned decay branches are 75% and 25%, respectively. The simulated $\theta_{^{17}\mathrm{Ne\text{-}p}}$ distribution is displayed by the solid curve in Figure 5.5(b). One can clearly see that it generally reproduces the experimental spectrum. The simulation shows a smoother distribution than the experimental pattern which can be attributed to much larger statistics of the simulated events than of experimental data. The determined Q_{2p} for broad peak (iii) is $3.2^{+1.2}_{-1.0}$ MeV, which matches the previously-measured ^{19}Mg excited states at 2.9(2) and 3.6(2) MeV [58]. However, these two states cannot be resolved in the present experiment due to the limited experimental resolution and the small statistics.

Regarding the ^{19}Mg e.s. shown by the arc (iv) in Figure 5.1(a) and peak (iv) in Figure 5.3, the experimental $\theta_{^{17}\mathrm{Ne\text{-}p}}$ distribution is obtained by gating the events with ρ_{θ} ranging from 90.0 to 117.0 mrad and displayed by the black dots in Figure 5.5(c). Comparing the $\theta_{^{17}\mathrm{Ne\text{-}p}}$ distribution with that obtained in the previous experiment [58], it is reasonable to assume that the events within peak (iv) and arc (iv) belong to the 2*p* decays of third $3/2^{-}$ state in ^{19}Mg. To test our assumption, MC simulation of the detector response to the sequential 2*p* emission of ^{19}Mg e.s. with a $Q_{2p} = 5.1^{+0.3}_{-0.3}$ MeV via the 1.55 MeV ^{18}Na resonance was performed. The obtained $\theta_{^{17}\mathrm{Ne\text{-}p}}$ distribution is shown by the solid curve in Figure 5.5(c). One can see that the simulated spectrum and experimental distribution match in general. Therefore, the present work confirms the conclusion drawn in the previous study [58] that the 5.5(2) MeV e.s. of ^{19}Mg decays by sequential emission of protons via the 1.55 MeV ^{18}Na state.

5.2.3 Hints of One New State in ^{19}Mg and Two New States in ^{18}Na

In Figure 5.3, besides the known excited states of ^{19}Mg shown by the peaks (ii), (iii), and (iv), evidence on a new e.s. of ^{19}Mg is displayed by the peak (v) which is located around $\rho_\theta = 130$ mrad. Corresponding $\theta_{^{17}\text{Ne-p1}}$ versus $\theta_{^{17}\text{Ne-p2}}$ distribution is shown by the arc (v) in Figure 5.1(a). One can see that most events fall into several clusters which indicate sequential emission of protons from one e.s. of ^{19}Mg via intermediate resonances of ^{18}Na. The angular $\theta_{^{17}\text{Ne-p}}$ spectrum obtained by imposing the arc gate (v) ($119.0 < \rho_\theta < 146.0$ mrad) is shown by the black dots in Figure 5.5(d). It is found that such a multiple peak structure cannot be described by a sequential 2*p* decay via any previously-known ^{18}Na state because the characteristic $\theta_{^{17}\text{Ne-p}}$ pattern generated from 1*p* decay of the known state in ^{18}Na doesn't fit any peak shown in Figure 5.5(d). In order to interpret such experimental $\theta_{^{17}\text{Ne-p}}$ spectrum, the existence of two new ^{18}Na levels has to be assumed.

The hints of two new states expected for ^{18}Na can be found in Figure 5.6 which displays the comparison of angular $\theta_{^{17}\text{Ne-p}}$ correlations obtained from the measured $^{17}\text{Ne}+p$ and $^{17}\text{Ne}+p+p$ coincidences in the present experiment. In the former case, parent ^{18}Na states may be populated via several possible reactions on ^{20}Mg, while the latter distribution is presumably due to the 2*p* emission from ^{19}Mg states. Five peaks (1-5) which coexist in both histograms suggest the states of ^{18}Na. According to existing knowledge on the angular correlations obtained from the decays of known ^{18}Na states [58], the peaks 1-3 correspond to the the ^{18}Na states at 1.23 MeV, 1.55 MeV, and 2.084 MeV, respectively. Concerning the peak 4 and 5, they provide indications of two unknown e.s. in ^{18}Na, which are located at 2.5 MeV and 4.0 MeV above the 1*p* threshold, respectively.

Two above-discussed new states in ^{18}Na provide a possible explanation for the observed $\theta_{^{17}\text{Ne-p}}$ distribution shown in Figure 5.5(d), i.e., such an ^{17}Ne-proton angular correlations may originate from the decays of a new e.s. in ^{19}Mg by sequential emission of protons via the above-mentioned two ^{18}Na e.s. To verify such a tentative assignment, several MC simulations were performed. By properly varying the decay energies and lifetimes of ^{19}Mg state and ^{18}Na levels, it was found that the simulation of sequential emission of protons from ^{19}Mg e.s. at $8.9^{+0.8}_{-0.7}$ MeV via the excited states of ^{18}Na at $2.5^{+0.7}_{-0.3}$ MeV and $4.0^{+1.5}_{-0.6}$ MeV could reproduce the data tentatively. Corresponding two components are displayed by the dashed and dotted curves in Figure 5.5(d), respectively. The sum fit is illustrated by the solid curve, and it generally agrees with the data. In particular, the multiple-peak structure of the experimental pattern is reasonably described. It is worth noting that the energy level of ^{18}Na around 2.5 MeV has been predicted in a theoretical work [77]. Given the fact that the limited amount of ^{19}Mg 2*p* decay events identified in the present experiment, which provides only the hints of a new ^{19}Mg e.s. and two

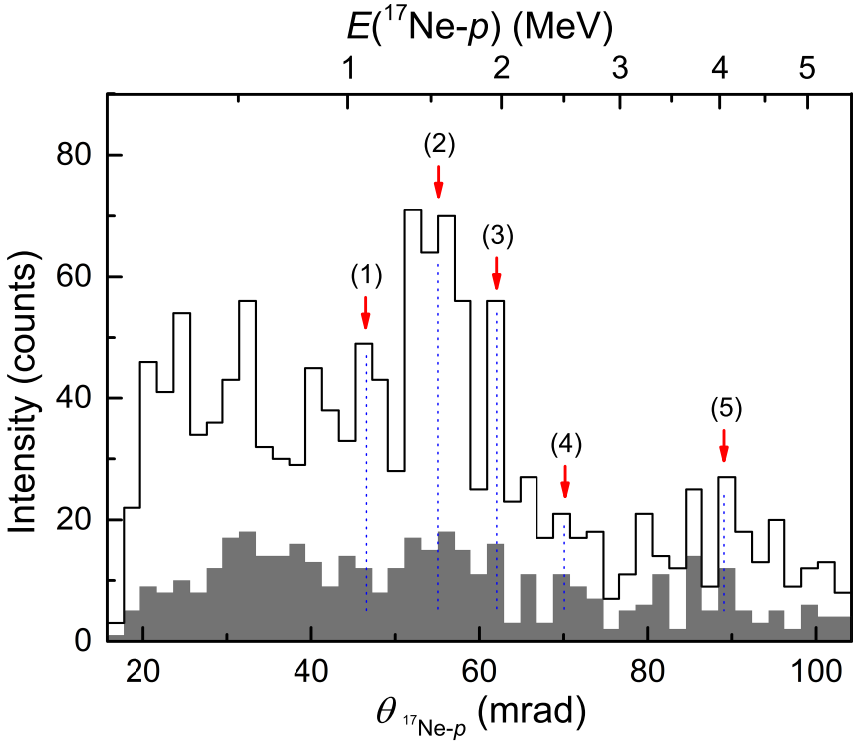

Figure 5.6: $\theta_{^{17}\mathrm{Ne\text{-}p}}$ distribution derived from the measured $^{17}\mathrm{Ne} + p$ coincidences (unfilled histogram) and that deduced from the $^{17}\mathrm{Ne} + p + p$ coincidences (grey-filled histogram). The blue dashed lines together with red arrows indicate the peaks which appear in both histograms and these peaks suggest the ^{18}Na resonances. Previously-known states of ^{18}Na are shown by peaks (1), (2), (3), while peak (4) and (5) suggest two new resonances in ^{18}Na. Corresponding 1p-decay energies are shown in the upper axis in MeV. See text for details.

new ^{18}Na e.s., future experiments with improved conditions (e.g., larger statistics) are required.

5.2.4 Decay Schemes of ^{19}Mg and ^{18}Na

To summarize the decay properties of states observed in ^{19}Mg and ^{18}Na, Figure 5.7 shows the level scheme and decay scenarios concerning the two-proton decays of ^{19}Mg by combining the previously-known results (see Ref. [58]) with the data obtained in the present work. The spins and parities given in parentheses were tentatively assigned in Ref. [58]. As stated in the previous sections, the g.s. and known e.s. of ^{19}Mg are observed in the present work. Their decay energies determined from the present experiment are consistent with those deduced from the previous experiment. Moreover, the evidence on a new e.s. of ^{19}Mg at $8.9^{+0.8}_{-0.7}$ MeV above the 2p threshold are found. It is

tentatively suggested that this new ^{19}Mg state decays by sequential emission of protons via two unknown ^{18}Na resonances at $2.5^{+0.7}_{-0.3}$ MeV and $4.0^{+1.5}_{-0.6}$ MeV above the 1p threshold, respectively. However, the spin-parity (J^{π}) assignment for these newly observed states is out of reach from the present work.

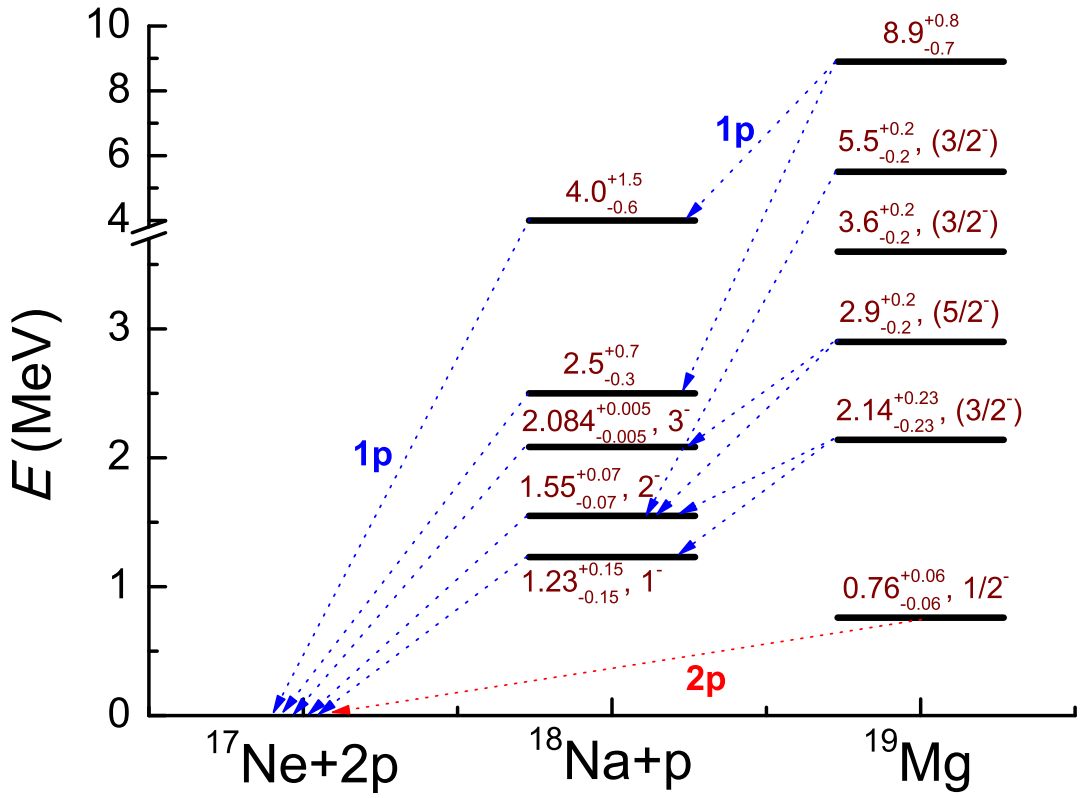

Figure 5.7: Decay schemes of observed states in ^{19}Mg and ^{18}Na. Decay energies (in units of MeV) are given relative to the respective 2p and 1p thresholds. The spins and parities given in parentheses are tentative assignments and taken from Ref. [58]. The energy of ^{18}Na(3^{-}) state is taken from Ref. [121].

6 Nuclear Structure Results of ^{30}Ar Deduced from ^{28}S-Proton Angular Correlations

6.1 ^{28}S-Proton Angular Correlations in 2*p* Decay of ^{30}Ar

The previous chapter shows the experimental results on the two-proton decay of ^{19}Mg: the data obtained in the present work are consistent with the previous experimental results [21, 58]; the 2*p* radioactivity of ^{19}Mg g.s. and sequential 2*p* emission from known ^{19}Mg e.s. are confirmed; moreover, hints of one new e.s. of ^{19}Mg and two new e.s. of ^{18}Na are found, which demonstrate that the tracking technique is a powerful spectroscopic tool to study the in-flight decays of 2*p* precursors with short lifetimes. This has encouraged us to study the decays of previously-unknown nucleus ^{30}Ar as well as its 1*p* decay daughter ^{29}Cl and to deduce their decay properties. It is worth mentioning that all energies of ^{30}Ar states and of ^{29}Cl resonances are given in this chapter and next chapter relative to the ^{28}S+*p*+*p* and ^{28}S+*p* threshold, respectively.

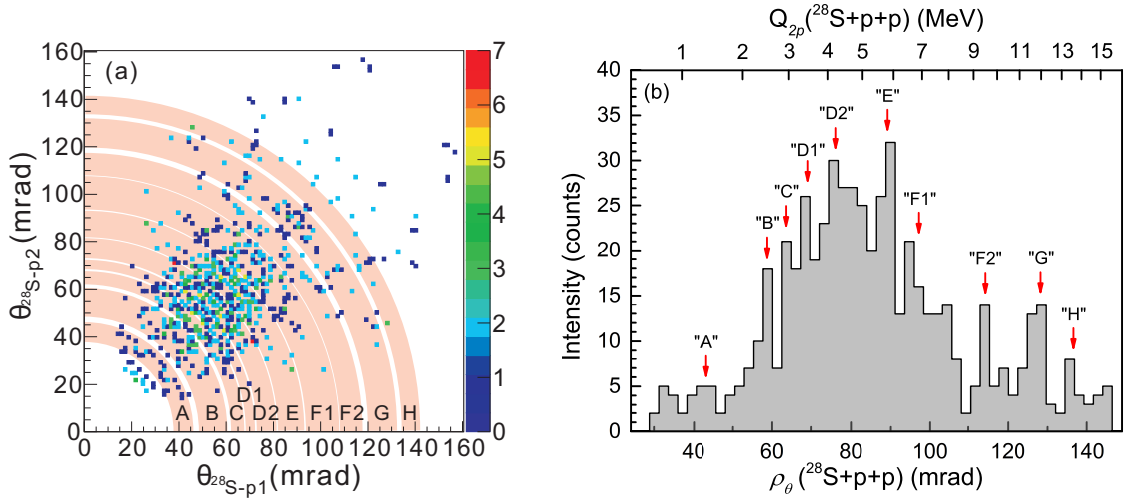

Figure 6.1: ^{28}S-proton angular correlations derived from measured $^{28}\mathrm{S} + p + p$ coincidences. (a) $\theta_{^{28}\mathrm{S\text{-}p1}}$ versus $\theta_{^{28}\mathrm{S\text{-}p2}}$ distribution. (b) The ρ_θ spectrum. The peaks and respective arcs labeled with "A-H" suggest the states of ^{30}Ar. Corresponding 2*p*-decay energies are displayed in the upper axis in MeV. See text for details.

As described in section 4.4, the decays of ^{30}Ar were identified by tracking the coincident $^{28}\mathrm{S} + p + p$ trajectories. Following a similar procedure to that conducted for 2*p* decays of ^{19}Mg, we measured the angle between decay products of ^{30}Ar (i.e., $\theta_{^{28}\mathrm{S\text{-}p}}$ and

$\theta_{p1\text{-}p2}$) and then reconstructed the ^{28}S-proton angular correlations as well as the decay vertices. The scatter plot of $\theta_{^{28}\text{S-p1}}$ versus $\theta_{^{28}\text{S-p2}}$ for all identified $^{28}\text{S} + p + p$ coincidences is shown in Figure 6.1(a). Here proton indexes are given for illustration purposes only. Several statistical enhancements can be observed in this angular correlation plot, and they are the indications for the 2p states of ^{30}Ar and 1p resonances of ^{29}Cl. The arcs labeled "A-H" in Figure 6.1(a) correspond to peaks in the ρ_θ spectrum shown in Figure 6.1(b), where $\rho_\theta = \sqrt{\theta^2_{^{28}\text{S-p1}} + \theta^2_{^{28}\text{S-p2}}}$. As demonstrated in the previous chapter, the ρ_θ distribution is helpful to identify the states of ^{30}Ar and discriminate transitions of interest. In Figure 6.1(b), the prominent peaks labeled "A-H" suggest several states of ^{30}Ar, and corresponding arcs in Figure 6.1(a) illustrate the ^{28}S-proton angular correlation patterns. These arcs and peaks demonstrate the first observation of 2p decays from several states of the previously-unknown nucleus ^{30}Ar. In order to deduce the nuclear structure information on these states and investigate their decay properties, careful analysis of $\theta_{^{28}\text{S-p}}$ patterns and detailed theoretical calculations as well as MC simulations were performed.

6.2 Analysis of the ^{28}S-Proton Angular Correlations

6.2.1 Comparison of $\theta_{^{28}\text{S-p}}$ Distributions Obtained from the $^{28}\text{S}+p$ and $^{28}\text{S}+p+p$ Coincidences

Based on the ^{28}S-proton angular correlations obtained from $^{28}\text{S} + p + p$ triple coincidences, see Figure 6.1, one can identify the ^{30}Ar states populated in the experiment. By comparing the $\theta_{^{28}\text{S-p}}$ distribution obtained from the measured $^{28}\text{S}+p$ double coincidence and that from $^{28}\text{S}+p+p$ triple coincidences, it is also possible to obtain some guidance on the levels in ^{29}Cl, which were populated in the experiment. Such a comparison is displayed in Figure 6.2. In the $^{28}\text{S}+p$ case (see the unfilled histogram in Figure 6.2), the ^{29}Cl states may be populated via several possible reactions on ^{31}Ar, e.g., the two-step reaction $^{31}\text{Ar} \rightarrow {}^{30}\text{Ar} + n$ followed by $^{30}\text{Ar} \rightarrow {}^{29}\text{Cl} + p$, or via direct fragmentation $^{31}\text{Ar} \rightarrow {}^{29}\text{Cl} + n + p$. Concerning the $\theta_{^{28}\text{S-p}}$ spectrum obtained from the $^{28}\text{S} + p + p$ coincidence (grey-filled histogram), population of ^{29}Cl states are presumably due to the 2p emission from ^{30}Ar states. Therefore, one may expect that the $\theta_{^{28}\text{S-p}}$ peaks in both distributions indicate the possible ^{29}Cl states populated by proton decays. In Figure 6.2, several $\theta_{^{28}\text{S-p}}$ peaks (indicated by arrows) with decent intensities coexist in both spectra, which suggest the possible ^{29}Cl resonances.

6.2.2 Assignments of ^{29}Cl States

Concerning the 1p-decay energies of the ^{29}Cl states shown by the arrows in Figure 6.2, one can deduce their values by employing the approximate linear relation between the

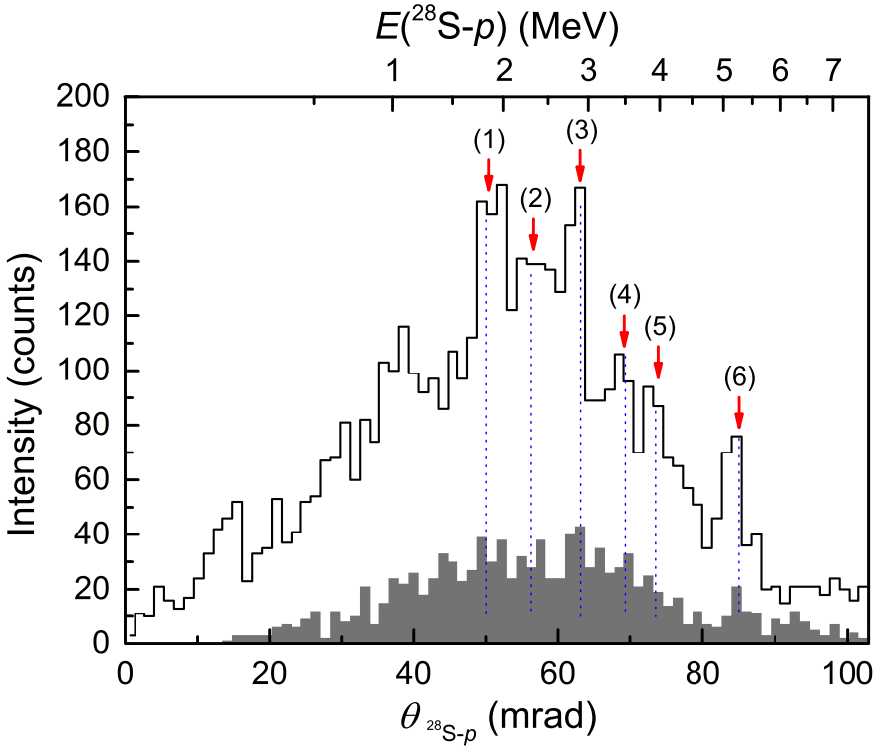

Figure 6.2: Angular correlations $\theta_{^{28}\text{S-p}}$ derived from the measured $^{28}\text{S} + p$ double coincidences (unfilled histogram) and that deduced from the $^{28}\text{S} + p + p$ triple coincidences (grey-filled histogram). The blue broken lines together with red arrows indicate the peaks which appear in both histograms, and they suggest the possible ^{29}Cl resonances, whose 1p-decay energies are shown in the upper axis in MeV.

$\theta_{^{28}\text{S-p}}$ and $\sqrt{Q_{1p}}$, see equation 1.5. The energies of the observed ^{29}Cl levels (1-6) are 1.8(1) MeV, 2.3(1) MeV, $2.9^{+0.2}_{-0.3}$ MeV, $3.5^{+0.4}_{-0.3}$ MeV, $3.9^{+0.6}_{-0.5}$ MeV, and $5.3^{+0.7}_{-0.4}$ MeV, respectively. In order to assign the g.s. of ^{29}Cl, the isobaric symmetry of mirror nuclei was considered. The mirror partner of the $T = 5/2$ nucleus ^{29}Cl is ^{29}Mg. According to [122], the J^π values of ^{29}Mg g.s. are $3/2^+$, and it is separated merely by 55 keV from the first e.s. of ^{29}Mg with $J^\pi = 1/2^+$. The energy levels of ^{29}Mg are displayed in the left part of Figure 6.3, where both experimental data [123] and shell model calculations are displayed. By assuming single-particle structure of ^{29}Mg, the spectrum of ^{29}Cl was studied with a two-body potential cluster model $^{28}\text{S} + p$ [124]. Based on the charge radius of ^{28}S which is 3.21(7) fm derived from systematics of the known isotopes ^{32,34,36}S [125], the Coulomb displacement energy was evaluated. The spin-orbit parameter for the potential model was defined by assuming spin-parity $5/2^+$ for the 1.638 MeV state (i.e., ^{29}Mg state indicated by $(3/2^+,5/2^+)$ in Figure 6.3) in ^{29}Mg. The calculated low-lying energy levels of ^{29}Cl together with the data obtained from the present experiment are shown in the right part of Figure 6.3. The predictions of 1.79 MeV and

2.31 MeV levels for ^{29}Cl are in excellent agreement with the data [126]. In comparison with ^{29}Mg, one can see that the low-lying ^{29}Cl states are displaced (represented by the blue dashed lines) due to a strong Thomas-Ehrman shift (TES), which is an effect violating the fundamental isobaric symmetry in the nuclear structure.

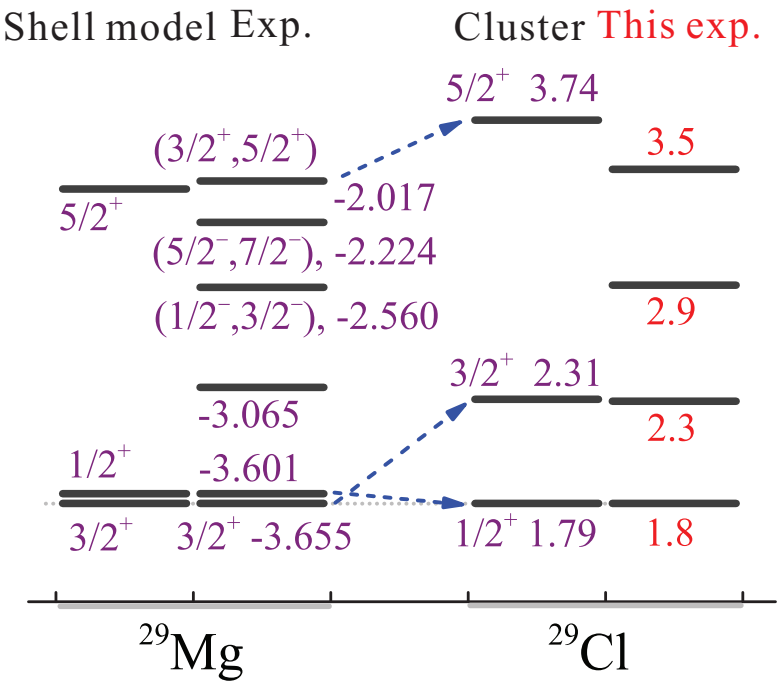

Figure 6.3: Level scheme of ^{29}Cl expected from the states of its isobaric mirror partner ^{29}Mg. Shell-model predictions for ^{29}Mg and results of a cluster potential model for ^{29}Cl are compared with the experimental data.The energies of ^{29}Cl are shown relative to the 1*p* threshold. The energies of ^{29}Mg states were shifted down by 3.655 MeV in order to compare with the mirror states in ^{29}Cl. See text for details. Figure based on [124].

The TES was firstly introduced to the investigation of single-particle states of *sd*-shell nuclei [127, 128]. Given the fact that the *s* and *d* orbitals have different radial extents, the Coulomb interaction may cause the difference of energies of the respective isobaric-mirror states. Such a phenomenon provides a simple way for estimates of dominant orbitals in a nucleus. Investigations of the TES have been extended to nuclei with an even number of "valence" nucleons recently, which can be used for estimates of nuclear configuration mixing [91]. It is known that the TES is responsible for energy anomalies in the nuclei near and beyond the proton drip-line [129]. In the case of ^{29}Cl, our calculations show that its $1/2^+$ g.s. and $3/2^+$ e.s. are at 1.79 MeV and 2.31 MeV above the 1*p* threshold, respectively. Therefore, it is reasonable to assume that the lowest-energy peaks at 1.8 MeV and 2.3 MeV in Figure 6.2 match the $1/2^+$ and $3/2^+$ states expected in ^{29}Cl [126].

6.2.3 $\theta_{^{28}\mathrm{S\text{-}p}}$ Distributions of Observed ^{30}Ar States

The assignments of several ^{29}Cl states in the previous section are important for the study of the decay mechanisms of observed ^{30}Ar states. Especially, the identification of ^{29}Cl g.s. and determination of its location play a crucial role in uncovering the decay mechanism of ^{30}Ar g.s. (see subsection 7.1.3). In the following, the experimental ^{28}S-proton angular correlations from ^{30}Ar decays will be carefully analyzed.

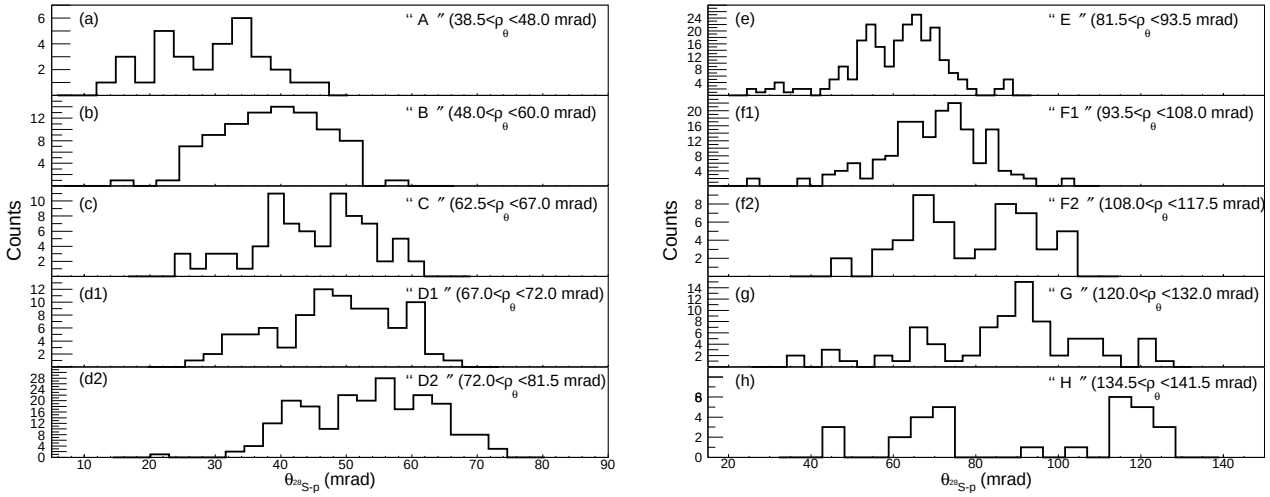

Figure 6.4: Angular correlations $\theta_{^{28}\mathrm{S\text{-}p}}$ derived from the measured $^{28}\mathrm{S}+p+p$ coincidences by using ρ_θ gates shown in Figure 6.1. Corresponding ρ_θ ranges for the peaks "A", "B", "C", "D1", "D2", "E", "F1", "F2", "G", and "H" are $38.5 < \rho_\theta < 48.0$ mrad (panel (a)), $48.0 < \rho_\theta < 60.0$ mrad (panel (b)), $62.5 < \rho_\theta < 67.0$ mrad (panel (c)), $67.0 < \rho_\theta < 72.0$ mrad (panel (d1)), $72.0 < \rho_\theta < 81.5$ mrad (panel (d2)), $81.5 < \rho_\theta < 93.5$ mrad (panel (e)), $93.5 < \rho_\theta < 108.0$ mrad (panel (f1)), $108.0 < \rho_\theta < 117.5$ mrad (panel (f2)), $120.0 < \rho_\theta < 132.0$ mrad (panel (g)), and $134.5 < \rho_\theta < 141.5$ mrad (panel (h)), respectively.

Since the $\theta_{^{28}\mathrm{S\text{-}p}}$ distributions reflect energy spectra of protons emitted from the 2*p* decay of ^{30}Ar states, they provide insight into the decay mechanisms of the present states. The pattern of the $\theta_{^{28}\mathrm{S\text{-}p}}$ distribution carries information on the decay branches of the ^{30}Ar state. Figure 6.4 displays the $\theta_{^{28}\mathrm{S\text{-}p}}$ spectra obtained from $^{28}\mathrm{S}+p+p$ coincidences which are selected by imposing the ρ_θ gates "A", "B", "C", "D1", "D2", "E", "F1", "F2", "G", and "H" shown in Figure 6.1. As explained in section 5.1, the proton spectrum of a simultaneous 2*p* decay of a state exhibits a peak which corresponds to the half of total 2*p*-decay energy Q_{2p}. In the case of the sequential emission of protons, a typical double-peak structure appears in the proton spectrum and the two peaks are related to the decay energies of two two-body decays, i.e., one peak locates at the decay energy of

the intermediate state of 1p-decay daughter nucleus (Q_{1p}) and the other peak sits around the 1p-decay energy of the mother nucleus (i.e., $Q_{2p} - Q_{1p}$). Moreover, multiple-peak structures may also be present in the proton spectrum, which indicate two or more decay branches. Therefore, one can obtain hints of the decay mechanism on the basis of the angular $\theta_{^{28}\mathrm{S\text{-}p}}$ distribution. In the case of ^{30}Ar, one can see in Figure 6.4 that except the state "B", all other ^{30}Ar states show two or more $\theta_{^{28}\mathrm{S\text{-}p}}$ peaks, which indicate a sequential decay mechanism. Concerning peak "B", the angular ^{28}S-proton spectrum presents a relatively broad peak which is wider than that expected for a simultaneous 2p decay. In section 7.1, such an unexpected pattern will be explained by a mechanism in the transition region between simultaneous 2p decay and sequential emission of protons. Regarding the state "H", we will not discuss it further due to the very small amount of decay events observed from this state.

6.2.4 Decay Schemes of ^{30}Ar and ^{29}Cl

In the present work, several states of ^{30}Ar are observed by analyzing the ^{28}S-proton angular correlations reconstructed from $^{28}\mathrm{S} + p + p$ coincidences. Meanwhile, the comparison of $\theta_{^{28}\mathrm{S\text{-}p}}$ spectrum obtained from $^{28}\mathrm{S} + p$ coincidences and that deduced from $^{28}\mathrm{S} + p + p$ coincidences suggests several low-lying excited states in ^{29}Cl. The g.s. and first e.s. of ^{29}Cl were found with the help of the theoretical calculations by taking isobaric mirror symmetry into account. Combining these results, we derived a tentative level scheme together with the decay branches for the observed ^{30}Ar and ^{29}Cl states. It is shown in Figure 6.5. One can see that except the state "B", all other states of ^{30}Ar decay by sequential emission of protons via the ^{29}Cl resonances. In the following chapter, this decay scheme will be interpreted in detail. In particular, the determination of the decay energy and the investigation of the decay mechanism will be discussed state by state.

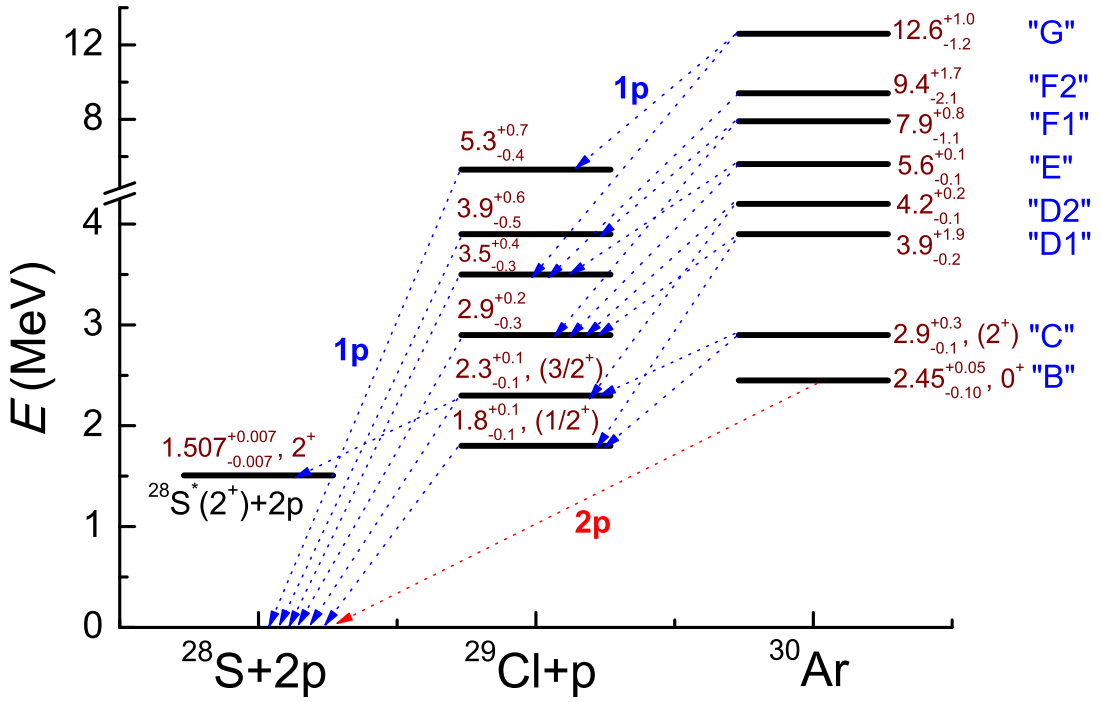

Figure 6.5: Proposed decay schemes of observed ^{30}Ar and ^{29}Cl states, whose decay energies (in units of MeV) are given relative to the 2p and 1p thresholds, respectively. The spins and parities given in parentheses are tentative assignments taken from [126]. The energy of ^{28}S(2^+) is taken from [130].

7 Discussion of the Measured Decay Properties

As described in the previous chapter, we have performed the analysis of ^{28}S-Proton angular correlations, and we have obtained the decay scheme shown in Figure 6.5. In order to explore the decay mechanisms of the observed states in ^{30}Ar and quantitatively interpret the experimental $\theta_{^{28}\text{S-p}}$ spectra displayed in Figure 6.4, theoretical calculations and Monte Carlo simulations were conducted. In this chapter, the assignment of the ground state of ^{30}Ar and the investigation of its decay properties will be presented. Then the determination of the decay mechanism and the extraction of spectroscopic information on several excited states in ^{30}Ar as well as related states in ^{29}Cl will be demonstrated. It is worth mentioning that most of results presented here have already been published in Ref. [126].

7.1 Two-Proton Decay of the ^{30}Ar Ground State

7.1.1 Assignment of the ^{30}Ar Ground State

The ρ_θ spectrum shown in Figure 6.1(b) displays the excitation spectrum of ^{30}Ar. Since the ρ_θ value is in direct proportion to the square root of 2*p* decay energy of ^{30}Ar, i.e., $\rho_\theta \sim \sqrt{Q_{2p}}$, one may expect that the lowest ρ_θ peak (peak "A"), which corresponds to the smallest Q_{2p} of 1.4 MeV, is the g.s. of ^{30}Ar. However, there are three arguments against peak "A" to be assigned to the ^{30}Ar ground state. First, if peak "A" is the ^{30}Ar g.s., then a consistent description of all observed ^{30}Ar states and their decays is not possible. Second, the intensity of peak "A" in Figure 6.1(b) is rather small in comparison with the intensities of other peaks. It is abnormal for a g.s. population. According to the previous studies on ^{16}Ne and ^{19}Mg, which were also produced via neutron-knockout reactions at intermediate energy [18,21,95], cross sections of the g.s. population and the e.s. population are similar. The above conclusion is also confirmed by the investigations of other 2*p* emitters, ^{6}Be, ^{12}O, and ^{16}Ne at lower energies [16, 20, 31]. In this sense, in the excitation spectrum of ^{30}Ar (Figure 6.1(b)), the surprisingly small population of peak "A" hardly makes it the ground state. The third argument is provided by the systematics of odd-even staggering of nuclear masses, which is quantitatively described in the following subsection.

7.1.2 Systematics of Odd-Even Mass Staggering

The odd-even staggering (OES) of nuclear masses is an effect which has often been associated with the nuclear pairing gap. The OES can be defined as

$$E_{OES} = \frac{1}{2}(2S_N - S_{2N}), \tag{7.1}$$

where S_N and S_{2N} are one-nucleon (either proton or neutron) and two-nucleon separation energies, respectively. Usually, the values for the OES display a slow trend as a function of mass number A [131].

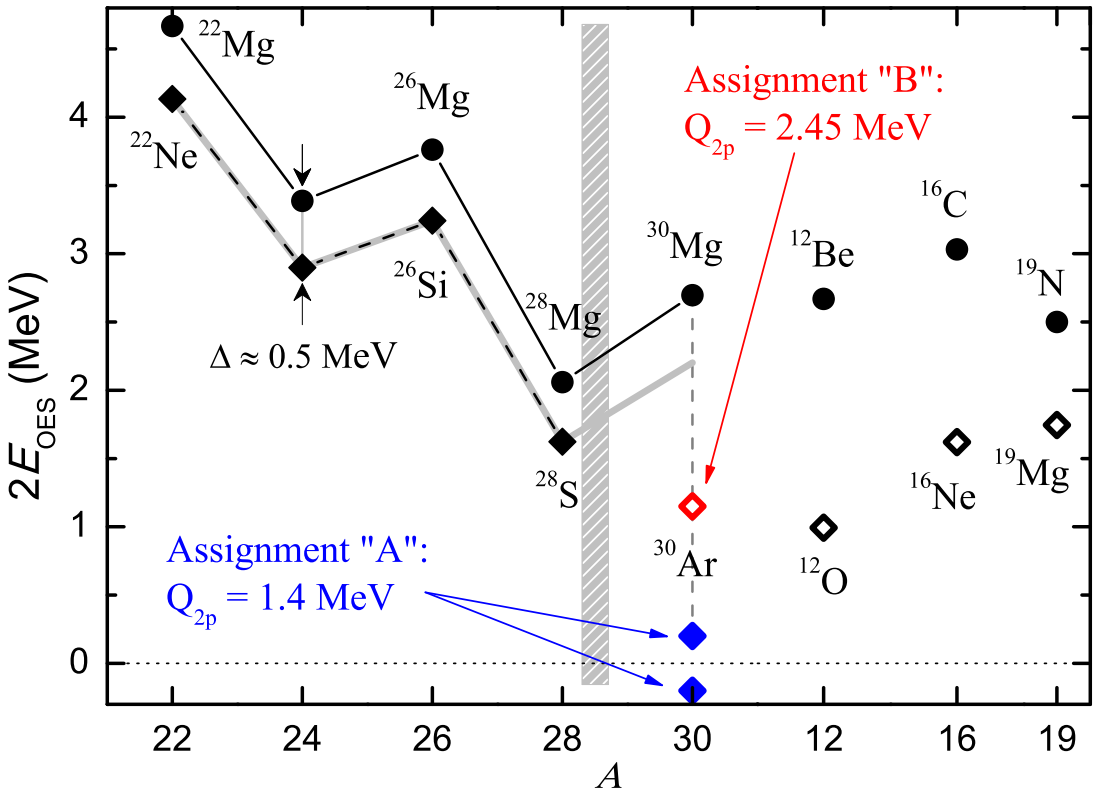

Figure 7.1: Odd-even mass staggering for some mirror nuclei with mass numbers A around 30. The left part of the grey bar: E_{OES} values for bound Mg isotopes and their isobaric mirrors are shown by solid and dashed lines, respectively. A small constant shift of about 0.5 MeV can be clearly seen. The right part of the grey bar: Data for known s-d shell 2*p* emitters and their bound mirror nuclei. The $2E_{OES}$ assignments stemming from $Q_{2p}(^{30}\mathrm{Ar})$ of 1.4 MeV and 2.45 MeV are shown by blue and red diamonds, respectively.

The OESs of Mg ($Z = 12$) isotopes and $N = 12$ isotones as a function of mass number A are shown in Figure 7.1. Here, the OES of ^{30}Ar and its mirror partner ^{30}Mg are also displayed. One can clearly observe an almost constant shift $\Delta \approx 0.5$ MeV between

bound $Z = 12$ and $N = 12$ partners up to $A = 28$. However, this trend breaks down in the case of unbound ^{30}Ar. Based on the excitation spectrum shown in Figure 6.1(b), we made two prescriptions for ^{30}Ar g.s. If we assign the ^{30}Ar g.s. to the lowest-lying peak "A" ($Q_{2p} = -S_{2p} = 1.4$ MeV), there may be two possible E_{OES} values since Figure 6.4(a), which shows the proton spectrum obtained by using gate "A", indicates a sequential 1*p* emission with $Q_p = -S_p$ of either 0.6 or 0.8 MeV. The respective E_{OES} values are either -0.2 or 0.2 MeV, which are shown by blue diamonds in Figure 7.1. Both OES values are around-zero and do not match any reasonable structure of ^{30}Ar g.s. Combining this strong argument with those two explained in the last subsection, the 1.4 MeV g.s. assignment can be ruled out [126]. On the other hand, if the second lowest-energy peak "B" ($Q_{2p} = 2.45$ MeV) in Figure 6.1(b) is assigned to the ^{30}Ar g.s., corresponding E_{OES} value is about 1.2 MeV (shown by the red-hollow diamond in Figure 7.1) for the $Q_p = 1.8$ MeV of the ^{29}Cl g.s. This E_{OES} value is about 1 MeV below the one expected from the systematic trend of E_{OES} versus A (see the grey line in Figure 7.1). However, as shown in the right part of Figure 7.1, the E_{OES} values of other known s-d shell 2*p* emitters, i.e., ^{12}O, ^{16}Ne, and ^{19}Mg, demonstrate a lowering trend while the prescription of 2.45 MeV ^{30}Ar g.s. assignment fits the trend well [126]. Therefore, it is reasonable to assign peak "B" to the ^{30}Ar ground state. The decay mechanism and mass as well as half-life of ^{30}Ar g.s. are discussed in the following subsections. Concerning peak "A", we assume it originates from a decay branch of the ^{30}Ar$^*(2^+)$ state (peak "C" with $Q_{2p} = 2.9$ MeV) into the excited 2^+ state of ^{28}S (see Figure 6.5), which is detailed described in subsection 7.2.1.

7.1.3 Decay Mechanism of the ^{30}Ar Ground State

As stated in the previous section, peak "B" in Figure 6.1(b) is assumed to be the ^{30}Ar ground state. The proton spectrum from 2*p* decay of this state is shown in Figure 6.4(b). On one hand, the broad pattern of the $\theta_{^{28}\mathrm{S\text{-}p}}$ distribution is almost twice wider than the one predicted by a true 2*p* decay mechanism. On the other hand, the spectrum does not point to a sequential 2*p* emission, where the typical double-peak structure appears. To solve this puzzle, a simple analytical direct decay model was applied [9]. This theoretical approach approximates well both the true and sequential 2*p* decay mechanisms and yields a smooth transition between them [65, 88]. The main features of this model are briefly described below.

Proton p_i (emitted with angular momentum j_i) is considered to populate an intermediate HI-*p* resonance at E_{ji}. Two protons share the total 2*p*-decay energy Q_{2p} which is described by the parameter $\varepsilon = E(HI - p)/Q_{2p}$. The *p*-*p* final state interaction is treated in a phenomenological sufficient way. The 2*p*-decay spectra are described by

the 2*p*-precursor's width, and it is given by the following formula:

$$\begin{aligned}\Gamma(Q_{2p}) &= \frac{Q_{2p}< V_3 >^2}{2\pi}\int_0^1 d\varepsilon \frac{\Gamma_{j1}(\varepsilon Q_{2p})}{(\varepsilon Q_{2p}-E_{j1})^2+\Gamma_{j1}(\varepsilon Q_{2p})^2/4} \\ &\times \frac{\Gamma_{j2}[(1-\varepsilon)Q_{2p}]}{[(1-\varepsilon)Q_{2p}-E_{j2}]^2+\Gamma_{j2}[(1-\varepsilon)Q_{2p}]^2/4}. \end{aligned} \quad (7.2)$$

In this equation, Γ_{ji} are the standard R-matrix expressions for 1*p*-decay widths as a function of energy of the involved resonances in the $^{28}S + p_i$ subsystems. The matrix element $< V_3 >$ can be approximated by the expression $< V_3 >^2 \approx (2E_{OES})^2$ [9, 88].

Based on the above introduced direct decay model, we have performed calculations of the dependence of the proton spectrum on the 2*p* decay energy of ^{30}Ar g.s. ($Q_{2p}(^{30}\mathrm{Ar})$) and on the width of ^{29}Cl g.s. ($\Gamma(^{29}\mathrm{Cl})$). The Figure 7.2(a) displays the calculated energy distributions between the ^{28}S and one of the emitted protons in the "Y" Jacobi system. In the calculations, the resonant energy of ^{29}Cl ground state $Q_p(^{29}\mathrm{Cl})$ is set to 1.8 MeV and the $\Gamma(^{29}\mathrm{Cl})$ is fixed at 92 keV. It can be clearly seen that the shape and width of the spectrum change dramatically with the variation of $Q_{2p}(^{30}\mathrm{Ar})$, which represents a strong sensitivity of the decay mechanism to the $Q_{2p}(^{30}\mathrm{Ar})$. In the case of small $Q_{2p}(^{30}\mathrm{Ar})$, e.g., of 2.35 MeV, the energy distribution between ^{28}S and proton (blue dashed curve in Figure 7.2(a)) is mainly characterized by a bell-like spectrum centered at $\varepsilon = 0.5$, which indicates the true 2*p* decay. In contrast, the spectrum with a bit larger $Q_{2p}(^{30}\mathrm{Ar})$ value (say, $Q_{2p}(^{30}\mathrm{Ar}) = 2.50$ MeV, the green dashed-dotted curve in Figure 7.2(a)) is mainly featured by a double-peak pattern (with two peaks at $\varepsilon = 0.75$ and at $\varepsilon = 0.25$), which typically corresponds to the sequential 2*p* emission. Therefore, the correlation pattern is extremely sensitive to calculation parameters, where small variations of $Q_{2p}(^{30}\mathrm{Ar})$ cause dramatic changes of the shapes of distributions. The decay energy of ^{30}Ar g.s. (black solid curve in Figure 7.2(a)) is located in a transition region between the true three-body decay mechanism and the sequential two-body decay mechanism. Similarly, the sensitivity of the energy distribution to $\Gamma(^{29}\mathrm{Cl})$ was also investigated. Corresponding results are shown in Figure 7.2(b). Here $Q_{2p}(^{30}\mathrm{Ar}) = 2.45$ MeV and $Q_p(^{29}\mathrm{Cl}) = 1.8$ MeV. With the increase of $\Gamma(^{29}\mathrm{Cl})$, an obvious change from a sequential two-body decay case to a true three-body decay situation can be observed.

In order to compare the model predictions of the ^{28}S-*p* angular correlations with the experimental data, Monte Carlo simulations of the detector response to the 2*p* decay of ^{30}Ar g.s. were performed. The momenta of three decay products used in the simulations were taken from the predictions of the direct decay model. Corresponding results are shown in panel (c) and (d) of Figure 7.2, which illustrate the dependence of the simulated $\theta_{^{28}\mathrm{S\text{-}p}}$ spectrum on $Q_{2p}(^{30}\mathrm{Ar})$ and $\Gamma(^{29}\mathrm{Cl})$, respectively. In comparison of experimental $\theta_{^{28}\mathrm{S\text{-}p}}$ distribution (grey histogram with statistical uncertainties) and virous

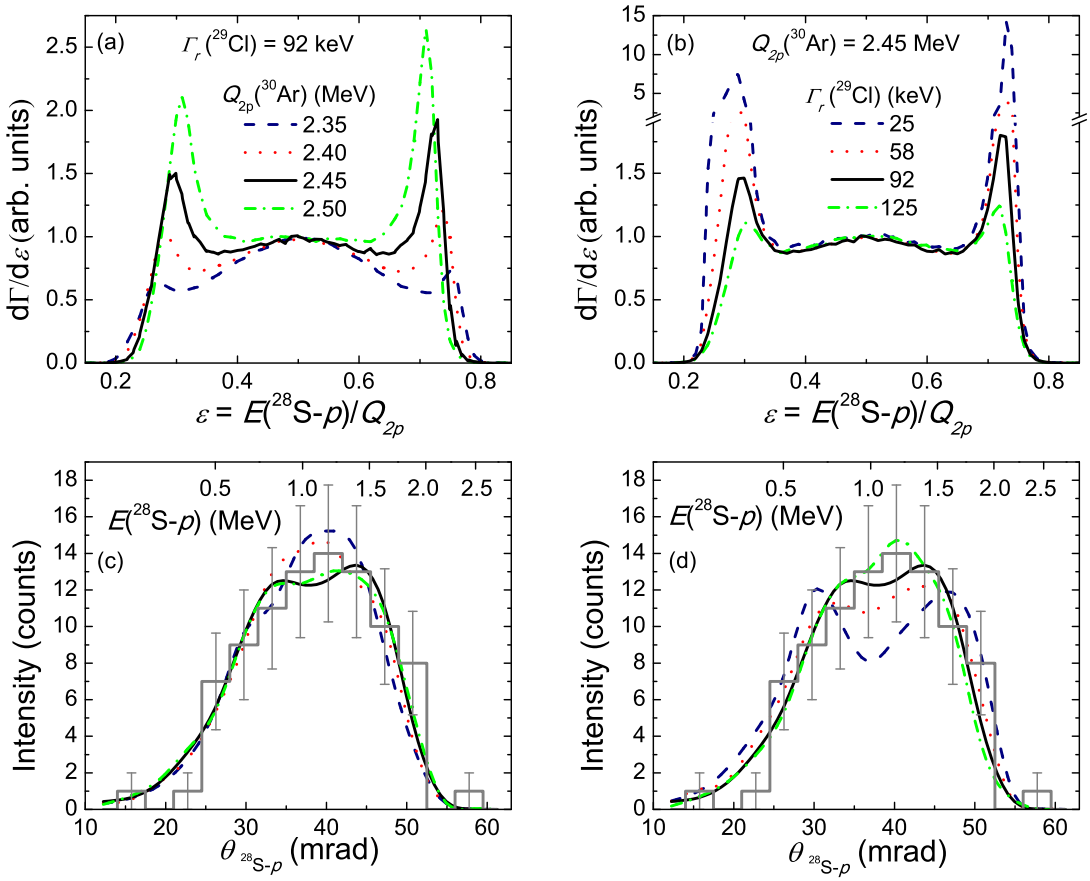

Figure 7.2: Transition from the true-2p decay mechanism to the sequential proton emission mechanism. (a) Proton spectrum calculated in the "Y" Jacobi system by employing equation 7.2, where the 2p-decay energy of ^{30}Ar is varied. (b) Same as (a) but for the variation of the width of ^{29}Cl g.s. In the panels (c) and (d), the experimental $\theta_{^{28}\mathrm{S\text{-}p}}$ distribution measured for the decay of ^{30}Ar g.s. (grey histogram with statistical uncertainties) is compared with those stemming from respective theoretical distributions in panels (a) and (b) after experimental bias is taken into account via Monte Carlo simulations. See text for details.

simulations, the model prediction with $Q_{2p} = 2.45$ MeV and $\Gamma(^{29}\mathrm{Cl}) = 92$ keV (black solid curve in panel (c) and (d) of Figure 7.2) reproduces the data. Based on these investigations, it is found that the decay of ^{30}Ar g.s. occurs exactly in an intermediate situation when two "satellite peaks", originating from sequential emission of protons, begin to grow on either side of the central bump, which results from true 2p decays. This is the first observation of such an interplay between two 2p-decay mechanisms of a nuclear ground state. It is worth mentioning that the transition dynamics of ^{30}Ar g.s. decay have been further investigated by employing a improved direct-decay model.

The sensitivity of energy distributions of decay products to reasonable combinations of parameters $\{Q_{2p}(^{30}\mathrm{Ar})$, $Q_p(^{29}\mathrm{Cl})$, $\Gamma(^{29}\mathrm{Cl})\}$ was systematically investigated. Corresponding results demonstrate a surprisingly strong sensitivity of the decay correlation patterns to the variation of all three parameters [132].

7.1.4 Mass of the ^{30}Ar Ground State

On the basis of the measured 2*p*-decay energy of ^{30}Ar g.s. and the 1*p*-decay energy of ^{29}Cl g.s., one can directly obtain the one-proton and two-proton separation energies of ^{30}Ar ($S_p(^{30}\mathrm{Ar})$ and $S_{2p}(^{30}\mathrm{Ar})$) as well as the one-proton separation energy of ^{29}Cl ($S_p(^{29}\mathrm{Cl})$). Furthermore, with the combination of the mass of ^{28}S g.s. and the proton mass as well as $Q_{2p}(^{30}\mathrm{Ar})$ and $Q_p(^{29}\mathrm{Cl})$, one can deduce the mass of ^{30}Ar and ^{29}Cl. In order to compare the mass values obtained in the present work with those tabulated in the latest Atomic Mass Evaluation (AME2012 [133]), the mass excess of ^{30}Ar ($ME(^{30}\mathrm{Ar})$) and ^{29}Cl ($ME(^{29}\mathrm{Cl})$) were deduced from the mass of ^{30}Ar and ^{29}Cl by taking into account binding energies of electrons. In Table 7.1, the $ME(^{30}\mathrm{Ar})$, $S_p(^{30}\mathrm{Ar})$, $S_{2p}(^{30}\mathrm{Ar})$, $ME(^{29}\mathrm{Cl})$, and $S_p(^{29}\mathrm{Cl})$ obtained in the present work are presented. Corresponding values from AME2012 are also tabulated. It is also worth mentioning that the one-proton separation energy of ^{30}Ar predicted by using the relativistic mean field theory [134] agrees very well with the experimental data obtained in the present work.

Table 7.1: Mass excess and one-proton separation energy of ^{30}Ar ground state and ^{29}Cl ground state as well as two-proton separation energy of ^{30}Ar ground state obtained in the present work. Corresponding values from AME2012 [133] are also given (# indicates extrapolated values).

Quantity	this work	AME2012
$ME(^{30}\mathrm{Ar})$ (keV)	21094^{+168}_{-189}	$21490(500)^{\#}$
$S_p(^{30}\mathrm{Ar})$ (keV)	-650^{+112}_{-141}	$-432(640)^{\#}$
$S_{2p}(^{30}\mathrm{Ar})$ (keV)	-2450^{+50}_{-100}	$-2842(530)^{\#}$
$ME(^{29}\mathrm{Cl})$ (keV)	$13157(189)$	$13770(400)^{\#}$
$S_p(^{29}\mathrm{Cl})$ (keV)	$-1800(100)$	$-2412(430)^{\#}$

7.1.5 Half-life of the ^{30}Ar Ground State

As stated in subsection 1.5.3, the information on the half-life of the 2*p* precursor may be deduced from the decay vertex distribution. The histograms with statistical uncertainties in Figure 7.3 show the distributions of the z coordinate (along the beam direction) of the measured decay vertices from the $^{28}\mathrm{S} + p + p$ coincidences. In Figure 7.3(a), the

experimental vertex distribution for the short-lived excited states of ^{30}Ar is compared with the Monte Carlo simulations of the detector response to the 2*p* decay of ^{30}Ar under different $T_{1/2}$ assumptions. The MC simulation obtained by assuming the $T_{1/2} \simeq 0$ for the ^{30}Ar states reproduces the data quantitatively. The uncertainty of half-life can be estimated by the $T_{1/2} = 5$ ps simulation, which fails to fit the data. Due to multiple scattering of the fragments in the thick target, the rising and falling slopes of the vertex distribution is asymmetric. The vertex profile shown in Figure 7.3(a) serves as the reference for estimating the $T_{1/2}$ of the ^{30}Ar g.s.. In Figure 7.3(b), the vertex profiles obtained from the MC simulations of ^{30}Ar g.s. decay with $T_{1/2} = 0$ and $T_{1/2} = 10$ ps are compared with corresponding experimental decay vertex distribution. One can clearly see that the $T_{1/2} \simeq 0$ simulation agrees with the experimental data. The simulation with $T_{1/2} = 10$ ps serves for illustration purpose. Therefore, the half-life of the ^{30}Ar g.s. is shorter than 10 ps, which can be treated as the upper limit. It is worth mentioning that the $T_{1/2}$ of ^{30}Ar g.s. predicted by NUBASE2012 is less than 20 ns [135].

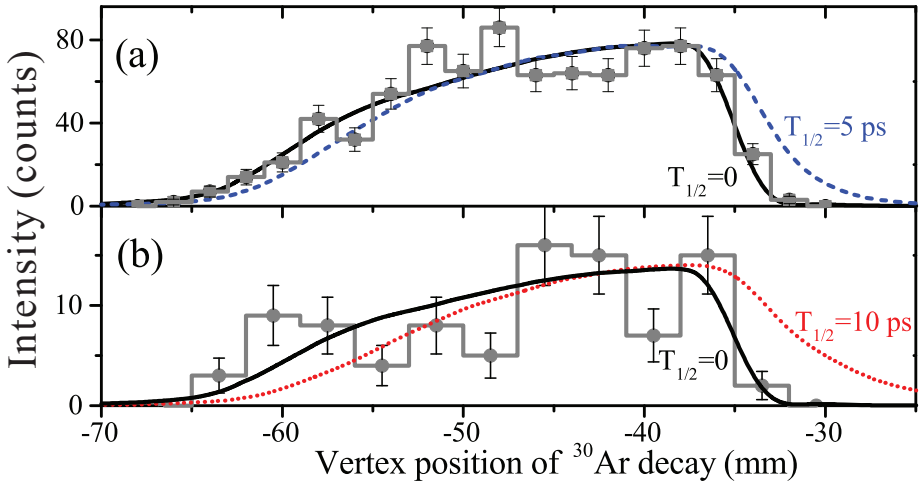

Figure 7.3: Distributions of the z coordinate (along the beam direction) of $^{30}\mathrm{Ar} \rightarrow {}^{28}\mathrm{S} + p + p$ decay vertices with respect to the closest SSD. (a) The experimental vertex distribution gated by large angles $\rho_\theta > 60$ mrad, which corresponds to short-lived excited states in ^{30}Ar. (b) The data selected by using the gate $45 < \rho_\theta < 55$ mrad where the ground state of ^{30}Ar is expected. The solid, dashed, and dotted curves show the Monte Carlo simulations of the detector response to the ^{30}Ar 2*p* decays with the half-life values of 0, 5 ps, and 10 ps, respectively. Figure taken from [126].

Theoretical calculations of the ^{30}Ar g.s. half-life were also performed by using the above-mentioned direct decay model. The predicted ^{30}Ar half-life is shown as a function of the total 2*p*-decay energy Q_{2p} by red-solid curves in Figure 7.4. For comparison, the true 2*p* decay model [94] and the sequential emission model were also applied to investigate the dependence of the ^{30}Ar g.s. half-life on the assumed Q_{2p}. The calculated

"half-life range" is shown by the green-dotted and blue-dashed curves, respectively. In the true 2*p*-decay calculations, the 1*p*-decay energy of the ^{29}Cl g.s. $Q_p(^{29}\mathrm{Cl})$ is assumed to be 1.8 MeV. In the sequential-emission model and direct decay model, s-wave 1*p* emission via the ^{29}Cl g.s. at 1.8 ± 0.1 MeV above the 1*p* threshold is assumed. In both model predictions, the thick lines represent the result with $Q_p(^{29}\mathrm{Cl}) = 1.8$ MeV while the two thin curves correspond to the $Q_p(^{29}\mathrm{Cl})$ extreme values of 1.7 MeV and 1.9 MeV. One can see that the measured ^{30}Ar g.s. energy range (i.e., $Q_{2p} = 2.45^{+0.05}_{-0.10}$ MeV, see right-hatched box in Figure 7.4) is located in the transition region between true 2*p* decay and sequential emission of protons. Based on the direct decay model calculations, the estimated half-life of ^{30}Ar g.s. is within the range of 10^{-18} to 10^{-17} s, which is below the $T_{1/2}$ upper limit of 10^{-11} s deduced from the measured decay vertex distribution. Such a very short half-life is out of reach of the decay-in-flight technique (see left-hatched area in Figure 7.4).

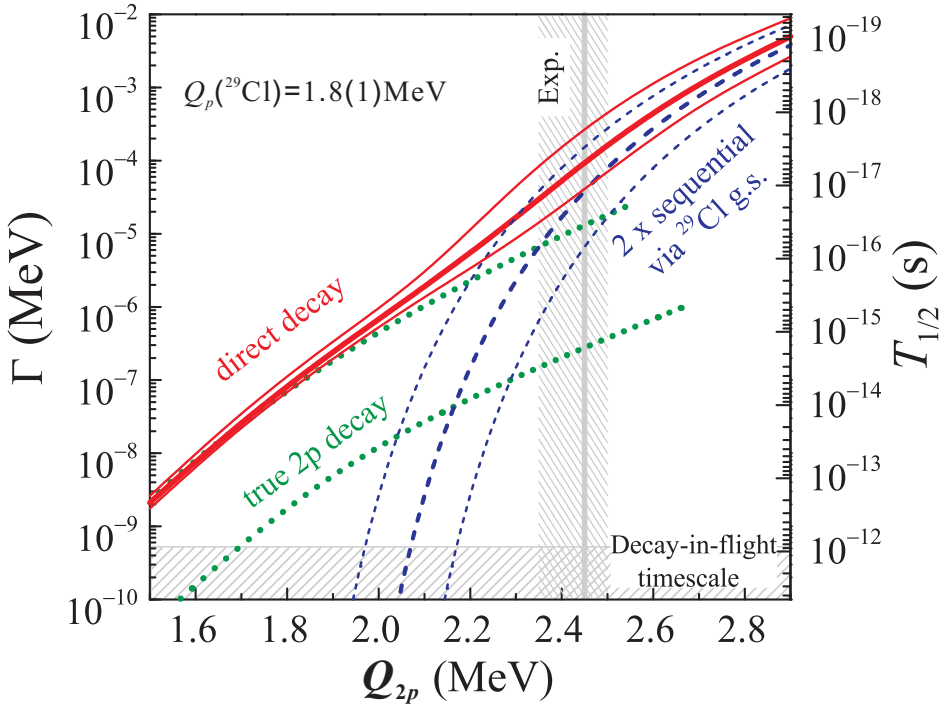

Figure 7.4: Half-life predictions for the ^{30}Ar ground state calculated with different decay mechanisms. The true 2*p*-decay calculations shown by green-dotted curves are from Ref. [94]. The half-life predictions by sequential-emission and direct decay model are displayed by blue-dashed and red-solid curves, respectively. The right hatched bar and vertical line show the $Q_{2p} = 2.45^{+0.05}_{-0.10}$ MeV range. The left hatched area indicates the half-life range accessible by decay-in-flight technique. See text for details. Figure taken from [124].

7.2 Decay Mechanism of the $^{30}\mathrm{Ar}^{*}(2^{+})$ State

In the previous section, we have demonstrated that the ^{30}Ar g.s. corresponds to peak "B" in Figure 6.1(b). Now let us explore the decay mechanism of peak "C" ($Q_{2p} = 2.9^{+0.3}_{-0.1}$ MeV), which is the lowest excited state of ^{30}Ar observed in the present work. The angular $\theta_{^{28}\mathrm{S\text{-}p}}$ distribution obtained by gating the $^{28}\mathrm{S} + p + p$ coincidences with ρ_θ in peak "C" is shown in Figure 6.4(c). There are three bumps in the spectrum and two of them match the g.s. and the first e.s. of ^{29}Cl, which are located at 1.8 MeV and 2.3 MeV above than the 1p threshold, respectively, see Figure 6.5. This indicates that the ^{30}Ar e.s. at 2.9 MeV may decay by two branches of sequential emission protons via the above-mentioned two ^{29}Cl states. Corresponding Monte Carlo simulations under the above hypothesis were performed. The simulated $\theta_{^{28}\mathrm{S\text{-}p}}$ spectra are compared to the experimental distribution shown in Figure 7.5(a). The calculation reproduces the data well. Therefore, peak "C" in Figure 6.1(b) can be attributed to the decay of the ^{30}Ar 2.9 MeV state to the ^{28}S g.s. via the g.s. and the first e.s. of ^{29}Cl. The spin-parity of this state is assumed to be 2^{+} like in its mirror nucleus ^{30}Mg [126].

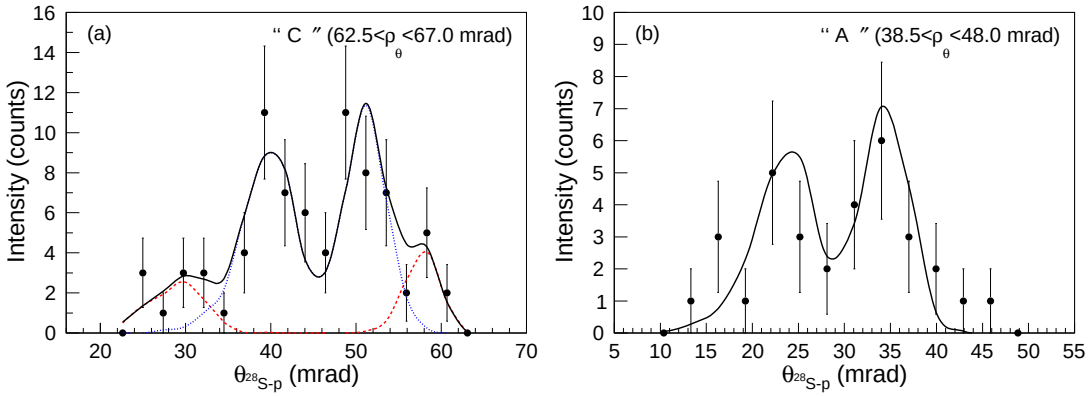

Figure 7.5: Angular $\theta_{^{28}\mathrm{S\text{-}p}}$ distributions related to the decays of $^{30}\mathrm{Ar}^{*}(2^{+})$ state. (a) The data (black dots with statistical uncertainties) are selected from the $^{28}\mathrm{S} + p + p$ coincidences by using the ρ_θ gate "C", $62.5 < \rho_\theta < 67.0$ mrad. Simulations of sequential decays $^{30}\mathrm{Ar}^{*}(2^{+}) \rightarrow {}^{29}\mathrm{Cl}^{*}(3/2^{+}) \rightarrow {}^{28}\mathrm{S}$ and $^{30}\mathrm{Ar}^{*}(2^{+}) \rightarrow {}^{29}\mathrm{Cl}^{*}(1/2^{+}) \rightarrow {}^{28}\mathrm{S}$ are shown by dashed curve and dotted curve, respectively. The solid curve displays the sum fit. (b) The experimental $\theta_{^{28}\mathrm{S\text{-}p}}$ spectrum (black dots with statistical uncertainties) obtained by gating the ^{30}Ar 2p decay events within peak "A", $38.5 < \rho_\theta < 48.0$ mrad. The solid curve shows the $\theta_{^{28}\mathrm{S\text{-}p}}$ distribution obtained from the simulation of a sequential 2p decay $^{30}\mathrm{Ar}^{*}(2^{+}) \rightarrow {}^{29}\mathrm{Cl}^{*}(3/2^{+}) \rightarrow {}^{28}\mathrm{S}^{*}(2^{+})$. See text for details.

Concerning peak "A", we assume that it also originates from the decay of ^{30}Ar e.s. at 2.9 MeV. Specifically, the 2.9 MeV e.s. of ^{30}Ar decays to the 2.3 MeV e.s. in ^{29}Cl

which is followed by the 1*p* emission of 2.3 MeV e.s. of ^{29}Cl to the known 2^+ state of ^{28}S at 1.51 MeV above the ground state. These two successive transitions provide a reasonable explanation of the low-energy peak (0.6 MeV) and the high-energy peak (0.8 MeV) in the angular $\theta_{^{28}\mathrm{S\text{-}p}}$ distribution related to peak "A" (see Figure 6.4(a)). According to this assumption, we performed Monte Carlo simulations of the detector response to the sequential 2*p* decay $^{30}\mathrm{Ar}^*(2^+) \rightarrow {}^{29}\mathrm{Cl}^*(3/2^+) \rightarrow {}^{28}\mathrm{S}^*(2^+)$. In Figure 7.5(b), the simulated $\theta_{^{28}\mathrm{S\text{-}p}}$ spectrum is compared to the experimental data. One can see the simulation agrees with the data. Therefore, the $Q_{2p} = 1.4$ MeV derived from peak "A" can be explained by the energy difference between the 2.9 MeV e.s. of ^{30}Ar and the 1.51 MeV e.s. of ^{28}S. The decay energies of 0.6 MeV and 0.8 MeV shown by the two peaks in Figure 6.4(a) are also quantitatively interpreted by the sequential emission of protons from ^{30}Ar$^*(2^+)$ state via ^{29}Cl e.s. at 2.3 MeV. Unfortunately, the present experiment didn't detect the γ-ray which should be emitted by the de-excitation of ^{28}S e.s. at 1.51 MeV. Therefore, a future experiment which can measure the $^{28}\mathrm{S}+p+p+\gamma$ coincidences with $Q_{2p} = 1.4$ MeV and $E_\gamma = 1.51$ MeV may test this tentative assignment [126].

7.2.1 Indication on Fine Structure in 2*p* Decay of $^{30}\mathrm{Ar}^*(2^+)$ State

As seen in the previous subsection, both peak "A" and peak "C" come from the decay of the 2^+ state of ^{30}Ar at 2.9 MeV. The decay scenario of the 2.9 MeV state in ^{30}Ar can be seen in Figure 6.5. One may notice that it decays via two branches: 1*p* decay to the ^{29}Cl g.s. and to the first e.s. of ^{29}Cl. In the same situation, the first e.s of ^{29}Cl also has two decay channels. It can decay either to the g.s. or to the first e.s. of ^{28}S by 1*p* emission. The observation of two decay branches into the g.s. and first e.s. of ^{28}S from the decay of ^{30}Ar$^*(2^+)$ state via intermediate states of ^{29}Cl represents the first hint of the so-called fine structure in 2*p* decay [126], which is in analogy to the fine structure effect observed in 1*p* radioactivity [9]. As mentioned above, detection of a $^{28}\mathrm{S} + p + p + \gamma$ coincidence is critical to verify the fine structure in the 2*p* decay of the state of $^{30}\mathrm{Ar}^*(2^+)$.

7.3 Sequential Emission of Protons from Higher Excited States of ^{30}Ar

Concerning ^{30}Ar states above peak "C", we inspected the $\theta_{^{28}\mathrm{S\text{-}p}}$ distribution resulting from the decays of such states by imposing the respective arc ρ_θ gates on the ^{30}Ar 2*p*-decay events. In Figure 6.4(d1), the $\theta_{^{28}\mathrm{S\text{-}p}}$ spectrum derived from peak "D1" exhibits a triple-peak structure, while the middle peak and the right-most peak match the 1.8 MeV and 2.9 MeV states observed in ^{29}Cl, respectively. Therefore, a natural interpretation for the experimental $\theta_{^{28}\mathrm{S\text{-}p}}$ spectrum is the sequential proton emission of ^{30}Ar state "D1" via the above-mentioned two ^{29}Cl states. To test such an explanation, MC simulations were performed and the resulting $\theta_{^{28}\mathrm{S\text{-}p}}$ spectra were compared with the data displayed in Fig-

ure 7.6(a). There the dashed and dotted curves represent the simulations of the detector response to the 2p decay of the 3.9 MeV ^{30}Ar state via the ^{29}Cl resonances at 1.8 MeV and 2.9 MeV, respectively. The weighted sum of these two components is shown by the solid curve and the contributions of the 1.8 MeV and 2.9 MeV components are 60% and 40%, respectively. One can see that simulations with our hypothesis reproduce the data rather well. In a similar manner, we carefully analyzed the ^{28}S-p angular correlations from peak "D2" shown in Figure 6.1. It was found that this ^{30}Ar state decays by sequential 2p emission via ^{29}Cl states at 2.3 MeV and 2.9 MeV, respectively. Corresponding MC simulations are shown in Figure 7.6(b) and they reproduce data well.

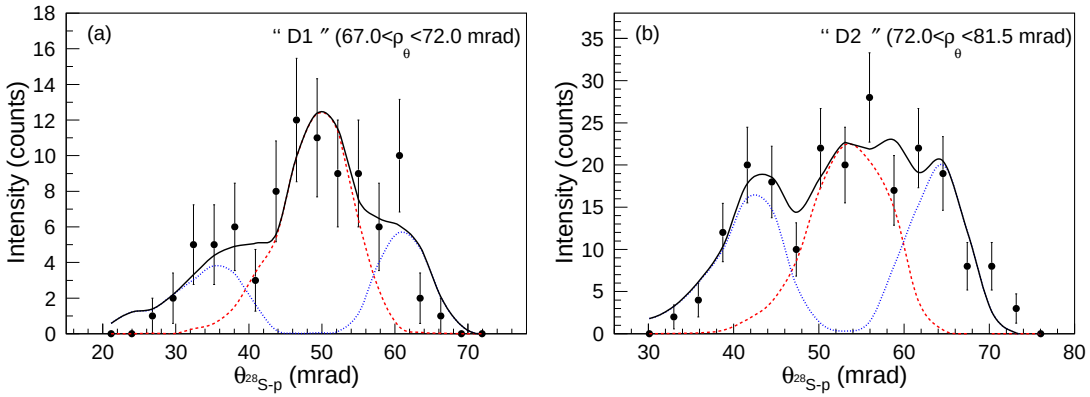

Figure 7.6: Angular $\theta_{^{28}\mathrm{S\text{-}p}}$ distributions derived from the decays of ^{30}Ar excited state at 3.9 MeV and at 4.2 MeV above the 2p threshold. (a) The data (black dots with statistical uncertainties) are selected from the $^{28}\mathrm{S}+p+p$ coincidences by using the ρ_θ gate "D1" at $67.0 < \rho_\theta < 72.0$ mrad. The solid curve displays the simulation of the sequential 2p decay of the ^{30}Ar state at 3.9 MeV via the ^{29}Cl resonance at 1.8 MeV (dashed curve) and the 2.9 MeV state (dotted curve). (b) The 2p decays selected by the ρ_θ gate "D2", $72.0 < \rho_\theta < 81.5$ mrad. The solid curve is the simulation of the sequential 2p decay of ^{30}Ar state at 4.2 MeV state via the 2.3 MeV (dashed curve) and the 2.9 MeV (dotted curve) levels in ^{29}Cl.

Regarding other observed excited states of ^{30}Ar, namely, peak "E", peak "F1", peak "F2", and peak "G" shown in Figure 6.1, it is tentatively suggested that all these e.s. decay by sequential emission of protons via intermediate resonances of ^{29}Cl. Corresponding MC simulations of the detector response to the 2p decays from these states were performed. Figure 7.7 shows a comparison between the simulated $\theta_{^{28}\mathrm{S\text{-}p}}$ spectra and the respective experimental distributions. One can see that all simulations generally agree with the data.

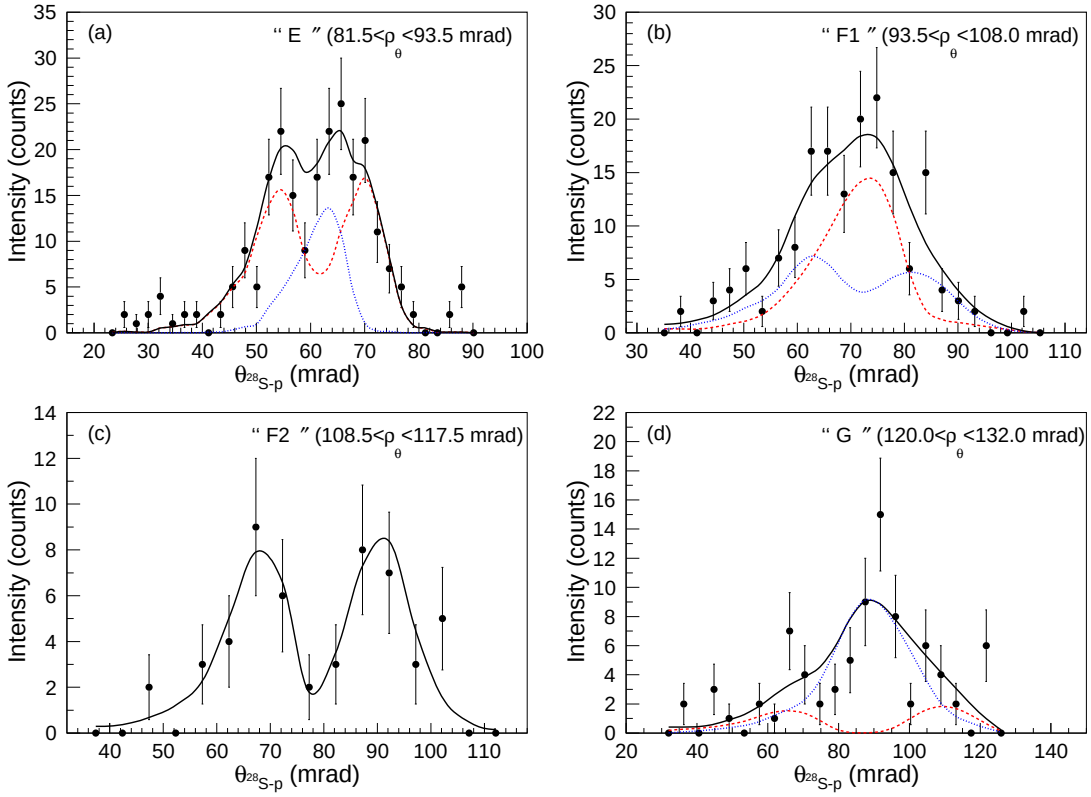

Figure 7.7: Angular $\theta_{^{28}\mathrm{S\text{-}p}}$ distributions derived from the decays of several excited states in ^{30}Ar. (a) The 2p decays selected by the ρ_θ gate "E", $81.5 < \rho_\theta < 93.5$ mrad. The simulation of the sequential 2p emission of the ^{30}Ar e.s at 5.6 MeV via the 3.5 MeV (dashed curve) and the 2.9 MeV (dotted curve) states in ^{29}Cl is depicted by the solid curve. (b) The 2p decay of e.s. in ^{30}Ar selected by the ρ_θ gate "F1", $93.5 < \rho_\theta < 108.0$ mrad. The dashed and dotted curves are the $\theta_{^{28}\mathrm{S\text{-}p}}$ distributions obtained by simulations of 2p emission of the ^{30}Ar state at 7.9 MeV via two ^{29}Cl states at 3.9 MeV and 2.9 MeV, respectively. The solid curve represents the sum fit. (c) The data obtained by imposing the ρ_θ gate "F2", $108.0 < \rho_\theta < 117.5$ mrad. The solid curve displays the $\theta_{^{28}\mathrm{S\text{-}p}}$ spectrum obtained from the simulation of sequential ejection of two protons from the 9.4 MeV ^{30}Ar e.s. via the ^{29}Cl resonance at 3.5 MeV. (d) The 2p decays selected by the ρ_θ gate "G", $120.0 < \rho_\theta < 132.0$ mrad. The solid curve shows the simulation of sequential 2p emission of the ^{30}Ar e.s. at 12.6 MeV via the ^{29}Cl states at 3.5 MeV (dashed curve) and 5.3 MeV (dotted curve), respectively.

8 Summary

As a recently-discovered exotic nuclear-decay mode, two-proton radioactivity provides a novel and powerful tool for nuclear structure studies beyond the proton drip-line. In order to search the previously-unknown nuclide ^{30}Ar, which is a 2p-radioactivity candidate, an experiment based on the tracking technique was performed at the FRS of GSI Darmstadt. The main contents of the present thesis are based on the data analysis of this experiment. The main achievements are the identification of new proton-unbound nuclei ^{30}Ar and ^{29}Cl and the investigation of their decay properties.

In the experiment, the high-energy ^{36}Ar beam was used to produce the secondary ^{31}Ar beam. Then the ^{31}Ar fragments were selected and transported by the first half of the FRS, which was operated in an achromatic ion-optic mode with an Al wedge degrader placed at the first focal plane of the FRS. At the middle focal plane F2, the ^{31}Ar beam bombarded the secondary ^{9}Be target. Then the ^{30}Ar nuclei were produced via one-neutron knockout reactions in the secondary target and their in-flight 2p decay products were tracked by a silicon strip detector array. The second half of the FRS was tuned to transmit the desired 2p decay daughter nuclei (i.e., ^{28}S) down to the final focal plane F4. Particle identification for the heavy ions was achieved by combining the magnetic rigidity, time-of-flight and energy loss measurements.

Silicon strip detectors, which are responsible for the measurement of the trajectories of the decay fragments, play a key role in the tracking technique. In order to achieve the best-possible accuracy of position and angle measurements by SSDs, several calibration and alignment procedures were performed. First, the performance of SSDs was studied with cosmic rays. Based on the data taken from the calibration runs, the pedestal of every strip was determined. Second, following the general procedure of pedestal subtraction, gain correction, dead and noisy strips (strips give no signal or noisy signal) treatment, and common-mode noise subtraction, the signals recorded by the SSDs during the experiment were analyzed event by event. The clusters generated by the incident ^{31}Ar and ^{28}S ions were identified, and the detector responses to their hits were calibrated. Third, an offset alignment and a tilt correction were performed to correct the possible misalignment of SSDs. After the calibration and alignment, the protons were identified by registering their impact positions in several SSD's and requiring a "straight-line" trajectory. Then the identification of a 2p decay event was performed by searching the triple coincidence $\mathrm{HI} + p + p$. The 2p-decay vertices were reconstructed and the angles between the decay products were measured.

In order to check the overall performance of the experiment and to determine the angular and half-life resolutions as well as the detection efficiency, decays of the previously-known *sd*-shell 2*p* emitter ^{19}Mg were remeasured. Through the analysis of the ^{17}Ne-proton angular correlations which reflect the energy correlations, the ground-state and several known excited states of ^{19}Mg were observed. A quantitative interpretation of the measured ^{17}Ne-proton angular correlations was conducted by comparing data with Monte Carlo simulations of the detector response to the measured decays. The 2*p* radioactivity of ^{19}Mg ground state and the sequential 2*p* emission of several known ^{19}Mg excited states were confirmed. The decay energies of these known ^{19}Mg states deduced from the present work are consistent with previous data. Moreover, the evidence on a new ^{19}Mg excited state at $8.9^{+0.8}_{-0.7}$ MeV above the 2*p* threshold was found. The corresponding ^{17}Ne-proton angular correlations can be tentatively explained by sequential emission of protons via two unknown ^{18}Na resonances at $2.5^{+0.7}_{-0.3}$ MeV and $4.0^{+1.5}_{-0.6}$ MeV above the 1*p* threshold, respectively. The decay schemes concerning the ^{19}Mg and ^{18}Na were updated.

After the successful proof, the previously-unknown nuclei ^{30}Ar and ^{29}Cl were identified by tracking the $^{28}\mathrm{S}+p+p$ and $^{28}\mathrm{S}+p$ coincidences, respectively. Several states of these 2*p*-unbound nuclei were observed. By analyzing the ^{28}S-proton angular correlations, the energies of the observed states in ^{30}Ar and ^{29}Cl were deduced relative to the 2*p* and the 1*p* thresholds, respectively. The assigned ground state and first excited state of ^{29}Cl were found at $1.8^{+0.1}_{-0.1}$ MeV and $2.3^{+0.1}_{-0.1}$ MeV above the 1*p* threshold, respectively. It was found that the ^{30}Ar ground state is located at $2.45^{+0.05}_{-0.10}$ MeV above the 2*p* threshold. Due to a strong Thomas-Ehrman shift, the lowest states in ^{30}Ar and ^{29}Cl point to a violation of isobaric mirror symmetry in the structure of these unbound nuclei. Detailed theoretical calculations of the correlations between 2*p* decay products followed by the Monte Carlo simulations of the detector response to the 2*p* decay were performed in order to investigate the decay mechanism of the ^{30}Ar ground state. It was found that the decay mechanism of the ^{30}Ar ground state is in a transition region between simultaneous 2*p* decay and sequential emission of protons. Such an interplay between the true three-body and the sequential two-body decay mechanisms is the first-time observation in the decay of a nuclear ground state. The theoretical investigations of transition dynamics of ^{30}Ar ground state demonstrated a surprisingly strong sensitivity of the decay correlation patterns to the variation of general 2*p*-decay parameters, namely, the 2*p* decay energy of the ^{30}Ar ground state, the 1*p* decay energy of the ^{29}Cl ground state, and the 1*p* decay width of the ^{29}Cl ground state. The first excited state of ^{30}Ar was found to be at $2.9^{+0.3}_{-0.1}$ MeV above the 2*p* threshold. Its decay was interpreted by two branches of sequential emission of protons into both ground state and first excited state of ^{28}S via the lowest states of ^{29}Cl. This is the first hint on so-called fine structure in the 2*p* emission. By comparing the experimental ^{28}S-proton angular correlations with those resulting from

the Monte Carlo simulations of the detector response, other observed ^{30}Ar excited states were tentatively assigned to decay by sequential emission of protons via intermediate resonances in ^{29}Cl. On the basis of the obtained results, the decay schemes of the observed states in ^{30}Ar and ^{29}Cl were constructed.

9 Outlook

The present thesis reports the analysis of an experiment which was conducted at the FRS of GSI. Two proton-unbound nuclei ^{30}Ar and ^{29}Cl were observed by tracking their in-flight decay products. It is also worth mentioning that the implantation-decay method was also applied in the experiment. The β-delayed 3p-decay of the exotic nucleus ^{31}Ar was observed with the OTPC. A combination of both in-flight decay technique and implantation decay method in the same experiment is a promising achievement in the studies of the proton-rich exotic nuclei. New opportunities, to be realized especially at the future Superconducting FRagment Separator (Super-FRS) of the Facility for Antiproton and Ion Research (FAIR), are outlined here.

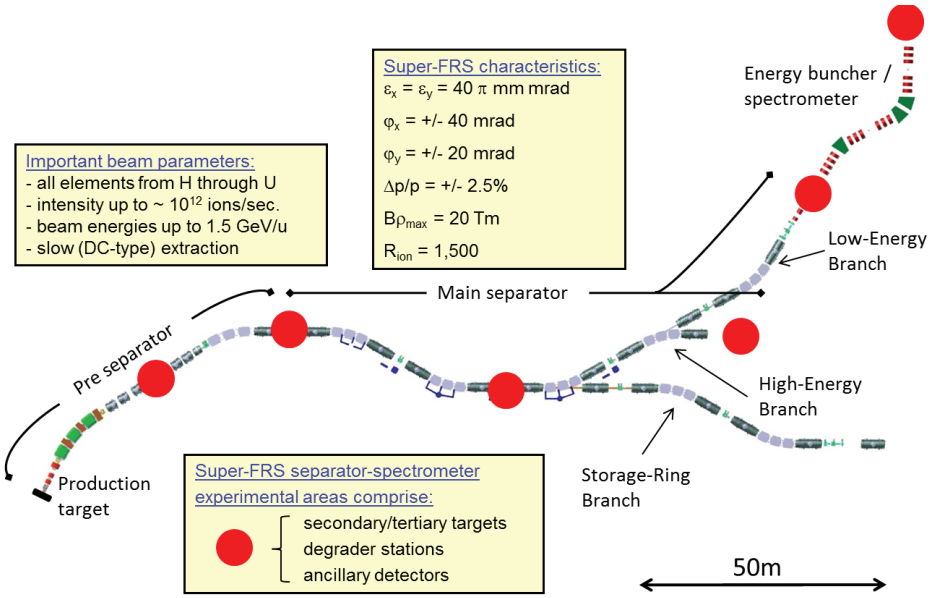

Figure 9.1: Layout of the Super-FRS together with its three separator branches: the Low-Energy Branch, the High-Energy Branch, and the Storage-Ring Branch. The spectrometer-energy-buncher system is also shown. The main characteristics and important beam parameters of the Super-FRS are listed in the boxes. ε_x and ε_y denote transverse beam emittances. φ_x and φ_y are angular acceptance. $\Delta p/p$ is the momentum acceptance. Bρ_{max} is the maximum magnetic rigidity. R$_{\mathrm{ion}}$ represents the resolving power. Figure taken from [136].

The results of the present work were obtained with relatively small number of decay events. The limited statistics has posed a challenge to the data analysis. An improved

statistics may help to further reduce the experimental uncertainties. Moreover, a combined detection of both particles and γ-rays emitted by the precursor may provide more information on the decay channels. These options will be addressed in the future EXPERT project. "EXPERT" stands for "EXotic Particle Emission and Radioactivity by Tracking" aimed at studies of nuclear landscape beyond the proton and neutron drip-lines. It intends to push nuclear structure researches up to the limits of nuclear existence [137]. EXPERT is a program proposed to be conducted with the Super-FRS at FAIR.

FAIR is a world-unique facility which is currently under construction at Darmstadt, Germany. After completion of FAIR, this new facility will provide high-intensity radioactive ion beams ranging from hydrogen up to uranium over a large energy range. As one of the main setups of FAIR, the Super-FRS will be a powerful fragment separator and high-resolution spectrometer. It can be employed to produce exotic nuclides via projectile fragmentation, fission, and two-step reactions. The isotopes of interest can be separated in flight within several hundred nanoseconds and they can be transported to the large-scale detector systems which will be located at the exits of the different separator branches. Main features of the Super-FRS are summarized in Figure 9.1. These challenging performance parameters are achieved with a multi-stage magnetic system, comprising intermediate degrader stations. Specialized detector systems will be installed at different focal planes of the Super-FRS in order to achieve the full particle identification event-by-event. These detectors can also be used advantageously for high-resolution momentum measurements [136].

The excellent features provided by the Super-FRS are well suited for the EXPERT project. In the future EXPERT experiment, the Super-FRS will be used as a radioactive ion beam separator in its first half and a high-resolution spectrometer in its second half set for registering secondary-reaction fragments. The EXPERT instrumentation will be placed at different focal planes at the Super-FRS. Figure 9.2 shows the main detectors and experimental scenarios proposed by the EXPERT program. The important detectors are: radiation-hard silicon strip detectors (radiation-hard SSDs) for tracking of the secondary beam impinging on the secondary target, silicon micro-strip tracking detectors (μSi tracking) for determining the trajectories of in-flight products coming from decays, the NeuRad (Neutron Radioactivity) detector for measuring the angular correlations of neutrons with a charged fragment, the GADAST (GAmma-ray Detectors Around Secondary Target) array for the measurement of γ rays and light particles emitted instantaneously after secondary reaction, the OTPC (Optical Time Projection Chamber) for radioactivity studies by employing the implantation decay method. Moreover, the theoretical/simulation framework will be also developed [137].

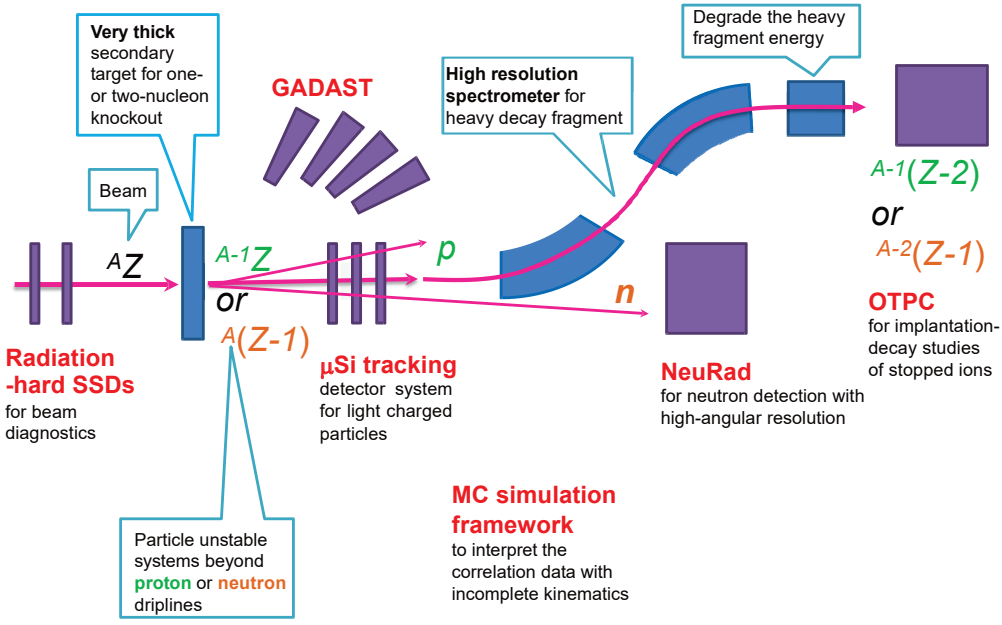

Figure 9.2: Schematic drawing of the proposed EXPERT experiments. The experimental scenario illustrated by the arrows suggests a population of two-proton (green color) or two-neutron (orange) precursor by one-nucleon knockout reaction. Figure based on [137].

Combining the Super-FRS together with the standard focal-plane detectors and the above-mentioned EXPERT detectors, the radioactive in-flight decays and continuum spectroscopy can be investigated. The phenomena of multi-nucleon radioactivity, resonance decays in continuum, β-delayed exotic decays and exotic excitation modes can be probed via observations of particle emission, including $2p$, $4p$, $6p$, n, $2n$, $4n$, $6n$ channels. Several EXPERT flagship cases, e.g., search for $2p$ radioactivity of ^{26}S and studying the ^{20}Si properties to search for $6p$ emission, have been considered. The proposed EXPERT setup covers two important lifetime ranges: of 100 ns - 1 s and of 1 ps - 100 ns by applying the implantation-decay and decay-in-flight techniques, respectively. For the short-lived systems, the resonance properties and information about continuum can be retrieved from the angular correlations between the decay products [137]. On the basis of the solid results achieved in the previous S271 and the present S388 experiment, the proposed EXPERT program will advance our understanding on the structure of nuclei along and beyond the drip-lines.

Bibliography

[1] R.F. Casten and B.M. Sherrill. The study of exotic nuclei. *Particle and Nuclear Physics*, 45(0):S171 – S233, 2000.

[2] S. Hofmann, W. Reisdorf, G. Münzenberg, F. P. Heßberger, J. R. H. Schneider, and P. Armbruster. Proton radioactivity of ^{151}Lu. *Zeitschrift für Physik A Atoms and Nuclei*, 305(2):111–123.

[3] O. Klepper, T. Batsch, S. Hofmann, R. Kirchner, W. Kurcewicz, W. Reisdorf, E. Roeckl, D. Schardt, and G. Nyman. Direct and beta-delayed proton decay of very neutron-deficient rare-earth isotopes produced in the reaction ^{58}Ni+^{92}Mo. *Zeitschrift für Physik A Atoms and Nuclei*, 305(2):125–130.

[4] M. Pfützner, E. Badura, C. Bingham, B. Blank, M. Chartier, H. Geissel, J. Giovinazzo, L.V. Grigorenko, R. Grzywacz, M. Hellström, Z. Janas, J. Kurcewicz, A.S. Lalleman, C. Mazzocchi, I. Mukha, G. Münzenberg, C. Plettner, E. Roeckl, K.P. Rykaczewski, K. Schmidt, R.S. Simon, M. Stanoiu, and J.-C. Thomas. First evidence for the two-proton decay of ^{45}Fe. *European Physical Journal A*, 14(3):279–285, 2002.

[5] J. Giovinazzo, B. Blank, M. Chartier, S. Czajkowski, A. Fleury, M. J. Lopez Jimenez, M. S. Pravikoff, J.-C. Thomas, F. de Oliveira Santos, M. Lewitowicz, V. Maslov, M. Stanoiu, R. Grzywacz, M. Pfützner, C. Borcea, and B. A. Brown. Two-proton radioactivity of ^{45}Fe. *Physical Review Letters*, 89:102501, 2002.

[6] V.I. Goldansky. On neutron-deficient isotopes of light nuclei and the phenomena of proton and two-proton radioactivity. *Nuclear Physics*, 19(0):482 – 495, 1960.

[7] Z. Kohley, T. Baumann, D. Bazin, G. Christian, P. A. DeYoung, J. E. Finck, N. Frank, M. Jones, E. Lunderberg, B. Luther, S. Mosby, T. Nagi, J. K. Smith, J. Snyder, A. Spyrou, and M. Thoennessen. Study of two-neutron radioactivity in the decay of ^{26}O. *Physical Review Letters*, 110:152501, 2013.

[8] Z. Kohley, T. Baumann, G. Christian, P. A. DeYoung, J. E. Finck, N. Frank, B. Luther, E. Lunderberg, M. Jones, S. Mosby, J. K. Smith, A. Spyrou, and M. Thoennessen. Three-body correlations in the ground-state decay of ^{26}O. *Physical Review C*, 91:034323, 2015.

[9] M. Pfützner, M. Karny, L. V. Grigorenko, and K. Riisager. Radioactive decays at limits of nuclear stability. *Reviews of Modern Physics*, 84:567–619, 2012.

[10] O.V. Bochkarev, L.V. Chulkov, A.A. Korsheninniicov, E.A. Kuz'min, I.G. Mukha, and G.B. Yankov. Democratic decay of ^{6}Be states. *Nuclear Physics A*, 505(2):215 – 240, 1989.

[11] B. Blank and M. Płoszajczak. Two-proton radioactivity. *Reports on Progress in Physics*, 71(4):046301, 2008.

[12] W. Whaling. Magnetic analysis of the $Li^6(He^3,t)Be^6$ reaction. *Physical Review*, 150:836–838, 1966.

[13] G. J. KeKelis, M. S. Zisman, D. K. Scott, R. Jahn, D. J. Vieira, Joseph Cerny, and F. Ajzenberg-Selove. Masses of the unbound nuclei ^{16}Ne, ^{15}F, and ^{12}O. *Physical Review C*, 17:1929–1938, 1978.

[14] R. A. Kryger, A. Azhari, M. Hellström, J. H. Kelley, T. Kubo, R. Pfaff, E. Ramakrishnan, B. M. Sherrill, M. Thoennessen, S. Yokoyama, R. J. Charity, J. Dempsey, A. Kirov, N. Robertson, D. G. Sarantites, L. G. Sobotka, and J. A. Winger. Two-proton emission from the ground state of ^{12}O. *Physical Review Letters*, 74:860–863, 1995.

[15] D. Suzuki, H. Iwasaki, D. Beaumel, L. Nalpas, E. Pollacco, M. Assié, H. Baba, Y. Blumenfeld, N. De Séréville, A. Drouart, S. Franchoo, A. Gillibert, J. Guillot, F. Hammache, N. Keeley, V. Lapoux, F. Maréchal, S. Michimasa, X. Mougeot, I. Mukha, H. Okamura, H. Otsu, A. Ramus, P. Roussel-Chomaz, H. Sakurai, J.-A. Scarpaci, O. Sorlin, I. Stefan, and M. Takechi. Breakdown of the $Z = 8$ shell closure in unbound ^{12}O and its mirror symmetry. *Physical Review Letters*, 103:152503, 2009.

[16] M. F. Jager, R. J. Charity, J. M. Elson, J. Manfredi, M. H. Mahzoon, L. G. Sobotka, M. McCleskey, R. G. Pizzone, B. T. Roeder, A. Spiridon, E. Simmons, L. Trache, and M. Kurokawa. Two-proton decay of ^{12}O and its isobaric analog state in ^{12}N. *Physical Review C*, 86:011304, 2012.

[17] C. J. Woodward, R. E. Tribble, and D. M. Tanner. Mass of ^{16}Ne. *Physical Review C*, 27:27–30, 1983.

[18] I. Mukha, L. Grigorenko, K. Sümmerer, L. Acosta, M. A. G. Alvarez, E. Casarejos, A. Chatillon, D. Cortina-Gil, J. M. Espino, A. Fomichev, J. E. García-Ramos, H. Geissel, J. Gómez-Camacho, J. Hofmann, O. Kiselev, A. Korsheninnikov,

N. Kurz, Yu. Litvinov, I. Martel, C. Nociforo, W. Ott, M. Pfützner, C. Rodríguez-Tajes, E. Roeckl, M. Stanoiu, H. Weick, and P. J. Woods. Proton-proton correlations observed in two-proton decay of ^{19}Mg and ^{16}Ne. *Physical Review C*, 77:061303, 2008.

[19] F. Wamers, J. Marganiec, F. Aksouh, Yu. Aksyutina, H. Álvarez-Pol, T. Aumann, S. Beceiro-Novo, K. Boretzky, M. J. G. Borge, M. Chartier, A. Chatillon, L. V. Chulkov, D. Cortina-Gil, H. Emling, O. Ershova, L. M. Fraile, H. O. U. Fynbo, D. Galaviz, H. Geissel, M. Heil, D. H. H. Hoffmann, H. T. Johansson, B. Jonson, C. Karagiannis, O. A. Kiselev, J. V. Kratz, R. Kulessa, N. Kurz, C. Langer, M. Lantz, T. Le Bleis, R. Lemmon, Yu. A. Litvinov, K. Mahata, C. Müntz, T. Nilsson, C. Nociforo, G. Nyman, W. Ott, V. Panin, S. Paschalis, A. Perea, R. Plag, R. Reifarth, A. Richter, C. Rodriguez-Tajes, D. Rossi, K. Riisager, D. Savran, G. Schrieder, H. Simon, J. Stroth, K. Sümmerer, O. Tengblad, H. Weick, C. Wimmer, and M. V. Zhukov. First observation of the unbound nucleus ^{15}Ne. *Physical Review Letters*, 112:132502, 2014.

[20] K. W. Brown, R. J. Charity, L. G. Sobotka, Z. Chajecki, L. V. Grigorenko, I. A. Egorova, Yu. L. Parfenova, M. V. Zhukov, S. Bedoor, W. W. Buhro, J. M. Elson, W. G. Lynch, J. Manfredi, D. G. McNeel, W. Reviol, R. Shane, R. H. Showalter, M. B. Tsang, J. R. Winkelbauer, and A. H. Wuosmaa. Observation of long-range three-body coulomb effects in the decay of ^{16}Ne. *Physical Review Letters*, 113:232501, 2014.

[21] I. Mukha, K. Sümmerer, L. Acosta, M. A. G. Alvarez, E. Casarejos, A. Chatillon, D. Cortina-Gil, J. Espino, A. Fomichev, J. E. García-Ramos, H. Geissel, J. Gómez-Camacho, L. Grigorenko, J. Hoffmann, O. Kiselev, A. Korsheninnikov, N. Kurz, Yu. Litvinov, I. Martel, C. Nociforo, W. Ott, M. Pfützner, C. Rodríguez-Tajes, E. Roeckl, M. Stanoiu, H. Weick, and P. J. Woods. Observation of two-proton radioactivity of ^{19}Mg by tracking the decay products. *Physical Review Letters*, 99:182501, 2007.

[22] P. Voss, T. Baumann, D. Bazin, A. Dewald, H. Iwasaki, D. Miller, A. Ratkiewicz, A. Spyrou, K. Starosta, M. Thoennessen, C. Vaman, and J. A. Tostevin. ^{19}Mg two-proton decay lifetime. *Physical Review C*, 90:014301, 2014.

[23] C. Dossat, A. Bey, B. Blank, G. Canchel, A. Fleury, J. Giovinazzo, I. Matea, F. de Oliveira Santos, G. Georgiev, S. Grévy, I. Stefan, J. C. Thomas, N. Adimi, C. Borcea, D. Cortina Gil, M. Caamano, M. Stanoiu, F. Aksouh, B. A. Brown, and L. V. Grigorenko. Two-proton radioactivity studies with ^{45}Fe and ^{48}Ni. *Physical Review C*, 72:054315, 2005.

[24] K. Miernik, W. Dominik, Z. Janas, M. Pfützner, L. Grigorenko, C. R. Bingham, H. Czyrkowski, M. Ćwiok, I. G. Darby, R. Dabrowski, T. Ginter, R. Grzywacz, M. Karny, A. Korgul, W. Kuśmierz, S. N. Liddick, M. Rajabali, K. Rykaczewski, and A. Stolz. Two-proton correlations in the decay of ^{45}Fe. *Physical Review Letters*, 99:192501, 2007.

[25] M. Pomorski, M. Pfützner, W. Dominik, R. Grzywacz, T. Baumann, J. S. Berryman, H. Czyrkowski, R. Dabrowski, T. Ginter, J. Johnson, G. Kamiński, A. Kuźniak, N. Larson, S. N. Liddick, M. Madurga, C. Mazzocchi, S. Mianowski, K. Miernik, D. Miller, S. Paulauskas, J. Pereira, K. P. Rykaczewski, A. Stolz, and S. Suchyta. First observation of two-proton radioactivity in ^{48}Ni. *Physical Review C*, 83:061303, 2011.

[26] B. Blank, A. Bey, G. Canchel, C. Dossat, A. Fleury, J. Giovinazzo, I. Matea, N. Adimi, F. De Oliveira, I. Stefan, G. Georgiev, S. Grévy, J. C. Thomas, C. Borcea, D. Cortina, M. Caamano, M. Stanoiu, F. Aksouh, B. A. Brown, F. C. Barker, and W. A. Richter. First observation of ^{54}Zn and its decay by two-proton emission. *Physical Review Letters*, 94:232501, 2005.

[27] P. Ascher, L. Audirac, N. Adimi, B. Blank, C. Borcea, B. A. Brown, I. Companis, F. Delalee, C. E. Demonchy, F. de Oliveira Santos, J. Giovinazzo, S. Grévy, L. V. Grigorenko, T. Kurtukian-Nieto, S. Leblanc, J.-L. Pedroza, L. Perrot, J. Pibernat, L. Serani, P. C. Srivastava, and J.-C. Thomas. Direct observation of two protons in the decay of ^{54}Zn. *Physical Review Letters*, 107:102502, 2011.

[28] D. F. Geesaman, R. L. McGrath, P. M. S. Lesser, P. P. Urone, and B. VerWest. Particle decay of ^{6}Be. *Physical Review C*, 15:1835–1838, 1977.

[29] O. V. Bochkarev, A. A Korsheninnikov, E. A. Kuz'min, I. G. Mukha, A. A Ogloblin, L. V. Chulkov, and Yan'kov. G. B. Two-proton decay of ^{6}Be. *JETP Letters*, 40:969, 1984.

[30] L.V. Grigorenko, T.D. Wiser, K. Miernik, R.J. Charity, M. Pfützner, A. Banu, C.R. Bingham, M. Ćwiok, I.G. Darby, W. Dominik, J.M. Elson, T. Ginter, R. Grzywacz, Z. Janas, M. Karny, A. Korgul, S.N. Liddick, K. Mercurio, M. Rajabali, K. Rykaczewski, R. Shane, L.G. Sobotka, A. Stolz, L. Trache, R.E. Tribble, A.H. Wuosmaa, and M.V. Zhukov. Complete correlation studies of two-proton decays: ^{6}Be and ^{45}Fe. *Physics Letters B*, 677(1 – 2):30 – 35, 2009.

[31] I. A. Egorova, R. J. Charity, L. V. Grigorenko, Z. Chajecki, D. Coupland, J. M. Elson, T. K. Ghosh, M. E. Howard, H. Iwasaki, M. Kilburn, Jenny Lee, W. G. Lynch, J. Manfredi, S. T. Marley, A. Sanetullaev, R. Shane, D. V. Shetty, L. G. Sobotka, M. B. Tsang, J. Winkelbauer, A. H. Wuosmaa, M. Youngs, and M. V.

Zhukov. Democratic decay of ^{6}Be exposed by correlations. *Physical Review Letters*, 109:202502, 2012.

[32] L. V. Grigorenko, R. C. Johnson, I. G. Mukha, I. J. Thompson, and M. V. Zhukov. Theory of two-proton radioactivity with application to ^{19}Mg and ^{48}Ni. *Physical Review Letters*, 85:22–25, 2000.

[33] L. V. Grigorenko, I. G. Mukha, I. J. Thompson, and M. V. Zhukov. Two-proton widths of ^{12}O, ^{16}Ne, and three-body mechanism of thomas-ehrman shift. *Physical Review Letters*, 88:042502, 2002.

[34] A.S. Fomichev, V. Chudoba, I.A. Egorova, S.N. Ershov, M.S. Golovkov, A.V. Gorshkov, V.A. Gorshkov, L.V. Grigorenko, G. Kamiński, S.A. Krupko, I.G. Mukha, Yu.L. Parfenova, S.I. Sidorchuk, R.S. Slepnev, L. Standyło, S.V. Stepantsov, G.M. Ter-Akopian, R. Wolski, and M.V. Zhukov. Isovector soft dipole mode in ^{6}Be. *Physics Letters B*, 708(1 – 2):6 – 13, 2012.

[35] L. Axelsson, M. J. G. Borge, S. Fayans, V. Z. Goldberg, S. Grévy, D. Guillemaud-Mueller, B. Jonson, K. M. Källman, T. Lönnroth, M. Lewitowicz, P. Manngård, K. Markenroth, I. Martel, A. C. Mueller, I. Mukha, T. Nilsson, G. Nyman, N. A. Orr, K. Riisager, G. V. Rogatchev, M. G. Saint-Laurent, I. N. Serikov, O. Sorlin, O. Tengblad, F. Wenander, J. S. Winfield, and R. Wolski. Study of the unbound nucleus ^{11}N by elastic resonance scattering. *Physical Review C*, 54:R1511–R1514, 1996.

[36] A. Lépine-Szily, J. M. Oliveira, A. N. Ostrowski, H. G. Bohlen, R. Lichtenthaler, A. Blazevic, C. Borcea, V. Guimarães, R. Kalpakchieva, V. Lapoux, M. MacCormick, F. Oliveira, W. von Oertzen, N. A. Orr, P. Roussel-Chomaz, Th. Stolla, and J. S. Winfield. Spectroscopy of the unbound nucleus ^{11}N by the ^{12}C(^{14}N,^{15} C)^{11}N transfer reaction. *Physical Review Letters*, 80:1601–1604, 1998.

[37] A. Azhari, T. Baumann, J. A. Brown, M. Hellström, J. H. Kelley, R. A. Kryger, D. J. Millener, H. Madani, E. Ramakrishnan, D. E. Russ, T. Suomijarvi, M. Thoennessen, and S. Yokoyama. Proton decay of states in ^{11}N. *Physical Review C*, 57:628–631, 1998.

[38] A. Azhari, R. A. Kryger, and M. Thoennessen. Decay of the ^{12}O ground state. *Physical Review C*, 58:2568–2570, 1998.

[39] K. Mercurio, R. J. Charity, R. Shane, L. G. Sobotka, J. M. Elson, M. Famiano, A. H. Wuosmaa, A. Banu, C. Fu, L. Trache, R. E. Tribble, and A. M. Mukhamedzhanov. Correlated two-proton decay from ^{10}C. *Physical Review C*, 78:031602, 2008.

[40] C.R. Bain, P.J. Woods, R. Coszach, T. Davinson, P. Decrock, M. Gaelens, W. Galster, M. Huyse, R.J. Irvine, P. Leleux, E. Lienard, M. Loiselet, C. Michotte, R. Neal, A. Ninane, G. Ryckewaert, A.C. Shotter, G. Vancraeynest, J. Vervier, and J. Wauters. Two proton emission induced via a resonance reaction. *Phys. Lett. B*, 373(1 – 3):35 – 39, 1996.

[41] K. W. Brown, R. J. Charity, L. G. Sobotka, L. V. Grigorenko, T. A. Golubkova, S. Bedoor, W. W. Buhro, Z. Chajecki, J. M. Elson, W. G. Lynch, J. Manfredi, D. G. McNeel, W. Reviol, R. Shane, R. H. Showalter, M. B. Tsang, J. R. Winkelbauer, and A. H. Wuosmaa. Interplay between sequential and prompt two-proton decay from the first excited state of ^{16}Ne. *Physical Review C*, 92:034329, 2015.

[42] M. J. Chromik, P. G. Thirolf, M. Thoennessen, B. A. Brown, T. Davinson, D. Gassmann, P. Heckman, J. Prisciandaro, P. Reiter, E. Tryggestad, and P. J. Woods. Two-proton spectroscopy of low-lying states in ^{17}Ne. *Physical Review C*, 66:024313, 2002.

[43] J. Gómez del Campo, A. Galindo-Uribarri, J. R. Beene, C. J. Gross, J. F. Liang, M. L. Halbert, D. W. Stracener, D. Shapira, R. L. Varner, E. Chavez-Lomeli, and M. E. Ortiz. Decay of a resonance in ^{18}Ne by the simultaneous emission of two protons. *Physical Review Letters*, 86:43–46, 2001.

[44] G. Raciti, G. Cardella, M. De Napoli, E. Rapisarda, F. Amorini, and C. Sfienti. Experimental evidence of ^{2}He decay from ^{18}Ne excited states. *Physical Review Letters*, 100:192503, 2008.

[45] F. de Oliveira Santos, P. Himpe, M. Lewitowicz, I. Stefan, N. Smirnova, N.L. Achouri, J.C. Angélique, C. Angulo, L. Axelsson1, D. Baiborodin, F. Becker, M. Bellegui, E. Berthoumieux, B. Blank1, C. Borcea, A. Cassimi, J.M. Daugas, G. de France, F. Dembinski, C.E. Demonchy, Z. Dlouhy, P. Dolégiéviez, C. Donzaud, G. Georgiev, L. Giot, S. Grévy, D. Guillemaud Mueller, V. Lapoux, E. Liénard, M.J. Lopez Jimenez, K. Markenroth, I. Matea, W. Mittig, F. Negoita, G. Neyens, N. Orr, F. Pougheon, P. Roussel Chomaz, M.G. Saint Laurent, F. Sarazin, H. Savajols, M. Sawicka, O. Sorlin, M. Stanoiu, C. Stode, G. Thiamova, D. Verney, , and A.C.C. Villari. Study of ^{19}Na at spiral. *European Physical Journal A*, 24:237–247, 2005.

[46] C. J. Lin, X. X. Xu, H. M. Jia, F. Yang, F. Jia, S. T. Zhang, Z. H. Liu, H. Q. Zhang, H. S. Xu, Z. Y. Sun, J. S. Wang, Z. G. Hu, M. Wang, R. F. Chen, X. Y. Zhang, C. Li, X. G. Lei, Z. G. Xu, G. Q. Xiao, and W. L. Zhan. Experimental study of two-proton correlated emission from ^{29}S excited states. *Physical Review C*, 80:014310, 2009.

[47] I. Mukha, E. Roeckl, L. Batist, A. Blazhev, J. Döring, H. Grawe, L. Grigorenko, M. Huyse, Z. Janas, R. Kirchner, M. La Commara, C. Mazzocchi, Sam L. Tabor, and P. Van Duppen. Proton-proton correlations observed in two-proton radioactivity of ^{94}Ag. *Nature*, 439:298–302, 2006.

[48] O. L. Pechenaya, C. J. Chiara, D. G. Sarantites, W. Reviol, R. J. Charity, M. P. Carpenter, R. V. F. Janssens, T. Lauritsen, C. J. Lister, D. Seweryniak, S. Zhu, L.-L. Andersson, E. K. Johansson, and D. Rudolph. Level structure of $^{92}\mathrm{Rh}$: Implications for the two-proton decay of $^{94}\mathrm{Ag}^{m}$. *Physical Review C*, 76:011304, 2007.

[49] A. Kankainen, V.-V. Elomaa, L. Batist, S. Eliseev, T. Eronen, U. Hager, J. Hakala, A. Jokinen, I. D. Moore, Yu. N. Novikov, H. Penttilä, A. Popov, S. Rahaman, S. Rinta-Antila, J. Rissanen, A. Saastamoinen, D. M. Seliverstov, T. Sonoda, G. Vorobjev, C. Weber, and J. Äystö. Mass measurements and implications for the energy of the high-spin isomer in $^{94}\mathrm{Ag}$. *Physical Review Letters*, 101:142503, 2008.

[50] I. Mukha, H. Grawe, E. Roeckl, and S. Tabor. Comment on "level structure of ^{92}Rh: Implications for the two-proton decay of $^{94}\mathrm{Ag}^{m}$". *Physical Review C*, 78:039803, 2008.

[51] J. Cerny, D. M. Moltz, D. W. Lee, K. Peräjärvi, B. R. Barquest, L. E. Grossman, W. Jeong, and C. C. Jewett. Reinvestigation of the direct two-proton decay of the long-lived isomer $^{94}\mathrm{Ag}^{m}$ [0.4 s, 6.7 MeV, $(21+)$]. *Physical Review Letters*, 103:152502, 2009.

[52] David G. Jenkins. Reviewing the evidence for two-proton emission from the high-spin isomer in $^{94}\mathrm{Ag}$. *Physical Review C*, 80:054303, 2009.

[53] R. J. Charity, J. M. Elson, J. Manfredi, R. Shane, L. G. Sobotka, Z. Chajecki, D. Coupland, H. Iwasaki, M. Kilburn, Jenny Lee, W. G. Lynch, A. Sanetullaev, M. B. Tsang, J. Winkelbauer, M. Youngs, S. T. Marley, D. V. Shetty, A. H. Wuosmaa, T. K. Ghosh, and M. E. Howard. $2p$-$2p$ decay of $^{8}\mathbf{C}$ and isospin-allowed $2p$ decay of the isobaric-analog state in $^{8}\mathbf{B}$. *Physical Review C*, 82:041304, 2010.

[54] K. W. Brown, W. W. Buhro, R. J. Charity, J. M. Elson, W. Reviol, L. G. Sobotka, Z. Chajecki, W. G. Lynch, J. Manfredi, R. Shane, R. H. Showalter, M. B. Tsang, D. Weisshaar, J. R. Winkelbauer, S. Bedoor, and A. H. Wuosmaa. Two-proton decay from the isobaric analog state in $^{8}\mathrm{B}$. *Physical Review C*, 90:027304, 2014.

[55] J. Giovinazzo, B. Blank, C. Borcea, G. Canchel, J.-C. Dalouzy, C. E. Demonchy, F. de Oliveira Santos, C. Dossat, S. Grévy, L. Hay, J. Huikari, S. Leblanc,

I. Matea, J.-L. Pedroza, L. Perrot, J. Pibernat, L. Serani, C. Stodel, and J.-C. Thomas. First direct observation of two protons in the decay of ^{45}Fe with a time-projection chamber. *Physical Review Letters*, 99:102501, 2007.

[56] K. Miernik, W. Dominik, H. Czyrkowski, R. Dabrowski, A. Fomitchev, M. Golovkov, Z. Janas, W. Kuśmierz, M. Pfützner, A. Rodin, S. Stepantsov, R. Slepniev, G.M. Ter-Akopian, and R. Wolski. Optical time projection chamber for imaging nuclear decays. *Nuclear Instruments and Methods in Physics Research Section A*, 581(1 ‐ 2):194 – 197, 2007.

[57] B. Blank, P. Ascher, L. Audirac, G. Canchel, J. Giovinazzo, T. Kurtukian-Nieto, F. de Oliveira Santos, S. Grévy, J.-C. Thomas, C. Borcea, and L.V. Grigorenko. Two-proton radioactivity as a tool of nuclear structure studies. *Acta Physica Polonica B*, 42:545–553, 2011.

[58] I. Mukha, L. Grigorenko, L. Acosta, M. A. G. Alvarez, E. Casarejos, A. Chatillon, D. Cortina-Gil, J. M. Espino, A. Fomichev, J. E. García-Ramos, H. Geissel, J. Gómez-Camacho, J. Hofmann, O. Kiselev, A. Korsheninnikov, N. Kurz, Yu. A. Litvinov, I. Martel, C. Nociforo, W. Ott, M. Pfützner, C. Rodríguez-Tajes, E. Roeckl, C. Scheidenberger, M. Stanoiu, K. Sümmerer, H. Weick, and P. J. Woods. New states in ^{18}Na and ^{19}Mg observed in the two-proton decay of ^{19}Mg. *Physical Review C*, 85:044325, 2012.

[59] M. Pomorski, M. Pfützner, W. Dominik, R. Grzywacz, A. Stolz, T. Baumann, J. S. Berryman, H. Czyrkowski, R. Dabrowski, A. Fijałkowska, T. Ginter, J. Johnson, G. Kamiński, N. Larson, S. N. Liddick, M. Madurga, C. Mazzocchi, S. Mianowski, K. Miernik, D. Miller, S. Paulauskas, J. Pereira, K. P. Rykaczewski, and S. Suchyta. Proton spectroscopy of ^{48}Ni,^{46} Fe, and ^{44}Cr. *Physical Review C*, 90:014311, 2014.

[60] V.I. Goldansky. Two-proton radioactivity. *Nuclear Physics*, 27:648 – 664, 1961.

[61] B. Alex Brown. Diproton decay of nuclei on the proton drip line. *Physical Review C*, 43:R1513–R1517, 1991.

[62] W. Nazarewicz, J. Dobaczewski, T. R. Werner, J. A. Maruhn, P.-G. Reinhard, K. Rutz, C. R. Chinn, A. S. Umar, and M. R. Strayer. Structure of proton drip-line nuclei around doubly magic ^{48}Ni. *Physical Review C*, 53:740–751, 1996.

[63] W. E. Ormand. Mapping the proton drip line up to A$=70$. *Physical Review C*, 55:2407–2417, 1997.

[64] L. V. Grigorenko, R. C. Johnson, I. G. Mukha, I. J. Thompson, and M. V. Zhukov. Two-proton radioactivity and three-body decay: General problems and theoretical approach. *Physical Review C*, 64:054002, 2001.

[65] L. V. Grigorenko and M. V. Zhukov. Two-proton radioactivity and three-body decay. iii. integral formulas for decay widths in a simplified semianalytical approach. *Physical Review C*, 76:014008, 2007.

[66] F. C. Barker. Width of the ^{12}O ground state. *Physical Review C*, 59:535–538, 1999.

[67] F. C. Barker. ^{12}O ground-state decay by ^{2}He emission. *Physical Review C*, 63:047303, 2001.

[68] I. Mukha, K. Sümmerer, L. Acosta, M. A. G. Alvarez, E. Casarejos, A. Chatillon, D. Cortina-Gil, I. A. Egorova, J. M. Espino, A. Fomichev, J. E. García-Ramos, H. Geissel, J. Gómez-Camacho, L. Grigorenko, J. Hofmann, O. Kiselev, A. Korsheninnikov, N. Kurz, Yu. A. Litvinov, E. Litvinova, I. Martel, C. Nociforo, W. Ott, M. Pfützner, C. Rodríguez-Tajes, E. Roeckl, M. Stanoiu, N. K. Timofeyuk, H. Weick, and P. J. Woods. Spectroscopy of proton-unbound nuclei by tracking their decay products in-flight: One- and two- proton decays of ^{15}F, ^{16}Ne, and ^{19}Na. *Physical Review C*, 82:054315, 2010.

[69] K. Bennaceur, J. Dobaczewski, and M. Płoszajczak. Continuum effects for the mean-field and pairing properties of weakly bound nuclei. *Physical Review C*, 60:034308, 1999.

[70] J. Rotureau, J. Okołowicz, and M. Płoszajczak. Microscopic theory of the two-proton radioactivity. *Physical Review Letters*, 95:042503, 2005.

[71] D. Singh and G. Saxena. Study of two-proton radioactivity within the relativistic mean-field plus bcs approach. *International Journal of Modern Physics E*, 21(09):1250076, 2012.

[72] Qiang Zhao, Jian Min Dong, Jun Ling Song, and Wen Hui Long. Proton radioactivity described by covariant density functional theory with the similarity renormalization group method. *Phys. Rev. C*, 90:054326, 2014.

[73] Yeunhwan Lim, Xuewei Xia, and Youngman Kim. Proton radioactivity in relativistic continuum hartree-bogoliubov theory. *Phys. Rev. C*, 93:014314, 2016.

[74] Takahito Maruyama, Tomohiro Oishi, Kouichi Hagino, and Hiroyuki Sagawa. Time-dependent approach to many-particle tunneling in one dimension. *Physical Review C*, 86:044301, 2012.

[75] D. S. Delion, R. J. Liotta, and R. Wyss. Simple approach to two-proton emission. *Physical Review C*, 87:034328, 2013.

[76] H. T. Fortune. Width of ^{16}Ne(g.s.). *Physical Review C*, 90:024323, 2014.

[77] H. T. Fortune and R. Sherr. Two-proton decay energy and width of ^{19}Mg(g.s.). *Physical Review C*, 76:014313, 2007.

[78] H. T. Fortune and R. Sherr. Update on energy and width of ^{19}Mg(g.s.). *Physical Review C*, 83:057301, 2011.

[79] H. T. Fortune and R. Sherr. Reexamining ^{18}Na and ^{19}Mg. *Physical Review C*, 85:051302, 2012.

[80] Joachim Jänecke. The emission of protons from light neutron-deficient nuclei. *Nuclear Physics*, 61(2):326 – 341, 1965.

[81] V.I. Goldansky. Two-proton radioactivity (prospects of detection and study). *Soviet Physics Uspekhi*, 8:770 – 779, 1966.

[82] L. V. Grigorenko and M. V. Zhukov. Two-proton radioactivity and three-body decay. ii. exploratory studies of lifetimes and correlations. *Physical Review C*, 68:054005, 2003.

[83] E. Olsen, M. Pfützner, N. Birge, M. Brown, W. Nazarewicz, and A. Perhac. Landscape of two-proton radioactivity. *Physical Review Letters*, 110:222501, 2013.

[84] B. Blank, L. Audirac, G. Canchel, F. Delalee, C.E. Demonchy, J. Giovinazzo, L. Hay, P. Hellmuth, J. Huikari, S. Leblanc, S. List, C. Marchand, I. Matea, J.-L. Pedroza, J. Pibernat, A. Rebii, L. Serani, F. de Oliveira Santos, S. Grévy, L. Perrot, C. Stodel, J.C. Thomas, C. Borcea, C. Dossat, and R. de Oliveira. A time projection chamber to study two-proton radioactivity. *Nuclear Instruments and Methods in Physics Research Section B*, 266(19 – 20):4606 – 4611, 2008.

[85] I. Mukha and G. Schrieder. Two-proton radioactivity as a genuine three-body decay: The ^{19}Mg probe. *Nuclear Physics A*, 690(1 – 3):280 – 283, 2001.

[86] I. Mukha. Two-proton radioactivity search. *Physics of Atomic Nuclei*, 66(8):1519 – 1522, 2003.

[87] E. Byckling and K. Kajantie. *Particle Kinematics*. Wiley, New York, 1973.

[88] L. V. Grigorenko and M. V. Zhukov. Two-proton radioactivity and three-body decay. iv. connection to quasiclassical formulation. *Physical Review C*, 76:014009, 2007.

[89] M.V. Zhukov, B.V. Danilin, D.V. Fedorov, J.M. Bang, I.J. Thompson, and J.S. Vaagen. Bound state properties of borromean halo nuclei: ^{6}He and ^{11}Li. *Physics Reports*, 231(4):151 – 199, 1993.

[90] L. V. Grigorenko, T. D. Wiser, K. Mercurio, R. J. Charity, R. Shane, L. G. Sobotka, J. M. Elson, A. H. Wuosmaa, A. Banu, M. McCleskey, L. Trache, R. E. Tribble, and M. V. Zhukov. Three-body decay of ^{6}Be. *Phys. Rev. C*, 80:034602, 2009.

[91] L. V. Grigorenko, T. A. Golubkova, and M. V. Zhukov. Thomas-ehrman effect in a three-body model: The ^{16}Ne case. *Physical Review C*, 91:024325, 2015.

[92] L.V. Grigorenko, I.G. Mukha, and M.V. Zhukov. Prospective candidates for the two-proton decay studies i: structure and coulomb energies of ^{17}Ne and ^{19}Mg. *Nuclear Physics A*, 713(3 – 4):372 – 389, 2003.

[93] L.V Grigorenko, I.G Mukha, and M.V Zhukov. Erratum to: "prospective candidates for the two-proton decay studies i: structure and coulomb energies of ^{17}Ne and ^{19}Mg" [nucl. phys. a 713 (2003) 372]. *Nuclear Physics A*, 740(3 – 4):401 – 402, 2004.

[94] L.V. Grigorenko, I.G. Mukha, and M.V. Zhukov. Prospective candidates for the two-proton decay studies. (ii) exploratory studies of ^{30}Ar, ^{34}Ca, and ^{45}Fe. *Nuclear Physics A*, 714(3 – 4):425 – 440, 2003.

[95] I. Mukha, N. K. Timofeyuk, K. Sümmerer, L. Acosta, M. A. G. Alvarez, E. Casarejos, A. Chatillon, D. Cortina-Gil, J. M. Espino, A. Fomichev, J. E. García-Ramos, H. Geissel, J. Gómez-Camacho, L. Grigorenko, J. Hofmann, O. Kiselev, A. Korsheninnikov, N. Kurz, Yu. Litvinov, I. Martel, C. Nociforo, W. Ott, M. Pfützner, C. Rodríguez-Tajes, E. Roeckl, M. Stanoiu, H. Weick, and P. J. Woods. Observation of narrow states in nuclei beyond the proton drip line: ^{15}F and ^{16}Ne. *Physical Review C*, 79:061301, 2009.

[96] L. V. Grigorenko and M. V. Zhukov. Three-body resonant radiative capture reactions in astrophysics. *Physical Review C*, 72:015803, 2005.

[97] Joachim Görres, Michael Wiescher, and Friedrich-Karl Thielemann. Bridging the waiting points: The role of two-proton capture reactions in the *rp* process. *Physical Review C*, 51:392–400, 1995.

[98] L.V. Grigorenko, K. Langanke, N.B. Shul'gina, and M.V. Zhukov. Soft dipole mode in ^{17}Ne and the astrophysical 2*p* capture on ^{15}O. *Physics Letters B*, 641(3 – 4):254 – 259, 2006.

[99] M. Steiner, K. Blasche, H.-G. Clerc, H. Eickhoff, B. Franczak, H. Geissel, G. Münzenberg, K.-H. Schmidt, H. Stelzer, and K. Sümmerer. Preliminary measurements of SIS 18 beam parameters. *Nuclear Instruments and Methods in Physics Research Section A: Accelerators, Spectrometers, Detectors and Associated Equipment*, 312(3):420 – 424, 1992.

[100] H. Geissel, P. Armbruster, K. H. Behr, A. Brünle, K. Burkard, M. Chen, H. Folger, B. Franczak, H. Keller, O. Klepper, B. Langenbeck, F. Nickel, E. Pfeng, M. Pfützner, E. Roeckl, K. Rykaczewski, I. Schall, D. Schardt, C. Scheidenberger, K.-H. Schmidt, A. Schröter, T. Schwab, K. Sümmerer, M. Weber, G. Münzenberg, T. Brohm, H.-G. Clerc, M. Fauerbach, J.-J. Gaimard, A. Grewe, E. Hanelt, B. Knödler, M. Steiner, B. Voss, J. Weckenmann, C. Ziegler, A. Magel, H. Wollnik, J.P. Dufour, Y. Fujita, D.J. Vieira, and B. Sherrill. The GSI projectile fragment separator (frs): a versatile magnetic system for relativistic heavy ions. *Nuclear Instruments and Methods in Physics Research Section B*, 70(1 – 4):286 – 297, 1992.

[101] Bernhard Franzke. The heavy ion storage and cooler ring project ESR at GSI. *Nuclear Instruments and Methods in Physics Research Section B: Beam Interactions with Materials and Atoms*, 24 – 25, Part 1:18 – 25, 1987.

[102] A. Prochazka. *Private Communication*.

[103] H. Geissel. *Private Communication*.

[104] H. Weick. *Private Communication*.

[105] M. Berz, H.C. Hoffmann, and H. Wollnik. COSY 5.0 - the fifth order code for corpuscular optical systems. *Nuclear Instruments and Methods in Physics Research Section A: Accelerators, Spectrometers, Detectors and Associated Equipment*, 258(3):402 – 406, 1987.

[106] http://web-docs.gsi.de/ weick/gicosy/.

[107] M. Stanoiu, K. Sümmerer, I. Mukha, A. Chatillon, E. Cortina Gil, M. Heil, J. Hoffman, O. A. Kiselev, N. Kurz, and W. Ott. A novel si strip array to investigate reaction and decay mechanisms. *Nuclear Instruments and Methods in Physics Research Section B*, 266(19 – 20):4625 – 4627, 2008.

[108] A. A. Lis, C. Mazzocchi, W. Dominik, Z. Janas, M. Pfützner, M. Pomorski, L. Acosta, S. Baraeva, E. Casarejos, J. Duénas-Díaz, V. Dunin, J. M. Espino, A. Estrade, F. Farinon, A. Fomichev, H. Geissel, A. Gorshkov, G. Kamiński, O. Kiselev, R. Knöbel, S. Krupko, M. Kuich, Yu. A. Litvinov, G. Marquinez-Durán, I. Martel, I. Mukha, C. Nociforo, A. K. Ordúz, S. Pietri, A. Prochazka,

A. M. Sánchez-Benítez, H. Simon, B. Sitar, R. Slepnev, M. Stanoiu, P. Strmen, I. Szarka, M. Takechi, Y. Tanaka, H. Weick, and J. S. Winfield. β-delayed three-proton decay of ^{31}Ar. *Physical Review C*, 91:064309, 2015.

[109] O.A. Kiselev, T. Aumann, W. Catford, M. Chartier, P. Egelhof, H. Emling, M. Freer, J.V. Kratz, M. Labiche, R. Lemmon, T. Nilsson, G. Nyman, G. Schrieder, H. Simon, A. Shrivastava, M. Stanoiu, K. Sümmerer, and for the R3B Collaboration. Recoil detector system for the r3b setup. *GSI Report 2006-1, FAIR-NUSTAR-R3B-01*, 2006.

[110] B. Alpat, G. Ambrosi, Ph. Azzarello, R. Battiston, P. Bene, B. Bertucci, S. Bizzaglia, M. Bizzarri, S. Blasko, M. Bourquin, Ph. Bouvier, W.J. Burger, M. Capell, C. Cecchi, Y.H. Chang, E. Cortina, N. Dinu, G. Esposito, E. Fiandrini, D. Haas, H. Hakobyan, M. Ionica, R. Ionica, A. Kounine, V. Koutsenko, A. Lebedev, C. Lechanoine-Leluc, C.H. Lin, F. Masciocchi, M. Menichelli, S. Natale, M. Paniccia, A. Papi, M. Pauluzzi, E. Perrin, M. Pohl, D. Rapin, J.P. Richeux, W. Wallraff, M. Willenbrock, and P. Zuccon. Charge determination of nuclei with the ams-02 silicon tracker. *Nuclear Instruments and Methods in Physics Research Section A*, 540(1):121 – 130, 2005.

[111] B. Alpat, G. Ambrosi, C. Balboni, R. Battiston, A. Biland, M. Bourquin, W.J. Burger, Y.H. Chang, A.E. Chen, N. Dinu, P. Extermann, E. Fiandrini, S.R. Hou, M. Ionica, R. Ionica, W.T. Lin, W. Lustermann, G Maehlum, M. Menichelli, M. Pauluzzi, N. Produit, D. Rapin, D. Ren, M. Ribordy, H. Sann, D. Schardt, K. Sümmerer, G. Viertel, D Vité, W. Wallraff, and S.X Wu. High-precision tracking and charge selection with silicon strip detectors for relativistic ions. *Nuclear Instruments and Methods in Physics Research Section A*, 446(3):522 – 535, 2000.

[112] http://www.ideas.no/.

[113] J. Hoffmann, K. Kurz, and W. Ott. Silicon micro strip detector readout system. *GSI Report 2007-1, INSTRUMENTS-METHODS-21*, 2007.

[114] Multi-Branch System. *http://www-w2k.gsi.de/daq/*.

[115] A. Prochazka. Nuclear structure studies via precise momentum measurements. *PhD thesis, Justus-Liebig Universität Gießen*, 2011.

[116] R. Janik, A. Prochazka, B. Sitar, P. Strmen, I. Szarka, H. Geissel, K.-H. Behr, C. Karagiannis, C. Nociforo, H. Weick, and M. Winkler. Time projection chambers with c-pads for heavy ion tracking. *Nuclear Instruments and Methods in Physics Research Section A: Accelerators, Spectrometers, Detectors and Associated Equipment*, 640(1):54 – 57, 2011.

[117] O.B. Tarasov and D. Bazin. Lise++: Radioactive beam production with in-flight separators. *Nuclear Instruments and Methods in Physics Research Section B: Beam Interactions with Materials and Atoms*, 266(19 – 20):4657 – 4664, 2008. Proceedings of the XVth International Conference on Electromagnetic Isotope Separators and Techniques Related to their Applications.

[118] A. M. Lane and R. G. Thomas. R-matrix theory of nuclear reactions. *Reviews of Modern Physics*, 30:257–353, 1958.

[119] GEANT—detector simulation tool. *CERN software library*.

[120] W. T. Eadie et al. *Statistical Methods in Experimental Physics*. North-Holland, Amsterdam, 1971.

[121] M. Assié, F. de Oliveira Santos, T. Davinson, F. de Grancey, L. Achouri, J. Alcántara-Núñez, T. Al Kalanee, J.-C. Angélique, C. Borcea, R. Borcea, L. Caceres, I. Celikovic, V. Chudoba, D.Y. Pang, C. Ducoin, M. Fallot, O. Kamalou, J. Kiener, Y. Lam, A. Lefebvre-Schuhl, G. Lotay, J. Mrazek, L. Perrot, A.M. Sánchez-Benítez, F. Rotaru, M.-G. Saint-Laurent, Yu. Sobolev, N. Smirnova, M. Stanoiu, I. Stefan, K. Subotic, P. Ujic, R. Wolski, and P.J. Woods. Spectroscopy of ^{18}Na: Bridging the two-proton radioactivity of ^{19}Mg. *Physics Letters B*, 712(3):198 – 202, 2012.

[122] P. Baumann, Ph. Dessagne, A. Huck, G. Klotz, A. Knipper, G. Marguier, C. Miehé, M. Ramdane, C. Richard-Serre, G. Walter, and B. H. Wildenthal. Gamow-teller beta decay of ^{29}Na and comparison with shell-model predictions. *Physical Review C*, 36:765–773, 1987.

[123] M. Shamsuzzoha Basunia. Nuclear data sheets for A = 29. *Nuclear Data Sheets*, 113(4):909 – 972, 2012.

[124] L. V. Grigorenko. Private communication.

[125] I. Angeli and K.P. Marinova. Table of experimental nuclear ground state charge radii: An update. *Atomic Data and Nuclear Data Tables*, 99(1):69 – 95, 2013.

[126] I. Mukha, L. V. Grigorenko, X. Xu, L. Acosta, E. Casarejos, A. A. Ciemny, W. Dominik, J. Duénas-Díaz, V. Dunin, J. M. Espino, A. Estradé, F. Farinon, A. Fomichev, H. Geissel, T. A. Golubkova, A. Gorshkov, Z. Janas, G. Kamiński, O. Kiselev, R. Knöbel, S. Krupko, M. Kuich, Yu. A. Litvinov, G. Marquinez-Durán, I. Martel, C. Mazzocchi, C. Nociforo, A. K. Ordúz, M. Pfützner, S. Pietri, M. Pomorski, A. Prochazka, S. Rymzhanova, A. M. Sánchez-Benítez, C. Scheidenberger, P. Sharov, H. Simon, B. Sitar, R. Slepnev, M. Stanoiu, P. Strmen, I. Szarka, M. Takechi, Y. K. Tanaka, H. Weick, M. Winkler, J. S. Winfield, and

M. V. Zhukov. Observation and spectroscopy of new proton-unbound isotopes ^{30}Ar and ^{29}Cl: An interplay of prompt two-proton and sequential decay. *Physical Review Letters*, 115:202501, 2015.

[127] R. G. Thomas. An analysis of the energy levels of the mirror nuclei, C^{13} and N^{13}. *Phys. Rev.*, 88:1109–1125, 1952.

[128] Joachim B. Ehrman. On the displacement of corresponding energy levels of C^{13} and N^{13}. *Phys. Rev.*, 81:412–416, 1951.

[129] E. Comay, I. Kelson, and A. Zidon. The thomas-ehrman shift across the proton dripline. *Physics Letters B*, 210(1 – 2):31 – 34, 1988.

[130] M. Shamsuzzoha Basunia. Nuclear data sheets for A = 28. *Nuclear Data Sheets*, 114(10):1189 – 1291, 2013.

[131] W.A. Friedman and G.F. Bertsch. Whence the odd-even staggering in nuclear binding? *The European Physical Journal A*, 41(1):109–113, 2009.

[132] T. A. Golubkova, X. Xu, L. V. Grigorenko, I. G. Mukha, C. Scheidenberger, and M. V. Zhukov. Transition from direct to sequential two-proton decay in s-d shell nuclei. *ArXiv*:1605.01013, 2016.

[133] G. Audi, M. Wang, A. H. Wapstra, F. G. Kondev, M. MacCormick, X. Xu, and B. Pfeiffer. The ame2012 atomic mass evaluation. *Chinese Physics C*, 36:1287, 2012.

[134] L.S. Geng, H. Toki, A. Ozawa, and J. Meng. Proton and neutron skins of light nuclei within the relativistic mean field theory. *Nuclear Physics A*, 730(1 - 2):80 – 94, 2004.

[135] G. Audi, M. Wang, A. H. Wapstra, F. G. Kondev, M. MacCormick, X. Xu, and B. Pfeiffer. The nubase2012 evaluation of nuclear properties. *Chinese Physics C*, 36:1157, 2012.

[136] Super-FRS Collaboration. Scientific program of the Super-FRS collaboration: report of the collaboration to the FAIR management. *GSI Report 2014-4*, 2014.

[137] I. Mukha et al. Expert (exotic particle emission and radioactivity by tracking) studies at the Super-FRS spectrometer. *Proceedings of International Syposium on Exotic Nuclei*, 579 - 596, 2014.

Acknowledgements

There are many people provided me help and support during my doctoral thesis work. It is a great pleasure for me to express my gratitude towards them.

First of all I would like to thank Prof. Dr. Christoph Scheidenberger and Prof. Dr. Dr. h.c. Hans Geissel for giving me the opportunity to work on this interesting topic. Prof. Dr. Christoph Scheidenberger is a warmhearted supervisor. I would like to express my deep gratitude to him for his guidance and support whenever it was needed. He proofread the thesis and provided me a lot of invaluable suggestions and comments. I also want to thank Prof. Dr. Dr. h.c. Hans Geissel, who always provided me advice and help. I learned a lot of basics about the FRS spectrometer system from him. His broad knowledge of physics inspired me a lot. Moreover, I would like to express my gratitude to Prof. Dr. Horst Lenske and Prof. Dr. Kai-Thomas Brinkmann for joining the examination committee.

It's a real pleasure to thank Prof. Dr. Jie Meng, who introduced me into the field of nuclear physics. I learned a lot from his wide and deep knowledge of nuclear physics. I sincerely appreciate his support and help throughout my thesis work. I also want to express my deep appreciation to Dr. Baohua Sun, who offered me the opportunity to study at JLU Gießen and GSI. There are so many things I learned from him. He have taught me the basic knowledge on the experimental nuclear physics and have been supporting me since my master work.

I would like to especially thank Dr. Ivan Mukha, my academic mentor, for his daily guidance and help in my practical work on the data analysis. He spent enormous amounts of time for improving my understanding of physics related to the two-proton radioactivity. I'm very grateful for his effort to find time to answer my never-ending questions. Ivan carefully read and corrected the thesis. His supervision, advices, patience, and encouragement in the process of completing this work are highly appreciated.

I want to express my appreciation to all my collaborators, who contributed into our experiment and made it successful. Especially, I'm grateful to Dr. Leonid Grigorenko for his guidance on the theoretical understanding of the two-proton decay. The discussions with him are very illuminating. Special thanks also go to Dr. Oleg Kiselev, for the comprehensive explanations on the silicon strip detectors used in our experiment.

I would like to express my gratitude to Dr. Andrej Prochazka, a long-time office-mate,

who always offered me help. I learned much knowledge about the time-projection chamber and other detectors from him.

Next thanks go to Dr. Helmut Weick, who introduced me the basics of ion optics and provided me a detailed explanation on the ion-optical settings used in our experiment.

I wish to express my appreciation to all colleagues of the FRS group at GSI. They provided me a lot of practical help and advice during the period of my thesis work. Especially, I would like to express my thanks to Ms. Siglind Raiss, Ms. Luise Dörsching-Steitz, and Ms. Daniela Preß for their kindly help and assistance whenever it is needed.

I would like to thank all the members in IONAS-group at II. Physikalisches Institut, JLU Gießen. Their kindly help made the period of my stay in Gießen comfortable and enjoyable. In addition, I'm grateful to Ms. Evelin Prinz for taking care of the university bureaucracy.

Furthermore, I want to thank all my friends. They made the period of my doctoral work nice and enjoyable. It was really a pleasure to have friends like Dr. Fabio Schirru, Dr. Soumya Bagchi, and Dr. Yoshiki Tanaka. We had many interesting discussions and much fun during lunches and coffee breaks. My special thanks go to my good friend Xiaoyu Guo, who offered me a lot of help. I'm very grateful to him for spending some time to check the kinematic equations used in the thesis.

I wish to thank my girlfriend Jie Zhang for her love and support during these years. Last but not the least, I would like to express my deepest gratitude towards my parents, my sister, and other family members for their unwavering support, love, patience, and encouragement.